

Mechanistic Study of Cu-Mediated,
Photoinduced C–S Bond Formation
and Demonstration of Electrochemical
Ammonia Production by a Surface-
Attached Iron Complex

Thesis by
Kareem Imad Hannoun

In Partial Fulfillment of the Requirements for
the degree of
Doctor of Philosophy

Caltech

CALIFORNIA INSTITUTE OF TECHNOLOGY
Pasadena, California

2019
(Defended May 6, 2019)

ACKNOWLEDGEMENTS

My time at Caltech has been both fulfilling and frustrating. I have been privileged to work with an incredible group of scientists, from whom I have learned and grown immensely. As an advisor, Jonas has given me this opportunity and challenged me to grow as a scientist and person. The other members of my committee have also encouraged me to achieve more and provided support and guidance along the way. I especially have to thank the members of the Peters lab I've had the honor of overlapping, who have helped me in more ways than I could possibly list here. I especially have to thank Yichen Tan, Jon Rittle, and John Anderson, who all helped me get on my feet in a new environment. Miles Johnson was a great colleague who really pushed me to do thorough and careful science and had a lasting influence on the way I approach my work self-critically.

I would also like to thank the training and mentorship I received as an undergraduate. Richard Jordan took me in as a clueless undergraduate and showed great patience with me as I acquired the skills and knowledge necessary to succeed. His fastidiousness and kind feedback encouraged me to continue in chemistry and develop a keen eye for data analysis. The camaraderie I experienced in the Jordan group gave me an opportunity to learn from many scientists with disparate backgrounds.

I need to thank all the friends who've helped me through graduate school. Nik Thompson and Blake Daniels were instrumental in my happiness and adjustment to Caltech. Paul Walton, Trevor Del Castillo, Ben Matson, and Mark Nesbit have all provided great experiences, from hiking and camping together to roasting coffee. Nina Gu has supported me over the past couple of years and provided constant friendship and willingness to have

new experiences outside of lab. Michael McGovern has been a consistent source of support and encouragement. Although we don't get to talk or see each other as often as we would like, I know he's always there for me.

Last, but not least, I need to thank my family for their unwavering support and belief. My parents and my sister Deena have always been encouraging during difficult stretches and I'm lucky to have such a loving family who support me unwaveringly.

ABSTRACT

The worldwide reliance on fossil fuels for energy and petrochemicals poses a massive environmental hazard. Furthermore, many chemical processes rely on precious metals that have low abundance on Earth and are threatened. As the world population grows rapidly, these factors pose an increasing threat to our planet and new chemical processes are needed that employ earth-abundant catalysts and alternative chemical currencies such as light and electricity derived from renewable sources.

Chapter 2 discusses an in-depth mechanistic study of the photoinduced, copper-mediated cross-coupling of aryl thiols with aryl halides. This reaction employs light energy and an earth-abundant metal to achieve bond formation through a pathway distinct from that of thermal reactions. In particular, I focus on the stoichiometric photochemistry and subsequent reactivity of a $[\text{Cu}^{\text{I}}(\text{SAr})_2]^-$ complex (Ar = 2,6-dimethylphenyl). A broad array of experimental techniques furnish data consistent with a pathway in which a photoexcited $[\text{Cu}^{\text{I}}(\text{SAr})_2]^{-*}$ complex undergoes SET to generate a Cu^{II} species and an aryl radical, which then couple through an in-cage radical recombination.

Chapter 3 discusses the surface attachment of a $\text{P}_3^{\text{B}}\text{Fe}$ complex to a carbon electrode, and the electrochemical generation of ammonia from N_2 by the surface-appended species ($\text{P}_3^{\text{B}}\text{Fe}$ = tris-phosphinoborane). Ammonia production is achieved industrially by the combination of N_2 and H_2 , the latter of which is derived from methane with concomitant production of CO_2 . Alternative chemical processes, such as the use of energy derived from electricity, are vital for the decreasing the carbon footprint of ammonia production. Synthetic modification of a previously-reported $\text{P}_3^{\text{B}}\text{Fe}$ complex by addition of three pyrene substituents onto the catalyst backbone allows non-covalent attachment onto a graphite surface. The

resulting functionalized electrode shows good stability towards iron desorption under highly reducing conditions, and produces 1.4 equiv NH_3 per iron site. The data presented provide the first demonstration of electrochemical nitrogen fixation by a molecular complex appended to an electrode.

PUBLISHED CONTENT AND CONTRIBUTIONS

- (1) Johnson, M. W.[†]; **Hannoun, K. I.**[†]; Tan, Y.; Fu, G. C.; Peters, J. C. A Mechanistic Investigation of the Photoinduced, Copper-Mediated Cross-Coupling of an Aryl Thiol with an Aryl Halide. *Chem. Sci.* **2016**, *7* (7), 4091–4100. <https://doi.org/10.1039/C5SC04709A>. K.I.H. participated in running experiments, data analysis, DFT calculations, and manuscript preparation.

[†]These authors contributed equally.

TABLE OF CONTENTS

Acknowledgements	iii
Abstract	v
Published Content and Contributions.....	vii
Table of Contents.....	viii
List of Illustrations and/or Tables	x
Nomenclature.....	xiii
Chapter I: Introduction	1
1.1 Motivation	1
1.2 Copper-Mediated Cross Coupling and Photochemistry.....	2
1.3 Mechanism of Copper-mediated Coupling Reactions	3
1.4 Reduction of N ₂ to NH ₃ by Molecular Catalysts.....	6
1.5 Surface Attachment of Molecular Electrocatalysts	10
1.6 Chapter Summaries	12
1.7 References	13
Chapter II: A Mechanistic Investigation of Photoinduced, Copper-Catalyzed Cross-Couplings of Aryl Thiols with Aryl Halides.....	21
2.1 Introduction	21
2.2 Results and Discussion.....	23
2.3 Conclusions	43
2.4 References	45
Chapter III: Electrochemical Ammonia Production by a Surface-Attached Iron Complex	55
3.1 Introduction	55
3.2 Results and Discussion.....	56
3.3 Conclusion	62
3.4 References	62
Appendix A: Supplementary Information for Chapter II.....	66
A.1 General Considerations	66
A.2 Synthesis and Characterization	70
A.3 Molar Conductivity Measurements	76
A.4 Spectroscopic Identification of Copper(II) Species	76
A.5 Identification of 2.1 by ESI-MS.....	77
A.6 Radical Clock Experiments.....	78
A.7 Stoichiometric of [Cu ^I (SAr) ₂]Na with Phenyl Halides	81
A.8 Stern-Volmer Quenching Experiment	81
A.9 Steady-State Fluorimetry Experiment	82
A.10 Reactivity of 1-(but-3-en-1-yloxy)-2-iodobenzene with [Cu ^I (SAr) ₂]Na.....	82
A.11 VT-NMR Study of 2.1	83
A.12 DOSY Experiment	83
A.13 Actinometric Studies	84

A.14 Emission Spectrum of 100-W Hg Lamp	86
A.15 Absorption Spectra of 2.1 in the Presence of 2.2	88
A.16 DFT Calculations	89
A.17 Probe of Direct Coupling between [Cu ^I (SAr) ₂]Na (2.1) and Aryl Radical ...	92
A.18 X-Ray Crystallographic Data.....	96
A.19 ¹ H and ¹³ C NMR Data.....	97
A.20 References.....	110
Appendix B: Supplementary Information for Chapter III.....	113
B.1 General Considerations.....	113
B.2 Synthesis and Characterization	115
B.3 Chemical Ammonia Generation Experiments	119
B.4 Electrochemistry	119
B.5 Electrochemical Ammonia Generation Experiments.	123
B.6 Electrode Desorption Experiment	124
B.7 Supplementary XPS data.....	125
B.8 NMR Spectra	125
B.9 References.....	129

LIST OF ILLUSTRATIONS AND TABLES

Chapter I:	
Scheme 1.1: Copper-mediated Ullmann coupling	2
Scheme 1.2: Copper-catalyzed, ligand-accelerated Ullmann coupling	3
Figure 1.1 Photoexcitation of a Cu ^I -amide to access a highly reducing excited state and photoinduced C–N cross-coupling catalyzed by a Cu ^I -amide	3
Figure 1.2: Possible pathways for ligand-accelerated Ullmann coupling reactions	4
Figure 1.3: Radical clock experiments disfavoring the intermediacy of an aryl radical in the copper-catalyzed C–N and C–S coupling reactions.....	5
Scheme 1.3: Model chemistry demonstrating the viability of a Cu ^I /Cu ^{III} cycle based on oxidative addition and reductive elimination for C–N coupling	5
Figure 1.4: Early mechanistic studies of photoinduced, Cu-catalyzed cross-coupling.....	6
Figure 1.5: First examples of N ₂ activation and catalytic reduction	8
Figure 1.6: Electrochemical reduction of N ₂	9
Figure 1.7: Overview of common strategies for surface attachment of molecular electrocatalysts	11
Chapter II:	
Equation 2.1	21
Equation 2.2	22
Figure 2.1: Outline of a possible catalytic cycle for photoinduced, copper-catalyzed cross-coupling.....	22
Equation 2.3	23
Figure 2.2: An alternative mechanism: coupling of an aryl radical with a copper(I)-thiolate as a key step.....	24
Figure 2.3: An alternative mechanism: S _{RN} 1	25
Figure 2.4: An alternative mechanism: concerted oxidative addition	25
Equation 2.4	26
Equation 2.5	27
Equation 2.6	27
Figure 2.5: X-ray crystal structure of [Cu ^I (SAr) ₂][Na(12-crown-4) ₂] (2.1).....	28
Equation 2.7	29
Figure 2.6: Cyclic voltammograms of [Cu ^I (SAr) ₂ Na (2.1) and of NaSAr.....	30
Figure 2.7: Optical spectrum and time-resolved luminescence of 2.1	32
Figure 2.8: Difference density plot for the lowest energy absorption band of [Cu ^I (SAr) ₂]Na (2.1).....	33
Figure 2.9: Stern–Volmer plot for the luminescence quenching of [Cu ^I (SAr) ₂]Na* in the presence of Ph–I.....	34
Equation 2.8.....	35
Table 2.1: Reactions of a copper–thiolate with an aryldiazonium salt	36

Equation 2.9	36
Table 2.2: Reaction of an aryl radical: Cyclization versus capture by a copper–thiolate	38
Equation 2.10.....	39
Figure 2.10: X-band EPR spectrum (77 K) of a coupling reaction following irradiation for 5 min	40
Figure 2.11: Optical spectrum of a coupling reaction prior to photolysis and after photolysis in propionitrile at $-78\text{ }^{\circ}\text{C}$	41
Equation 2.11.....	41
Equation 2.12.....	42
Figure 2.12: Spin density plots of $[\text{Cu}^{\text{II}}(\text{SAr})_3]^-$ and $\text{Cu}^{\text{II}}(\text{SAr})_2$	43
Chapter III:	
Scheme 3.1.....	57
Scheme 3.2.....	57
Figure 3.1: UV-vis spectra of authentic sample of 3.3 and sample of 3.3 recovered from functionalized electrode	59
Figure 3.2: Cyclic voltammograms of functionalized and unfunctionalized electrodes	60
Table 3.1: Yields of NH_3 from CPE experiments with $\text{P}^{\text{v}}\text{P}_3^{\text{B}}\text{FeMe}$ -functionalized electrodes.....	61
Figure 3.3: XPS spectra.....	62
Appendix A:	
Figure A.1: Representative example of reaction setup using a 100-W Hg lamp ...	69
Table A.1: Molar conductivities of measured compounds	76
Figure A.2: ESI-MS of 2.1	78
Table A.2: Reactivity of 2.1 with 1-(allyloxy)-2-iodobenzene.....	79
Table A.3: Reactivity of 2.1 with 1-(but-3-en-1-yloxy)-2-iodobenzene	80
Table A.4: Reactivity of 2.1 with 2-iodobenzophenone	80
Table A.5: Stability of radical clocks.....	80
Table A.6: Reactivity of 2.1 with iodobenzene and control experiments.....	81
Table A.7: Excited-state lifetime as a function of quencher concentration.....	82
Table A.8: Product distribution in the reaction of 2.1 with 1-(but-3-en-1-yloxy)-2-iodobenzene	82
Figure A.3: Low temperature and ambient temperature ^1H NMR of 2.1	83
Table A.9: Measured hydrodynamic radii	84
Table A.10: DFT-calculated radii	84
Figure A.4: Emission spectrum of 100-W Blak-Ray Long Wave Ultraviolet Lamp (Hg).....	87
Figure A.5: Absorbance spectra of $[\text{Cu}^{\text{I}}(\text{SAr})_2]\text{Na}$ in acetonitrile at various concentrations	87
Figure A.6: Absorbance spectra of sodium 2,6-dimethylthiophenolate in acetonitrile at various concentrations	88
Figure A.7: Optical spectra of 2.1 in the presence of increasing concentrations of sodium 2,6-dimethylthiophenolate	88
Figure A.8: Optical spectra of 2.1 in the presence of	

sodium 2,6-dimethylthiophenolate at variable temperature.....	89
Figure A.9: Calculated free energies of two possible Cu(I) speciations.....	90
Figure A.10: Calculated free energies of three possible Cu(II) speciations	90
Table A.11: Free energies of computed molecules	90
Figure A.11: Spin density plots of Cu(2,6-dimethylthiophenolate) ₂ and [Cu(2,6-dimethylthiophenolate) ₃] ⁻	91
Figure A.12: DFT structures of Cu(2,6-dimethylthiophenolate) ₂ and [Cu(2,6-dimethylthiophenolate) ₃] ⁻ showing the orientation of the g tensor ...	92
Table A.12: Crystal Data and Structure Refinement for 2.1	96
Figure A.13: ¹ H NMR of [Cu ^I (SAr) ₂ Na].....	97
Figure A.14: ¹ H NMR of Sodium 2,6-dimethylthiophenolate.....	98
Figure A.15: ¹ H NMR of 4-Methoxyphenyl 2,6-dimethylphenyl sulfide	99
Figure A.16: ¹³ C NMR of 4-Methoxyphenyl 2,6-dimethylphenyl sulfide	100
Figure A.17: ¹ H NMR of 2-(Allyloxy) 2,6-dimethylphenyl sulfide.....	101
Figure A.18: ¹³ C NMR of 2-(Allyloxy) 2,6-dimethylphenyl sulfide.....	102
Figure A.19: ¹ H NMR of 3-(2,6-dimethylphenylthiomethyl)-2,3-dihydrobenzo-furan.....	103
Figure A.20: ¹³ C NMR of 3-(2,6-dimethylphenylthiomethyl)-2,3-dihydrobenzo-furan.....	104
Figure A.21: ¹ H NMR of 2-(2,6-dimethylphenylthio)-benzophenone	105
Figure A.22: ¹³ C NMR of 2-(2,6-dimethylphenylthio)-benzophenone	106
Figure A.23: ¹ H NMR of 2-(but-3-en-yloxy) 2,6-dimethylphenyl sulfide	107
Figure A.24: ¹³ C NMR of 2-(but-3-en-yloxy) 2,6-dimethylphenyl sulfide.....	108
Figure A.25: ¹ H NMR of 4-(methylchromane) 2,6-dimethylphenyl sulfide.....	109
Figure A.26: ¹³ C NMR of 4-(methylchromane) 2,6-dimethylphenyl sulfide.....	110
Appendix B:	
Figure B.1: Cyclic voltammogram of ^{py} P ₃ ^B (3.1).....	121
Figure B.2: Cyclic voltammogram of ^{py} P ₃ ^B FeMe (3.3)	121
Figure B.3: Cyclic voltammogram of [^{py} P ₃ ^B FeN ₂][Na(THF) _n] (3.4)	122
Figure B.4: Cyclic voltammograms of surface-attached ^{py} P ₃ ^B (3.1).....	123
Figure B.5: Overview XPS spectra.....	125
Figure B.6: ¹ H NMR of 3-Iodo-4-Bromo- <i>O</i> -(1-pyrenyl-butyl)phenol	125
Figure B.7: ¹³ C{ ¹ H} NMR of 3-Iodo-4-Bromo- <i>O</i> -(1-pyrenyl-butyl)phenol	126
Figure B.8: ¹ H NMR of 3-diisopropylphosphino-4-Bromo- <i>O</i> -(1-pyrenyl-butyl)phenol	126
Figure B.9: ³¹ P{ ¹ H} NMR of 3-diisopropylphosphino-4-Bromo- <i>O</i> -(1-pyrenyl-butyl)phenol	126
Figure B.10: ¹ H NMR of ^{py} P ₃ ^B (3.1).....	127
Figure B.11: ³¹ P{ ¹ H} NMR of ^{py} P ₃ ^B (3.1)	127
Figure B.12: ¹ H NMR of ^{py} P ₃ ^B FeBr (3.2).....	127
Figure B.13: ¹ H NMR of ^{py} P ₃ ^B FeMe (3.3)	128
Figure B.14: ¹ H NMR of [^{py} P ₃ ^B FeN ₂][Na(THF) _n] (3.4).....	128

NOMENCLATURE

- A.** Absorbance.
Å. Angstrom.
Ar. Aryl group.
ATR. Attenuated Total Reflectance.
A(X). Hyperfine coupling constant due to nucleus X
BAr^F₄. [B(3,5-C₆H₃(CF₃)₂)₄]⁻
Carb. Carbazolide.
Cat. Catalyst.
CO₂RR. CO₂ Reduction Reaction.
CPE. Controlled Potential Electrolysis.
CV. Cyclic Voltammetry or Cyclic Voltammogram.
D. Doublet or deuterium.
DCM. Dichloromethane
DFT. Density Functional Theory.
DMF. Dimethylformamide.
DMPHEN. 2,8-dimethyl-1,10-phenanthroline.
DOSY. Diffusion Ordered Spectroscopy
D_x. Compound with x deuterium atoms.
E. Electron.
E°. Thermodynamic reduction or oxidation potential.
E_p. Peak reduction or oxidation potential.
EPR. Electron Paramagnetic Resonance.
EPR. Electron Paramagnetic Resonance.
Eqn. Equation.
Equiv. Equivalent(s).
ESI-MS. Electrospray Ionization-Mass Spectrometry.
FT. Fourier Transform.
g. Electron g-factor.
GC. Gas Chromatography.
HER. Hydrogen Evolution Reaction.
HOPG. Highly Ordered Pyrolytic Graphite.
HPLC. High-Performance Liquid Chromatography.
I. Nuclear spin quantum number.
ⁱPr. Isopropyl.
IR. Infrared.
J. NMR coupling constant.
L. Generic ligand or liter.
LTQ. Linear Trap Quadrupole.
Lut. 2,6-lutidine.
M. Multiplet or metal.

NMR. Nuclear Magnetic Resonance.
Nuc. Nucleophile.
OTf. Trifluoromethanesulfonate anion.
P₃^B. Tris(*o*-diisopropylphosphinophenyl)borane.
Phen. 1,10-phenanthroline.
^{py}P₃^B. (*o*-^{*i*}Pr₂P-*p*-O(CH₂)₄pyrene-(C₆H₄))₃B.
Pyrr. Pyrrolidinone.
Q. Stern-Volmer quenching fraction, quality factor, or quartet.
R. Alkyl or aryl group.
S. Siemen (Ω⁻¹).
S. Spin quantum number.
SCE. Saturated Calomel Electrode.
SET. Single Electron Transfer.
S_N2. Bimolecular nucleophilic substitution.
S_NAr. Nucleophilic aromatic substitution.
S_{RN}1. Unimolecular radical nucleophilic substitution.
T. Triplet.
t-Bu. Tertiary-butyl.
TD-DFT. Time-Dependent Density Functional Theory.
TEMPO. 1-hydroxyl-2,2,6,6-tetramethylpiperidine anion.
TEMPOH. 1-hydroxyl-2,2,6,6-tetramethylpiperidine.
TMS. Tetramethylsilane.
UV-vis. Ultraviolet-visible.
X-band. Radio frequency range from 8.0 to 12.0 GHz (typically ~9.5 GHz for EPR).
XPS. X-ray Photoelectron Spectroscopy.
δ. NMR chemical shift.
ε. Extinction coefficient.
Λ_m. Molar conductivity.
μ_B. Bohr Magneton.
μ_{eff}. Effective magnetic moment.
Φ. Quantum Yield.

INTRODUCTION

1.1 Motivation

Over the current century, rapidly growing world population and increased energy usage in the developing world is projected to lead to at least a three-fold increase of worldwide energy usage.¹ The majority of energy currently comes from non-renewable sources that produce CO₂ emissions, contributing to climate change.² While renewable energy alternatives exist for providing electricity with a low carbon footprint, many chemical processes are reliant on fossil-fuel feedstocks such as natural gas.³

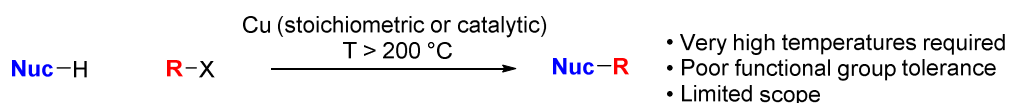
Furthermore, many important chemical processes rely on precious metals such as Pd, Rh, and Ir.^{4,5} These metals have low abundance on earth and their continued usage is not sustainable based on projected worldwide growth. Due to the use of precious metals and fossil-fuel based chemical feedstocks in many vital chemical processes, there is an urgent need to develop new chemical methods that use earth-abundant metals and incorporate alternative sources of energy such as sunlight and electricity.⁶

The use of alternative chemical processes opens up new methods for bond formation based on divergent reactivity.⁷ The development on new strategies for difficult bond formation reactions also opens up the possibility of discovering new transformations unachievable with previous methods. To better apply these new chemical methods to broader classes of reactions, we seek to understand the mechanism of these transformations and identify key reaction steps that we can alter through reaction design. The design and study

of photochemical and electrochemical reactions mediated by earth-abundant metals will lead to a greater understanding of reaction pathways operative in these classes of reactions.

However, many barriers exist to elucidating pathways of photochemical and electrochemical reactions. Photochemical reactions are often complex, and common spectroscopic methods that are suitable for thermally-driven reactions are not always applicable to their study. Electrochemical transformations can be difficult to control due to the interfacial and heterogeneous nature of electron transfer. Multi-electron, multi-proton redox processes are also complex due to the vast number of possible reaction pathways that can be spanned. Despite these difficulties, improvement and study of electrochemical and photochemical reactions is necessary to better employ renewable energy sources for chemical reactions. This thesis will discuss the study of photochemical bond formation reactions and development of an electrochemical N₂ reduction system.

1.2 Copper-Mediated Cross Coupling and Photochemistry



Scheme 1.1: Copper-mediated Ullmann coupling.

The coupling of nucleophiles and electrophiles catalyzed by copper dates back to the early 20th century, making it the first example of metal-catalyzed cross-coupling (Scheme 1.1).^{8,9} These early coupling reactions required harsh reaction conditions and showed limited functional group tolerance, leading to these methods being superseded by catalytic reactions based on precious metals such as palladium.¹⁰ In the early 21st century, it was discovered that the addition of chelating ligands, typically bidentate nitrogen donors, led to enhanced reactivity at lower temperatures with broader functional group tolerance relative to ligand-

free conditions (Scheme 1.2).¹¹ Over the last 15 years, there has been a significant growth in the use and number of reports of copper-catalyzed reactions.¹²



Scheme 1.2: Copper-catalyzed, ligand-accelerated Ullmann coupling.

Copper complexes have also been noted for their desirable photophysical properties, such as long excited-state lifetimes and highly reducing excited states.¹³ Our group has studied a number of P- and N-coordinated Cu^I complexes that access highly-reducing excited states, and we sought to employ these complexes to achieve copper-mediated bond formation reactions through single-electron redox processes.^{14–17} In 2012, we reported the copper-catalyzed coupling of carbazole with aryl halides through a radical pathway (Figure 1.1).¹⁸ This approach has been successfully expanded to a number of nucleophiles and electrophiles, yet many mechanistic questions remained (and still remain) unanswered.

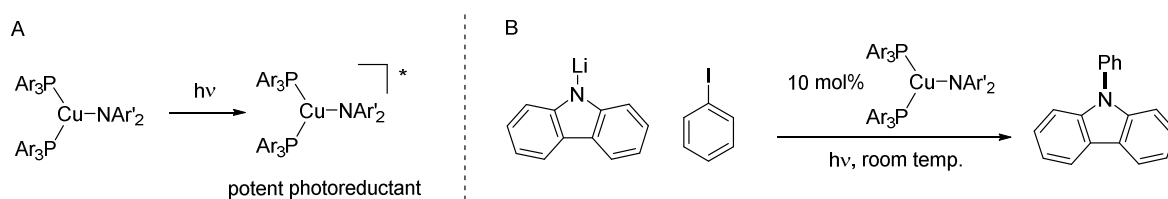


Figure 1.1: (A) Photoexcitation of a Cu^I-amide to access a highly reducing excited state. (B) Photoinduced C–N cross-coupling catalyzed by a Cu^I-amide.

1.3 Mechanism of Copper-mediated Coupling Reactions

Despite the long history of copper-catalyzed coupling reactions, very little was understood about the pathways operative in these reactions until recently. This lack of

understanding provided an obstacle to reaction discovery and optimization, as chemists were not able to make rational choices in testing substrates and ligands.

Early mechanistic work on thermal copper-catalyzed coupling reactions demonstrated that Cu^{I} -nucleophile complexes are key reaction intermediates, and that these intermediates can react with electrophiles.¹⁹ Several mechanisms have been proposed for this step, including (i) oxidative addition to generate a Cu^{III} intermediate, (ii) halogen atom transfer to generate a Cu^{II} -halide and electrophile radical, (iii) single-electron transfer (SET) to generate a Cu^{II} complex and electrophile radical, and (iv) σ -bond metathesis through a 4-centered transition state (Figure 1.2).

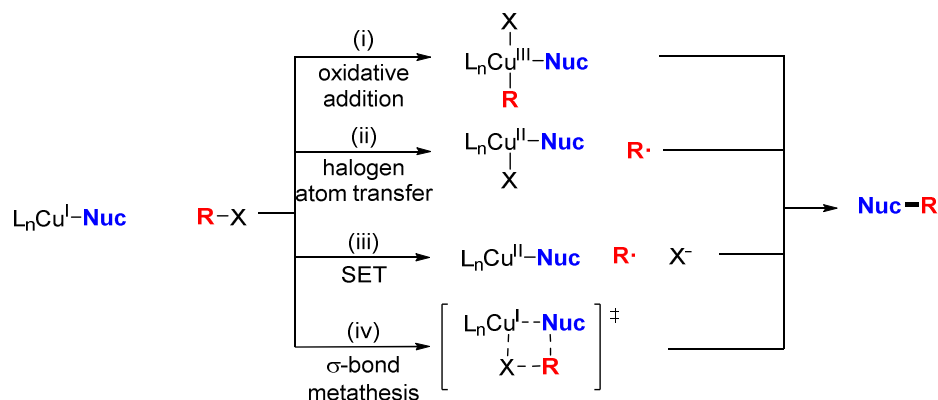


Figure 1.2: Possible pathways for ligand-accelerated Ullmann coupling reactions.

A number of radical clock and radical trapping experiments have disfavored mechanisms involving the formation of a free electrophile radical (Figure 1.3).^{19,20} However, these studies do not exclude the possibility of short-lived radical intermediates that undergo rapid recombination. Mechanistic studies on the reaction of iodobenzene and both methanol and methylamine concluded that both iodine atom transfer and single electron transfer mechanisms were accessible, with the preferred pathway depending on the nature of the nucleophile and ancillary ligand.²¹ While evidence exists for all pathways mentioned, most

proposals favor oxidative addition to generate a Cu^{III} species.²² The Ribas and Stahl groups demonstrated the viability of this oxidative addition mechanism by stoichiometrically demonstrating the synthesis of a macrocyclic Cu^{III} complex that undergoes reductive elimination to form a C–N bond (Scheme 1.3).²³ It is likely that different mechanisms may be operative in thermal Ullmann coupling reactions depending on the reaction conditions, or that multiple pathways may be accessible even in a single reaction.

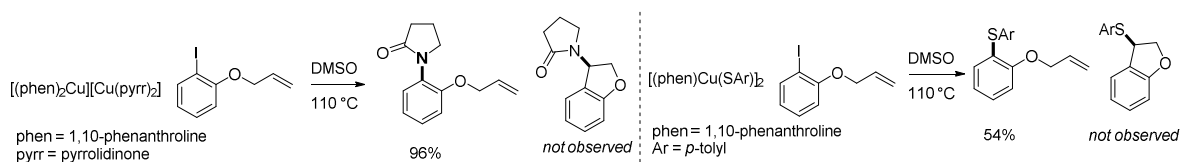
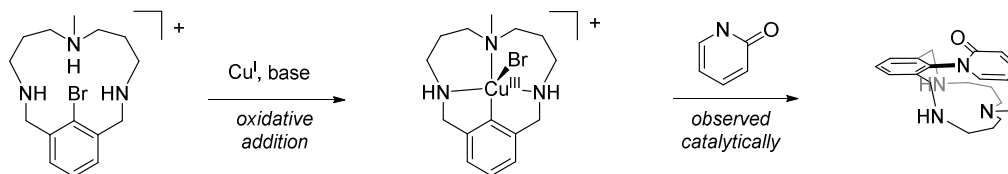


Figure 1.3: Radical clock experiments disfavoring the intermediacy of an aryl radical in the copper-catalyzed C–N (left) and C–S (right) coupling reactions.



Scheme 1.3: Model chemistry demonstrating the viability of a $\text{Cu}^{\text{I}}/\text{Cu}^{\text{III}}$ cycle based on oxidative addition and reductive elimination for C–N coupling.

In the photoinduced arylation of carbazole by a copper phosphine complex, early evidence supports a mechanism involving photoexcitation of a bis-phosphine copper carbazolid species as the first step.¹⁸ Complexes of this type can be quenched by iodobenzene, and EPR data of a frozen reaction mixture revealed the presence of a Cu^{II} species, consistent with photoinduced single-electron transfer (SET) from Cu^{I} to iodobenzene to form a Cu^{II} species and an aryl radical (Figure 1.4). Radical cyclization

experiments supported the intermediacy of an aryl radical, but the mechanism of the bond formation step was not determined.

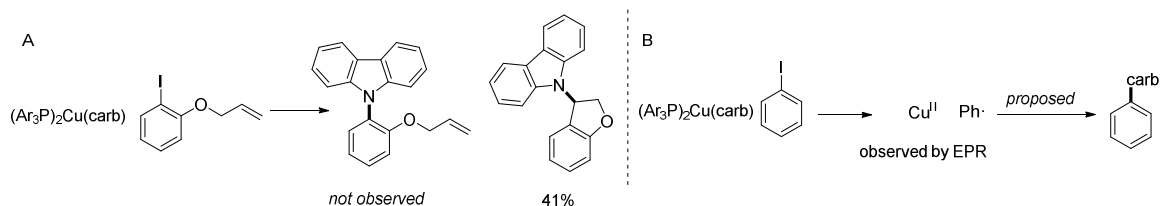


Figure 1.4: Early mechanistic studies of photoinduced, Cu-catalyzed cross-coupling. (A) Radical clock experiments demonstrating the intermediacy of an aryl radical. (B) Observation of a Cu^{II} species under catalytic conditions, which is proposed to be involved in C–N bond formation.

Following this report, a number of photoinduced copper-catalyzed cross coupling reactions were reported by our group, including N-alkylation,^{24, 25} S-arylation,²⁶ O-arylation,²⁷ and C-alkylation reactions.²⁸ These reactions did not require traditional ligands such as phosphines, and proceeded under varying conditions. We then sought to investigate the mechanism of these reactions to determine the factors affecting these ligand-free reactions and to characterize the mechanistic diversity of these reactions. In particular, we sought to determine the active species in these reactions, understand their photochemical properties, and better understand the nature of the coupling step.

1.4 Reduction of N_2 to NH_3 by Molecular Catalysts

The splitting of dinitrogen into ammonia is an essential process for worldwide agriculture, and is performed on a scale of 413 Tg N annually.²⁹ Nitrogen is fixed naturally primarily by nitrogenase enzymes that reside in root nodules of plants such as soybeans and

other legumes.³⁰ However, the amount of nitrogen fixed enzymatically falls significantly short of current worldwide demand.^{29,31}

As a supplement to natural sources of fixed nitrogen, industrial ammonia production represents a significant cost for the efficient growth of various crops. Industrially, N_2 is fixed by the Haber-Bosch process on a scale of 120 Tg N annually.³¹ The Haber-Bosch process employs an iron-based catalyst to convert H_2 and N_2 to ammonia at high temperature and pressure. While efficient, the Haber-Bosch process uses 2% of the global energy output and requires significant infrastructure. The majority of this energy input is employed for H_2 production through steam reforming and the water-gas shift reaction, which leads to CO_2 formation.^{29,32} The low volumetric energy density of H_2 also requires its on-site production and limits Haber-Bosch plants to areas that have large amounts of hydrocarbon fuels.³³ Development of scalable alternatives to the Haber-Bosch process that can be coupled to solar light or energy is important to the decentralized production of ammonia in the developing world, as well as to meeting the growing demand for ammonia-based fertilizer throughout the developed world.

As an alternative to the Haber-Bosch process, the fixation of N_2 with protons and electrons has been proposed as a scalable and energy-efficient method.³³ In particular, the reduction of dinitrogen with electricity derived from renewable sources is of particular interest. Significant progress has been made in the reduction of dinitrogen by transition metal

complexes over the past 50 years, although efficient catalytic reduction of N_2 remains difficult.

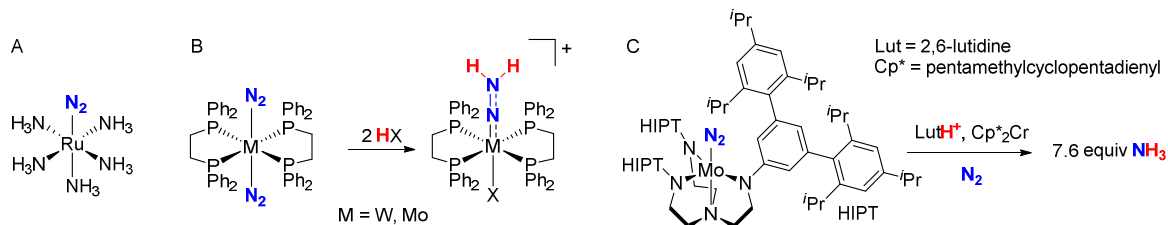


Figure 1.5: (A) The first example of N_2 binding to a transition metal. (B) Protonation of a metal-bound N_2 fragment to give N–H bond formation. (C) Catalytic reduction of N_2 to ammonia by a molybdenum complex.

The binding of N_2 to a transition metal center was first observed by Allen and Senoff at a Ru^{II} center in 1965.³⁴ In 1972, protonation of a metal-bound N_2 fragment was first reported by Chatt,³⁵ to give a $M=NNH_2$ species (Figures 1.5A, 1.5B). Catalytic reduction of N_2 to ammonia was then first reported by Schrock in 2003 at a Mo center (Figure 1.5C).³⁶ This report was followed by a number of other reports of catalytic N_2 reduction, including the reduction of N_2 to NH_3 by P_3^BFe by our group.^{37, 38} Despite the rapidly growing number

of reports of N₂ reduction by molecular complexes, chemical reductants and large driving forces are required in nearly every case.

1.4.1 Viability of Electrochemical Reduction

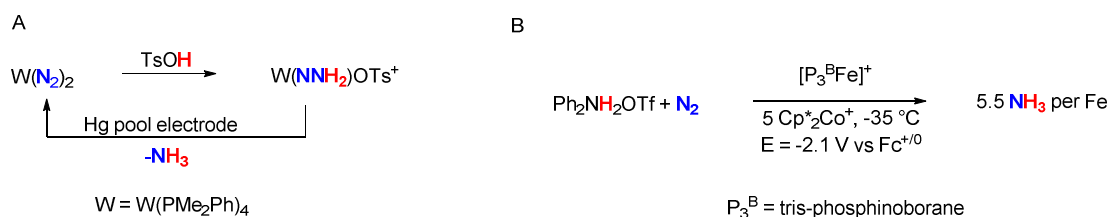


Figure 1.6: (A) Stoichiometric reduction of N₂ to ammonia by a tungsten complex at a Hg pool electrode by Pickett. (B) Electrocatalytic reduction of N₂ to ammonia by a molecular iron complex and a cocatalytic redox mediator by our group.

While most examples of molecular N₂ fixation have utilized relatively strong chemical reductants as the electron source, there has been long-standing interest in using alternative electron sources in N₂ fixation. Reduction of dinitrogen to ammonia without stoichiometric chemical reductants is necessary for coupling ammonia production to sunlight or electricity. In 1985, Pickett and coworkers demonstrated the stoichiometric reduction of N₂ to NH₃ at an electrode mediated by a tungsten phosphine complex (Figure 1.6A).^{39–41} Recently, our group has demonstrated the electrocatalytic reduction of N₂ at low temperature by a tris-phosphinoborane iron catalyst (P₃^BFe, Figure 1.6B).^{42, 43} This was followed by the Berben group's report of stoichiometric N₂ electroreduction by an aluminum complex at

lower overpotential.⁴⁴ These electroreductions demonstrate the viability of a molecular electrochemical strategy to reduce N_2 to ammonia.

1.5 Surface Attachment of Molecular Electrocatalysts

Electrocatalysis is fundamentally important for securing our energy future and producing chemical fuels from renewable energy.⁴⁵ Catalysis by synthetic transition metal complexes offer significant advantages over heterogeneous materials, including the ability to control interactions in their coordination sphere and the multitude of spectroscopic techniques available to study mechanism. These mechanistic understandings can allow rational alteration of catalysts to increase activity and stability.

A number of difficulties arise when soluble molecular complexes are employed as electrocatalysts in solution.⁴⁶ Only a small portion of the added catalyst is electrochemically active at a given time, deleterious bimolecular pathways can occur, catalyst can diffuse into both chambers of the electrochemical cell, and mechanistic study of molecular electrocatalysts presents numerous challenges. To avoid these difficulties, molecular catalysts can be immobilized on an electrode surface. While appealing, catalyst immobilization presents its own challenges. Most immobilization techniques require significant modification to the original catalyst synthesis, and may not be broadly applicable.

It is then difficult to determine the nature of the metal sites on the electrode, and the resulting catalyst activity may differ from that of the freely diffusing catalyst.

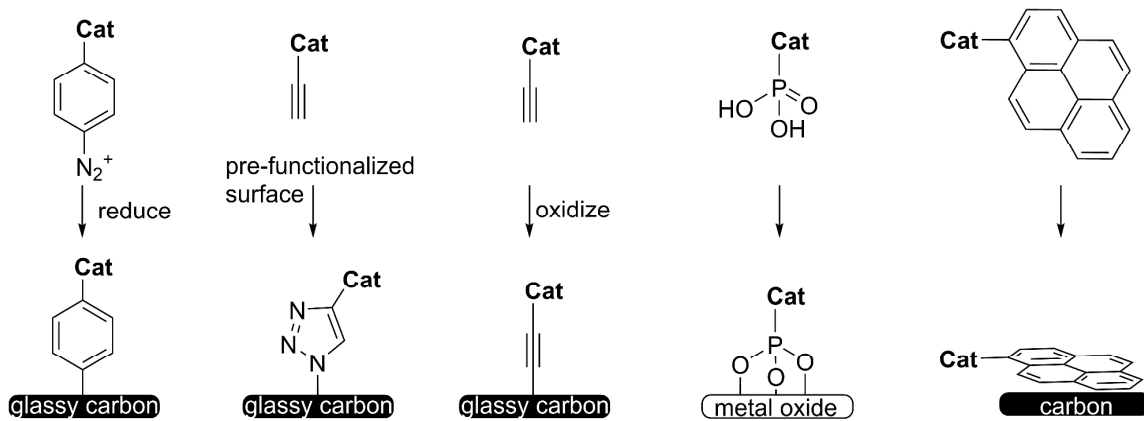


Figure 1.7: Overview of common strategies for surface attachment of molecular electrocatalysts.

Surface immobilization can be achieved by a number of approaches by using various types of catalyst-surface interactions, including both covalent and non-covalent attachment (Figure 1.7). Common covalent strategies include reduction of an aryl diazonium, Cu-catalyzed alkyne-azide click reaction, and alkyne oxidation. Common non-covalent strategies include adsorption of phosphonates on metal oxide layers and adsorption of pyrene moieties onto graphitic carbon surfaces. Covalent attachment methods generally require the incorporation of reactive functional groups and harsh redox processes that may interfere with catalyst synthesis, while adsorption on metal oxide layers allow limited electrode materials to be used.

A number of electrocatalytic reactions relevant to the generation of chemical fuels from electricity have been demonstrated by surface-attached molecular catalysts. The hydrogen evolution reaction (HER) has been heavily studied, as it is the simplest fuel-

forming reaction. A broad number of attachment strategies have been demonstrated for HER by an immobilized catalyst.⁴⁶ The CO₂ reduction reaction (CO₂RR) has also been explored; the harsher and more reducing conditions required for CO₂RR have however limited the applicability of many strategies. Adsorption of pyrene-containing catalysts has been most broadly successful,⁴⁷⁻⁵⁰ although other strategies have been successfully demonstrated.⁵¹⁻⁵⁷

1.6 Chapter Summaries

Chapter 2 discusses an in-depth mechanistic study of the photoinduced, copper-mediated cross-coupling of aryl thiols with aryl halides. In particular, I focus on the stoichiometric photochemistry and subsequent reactivity of a [Cu^I(SAr)₂]⁻ complex (Ar = 2,6-dimethylphenyl). A broad array of experimental techniques furnish data consistent with a pathway in which a photoexcited [Cu^I(SAr)₂]^{-*} complex undergoes SET to generate a Cu^{II} species and an aryl radical, which then couple through an in-cage radical recombination.

Chapter 3 discusses the surface attachment of a P₃^BFe complex to a carbon electrode, and the electrochemical generation of ammonia from N₂ by the surface-appended species. Synthetic modification of a previously-reported P₃^BFe complex by addition of three pyrene substituents onto the catalyst backbone allows non-covalent attachment onto a graphite surface. The resulting functionalized electrode shows good stability towards desorption under highly reducing conditions, and produces 1.4 equiv NH₃ per iron site. The data

presented provide the first demonstration of electrochemical nitrogen fixation by a molecular complex appended to an electrode.

1.7 References

- (1) Lewis, N. S.; Nocera, D. G. Powering the Planet: Chemical Challenges in Solar Energy Utilization. *Proc. Natl. Acad. Sci.* **2006**, *103* (43), 15729–15735.
- (2) Balzani, V.; Credi, A.; Venturi, M. Photochemical Conversion of Solar Energy. *ChemSusChem* **2008**, *1* (1–2), 26–58.
- (3) Olah, G. A. Beyond Oil and Gas: The Methanol Economy. *Angew. Chem. Int. Ed.* **2005**, *44* (18), 2636–2639.
- (4) J. Dunn, P. The Importance of Green Chemistry in Process Research and Development. *Chem. Soc. Rev.* **2012**, *41* (4), 1452–1461.
- (5) Torborg, C.; Beller, M. Recent Applications of Palladium-Catalyzed Coupling Reactions in the Pharmaceutical, Agrochemical, and Fine Chemical Industries. *Adv. Synth. Catal.* **2009**, *351* (18), 3027–3043.
- (6) Chirik, P.; Morris, R. Getting Down to Earth: The Renaissance of Catalysis with Abundant Metals. *Acc. Chem. Res.* **2015**, *48* (9), 2495–2495.
- (7) Holland, P. L. Distinctive Reaction Pathways at Base Metals in High-Spin Organometallic Catalysts. *Acc. Chem. Res.* **2015**, *48* (6), 1696–1702.
- (8) Ullmann, F.; Bielecki, J. Ueber Synthesen in Der Biphenylreihe. *Berichte Dtsch. Chem. Ges.* **1901**, *34* (2), 2174–2185.

- (9) Hassan, J.; Sévignon, M.; Gozzi, C.; Schulz, E.; Lemaire, M. Aryl–Aryl Bond Formation One Century after the Discovery of the Ullmann Reaction. *Chem. Rev.* **2002**, *102* (5), 1359–1470.
- (10) Johansson Seechurn, C. C. C.; Kitching, M. O.; Colacot, T. J.; Snieckus, V. Palladium-Catalyzed Cross-Coupling: A Historical Contextual Perspective to the 2010 Nobel Prize. *Angew. Chem. Int. Ed.* **2012**, *51* (21), 5062–5085.
- (11) Beletskaya, I. P.; Cheprakov, A. V. The Complementary Competitors: Palladium and Copper in C–N Cross-Coupling Reactions. *Organometallics* **2012**, *31* (22), 7753–7808.
- (12) Thapa, S.; Shrestha, B.; K. Gurung, S.; Giri, R. Copper-Catalysed Cross-Coupling: An Untapped Potential. *Org. Biomol. Chem.* **2015**, *13* (17), 4816–4827.
- (13) Horváth, O. Photochemistry of Copper(I) Complexes. *Coord. Chem. Rev.* **1994**, *135–136*, 303–324.
- (14) Harkins, S. B.; Peters, J. C. A Highly Emissive Cu₂N₂ Diamond Core Complex Supported by a [PNP][−] Ligand. *J. Am. Chem. Soc.* **2005**, *127* (7), 2030–2031.
- (15) Miller, A. J. M.; Dempsey, J. L.; Peters, J. C. Long-Lived and Efficient Emission from Mononuclear Amidophosphine Complexes of Copper. *Inorg. Chem.* **2007**, *46* (18), 7244–7246.
- (16) Lotito, K. J.; Peters, J. C. Efficient Luminescence from Easily Prepared Three-Coordinate Copper(I) Arylamidophosphines. *Chem. Commun.* **2010**, *46* (21), 3690–3692.

- (17) Deaton, J. C.; Switalski, S. C.; Kondakov, D. Y.; Young, R. H.; Pawlik, T. D.; Giesen, D. J.; Harkins, S. B.; Miller, A. J. M.; Mickenberg, S. F.; Peters, J. C. E-Type Delayed Fluorescence of a Phosphine-Supported $\text{Cu}_2(\mu\text{-NAr}_2)_2$ Diamond Core: Harvesting Singlet and Triplet Excitons in OLEDs. *J. Am. Chem. Soc.* **2010**, *132* (27), 9499–9508.
- (18) Creutz, S. E.; Lotito, K. J.; Fu, G. C.; Peters, J. C. Photoinduced Ullmann C–N Coupling: Demonstrating the Viability of a Radical Pathway. *Science* **2012**, *338* (6107), 647–651.
- (19) Tye, J. W.; Weng, Z.; Johns, A. M.; Incarvito, C. D.; Hartwig, J. F. Copper Complexes of Anionic Nitrogen Ligands in the Amidation and Imidation of Aryl Halides. *J. Am. Chem. Soc.* **2008**, *130* (30), 9971–9983.
- (20) Chen, C.; Weng, Z.; Hartwig, J. F. Synthesis of Copper(I) Thiolate Complexes in the Thioetherification of Aryl Halides. *Organometallics* **2012**, *31* (22), 8031–8037.
- (21) Jones, G. O.; Liu, P.; Houk, K. N.; Buchwald, S. L. Computational Explorations of Mechanisms and Ligand-Directed Selectivities of Copper-Catalyzed Ullmann-Type Reactions. *J. Am. Chem. Soc.* **2010**, *132* (17), 6205–6213.
- (22) Monnier, F.; Taillefer, M. Catalytic C–C, C–N, and C–O Ullmann-Type Coupling Reactions. *Angew. Chem. Int. Ed.* **2009**, *48* (38), 6954–6971.
- (23) Casitas, A.; King, A. E.; Parella, T.; Costas, M.; Stahl, S. S.; Ribas, X. Direct Observation of $\text{Cu}^{\text{I}}/\text{Cu}^{\text{III}}$ Redox Steps Relevant to Ullmann-Type Coupling Reactions. *Chem. Sci.* **2010**, *1* (3), 326–330.

- (24) Bissember, A. C.; Lundgren, R. J.; Creutz, S. E.; Peters, J. C.; Fu, G. C. Transition-Metal-Catalyzed Alkylations of Amines with Alkyl Halides: Photoinduced, Copper-Catalyzed Couplings of Carbazoles. *Angew. Chem. Int. Ed.* **2013**, *52* (19), 5129–5133.
- (25) Ziegler, D. T.; Choi, J.; Muñoz-Molina, J. M.; Bissember, A. C.; Peters, J. C.; Fu, G. C. A Versatile Approach to Ullmann C–N Couplings at Room Temperature: New Families of Nucleophiles and Electrophiles for Photoinduced, Copper-Catalyzed Processes. *J. Am. Chem. Soc.* **2013**, *135* (35), 13107–13112.
- (26) Uyeda, C.; Tan, Y.; Fu, G. C.; Peters, J. C. A New Family of Nucleophiles for Photoinduced, Copper-Catalyzed Cross-Couplings via Single-Electron Transfer: Reactions of Thiols with Aryl Halides Under Mild Conditions (0 °C). *J. Am. Chem. Soc.* **2013**, *135* (25), 9548–9552.
- (27) Tan, Y.; Muñoz-Molina, J. M.; Fu, G. C.; Peters, J. C. Oxygen Nucleophiles as Reaction Partners in Photoinduced, Copper-Catalyzed Cross-Couplings: O-Arylations of Phenols at Room Temperature. *Chem. Sci.* **2014**, *5* (7), 2831–2835.
- (28) Ratani, T. S.; Bachman, S.; Fu, G. C.; Peters, J. C. Photoinduced, Copper-Catalyzed Carbon–Carbon Bond Formation with Alkyl Electrophiles: Cyanation of Unactivated Secondary Alkyl Chlorides at Room Temperature. *J. Am. Chem. Soc.* **2015**, *137* (43), 13902–13907.
- (29) Fowler, David; Coyle, Mhairi; Skiba, Ute; Sutton, Mark A.; Cape, J. Neil; Reis, Stefan; Sheppard, Lucy J.; Jenkins, Alan; Grizzetti, Bruna; Galloway, James N.; et al. The Global Nitrogen Cycle in the Twenty-First Century. *Philos. Trans. R. Soc. B Biol. Sci.* **2013**, *368* (1621), 20130164.

- (30) Mus, F.; Crook, M. B.; Garcia, K.; Costas, A. G.; Geddes, B. A.; Kouri, E. D.; Paramasivan, P.; Ryu, M.-H.; Oldroyd, G. E. D.; Poole, P. S.; et al. Symbiotic Nitrogen Fixation and the Challenges to Its Extension to Nonlegumes. *Appl Env. Microbiol* **2016**, 82 (13), 3698–3710.
- (31) Erisman, J. W.; Sutton, M. A.; Galloway, J.; Klimont, Z.; Winiwarter, W. How a Century of Ammonia Synthesis Changed the World. *Nat. Geosci.* **2008**, 1, 636–639.
- (32) Recently, the possibility of producing ammonia from dihydrogen derived from water electrolysis has also been explored as a low-carbon alternative to steam reforming. However, this process is extremely energy intensive and relies on a non-abundant platinum catalyst.
- (33) Singh, V.; Dincer, I.; Rosen, M. A. Chapter 4.2 - Life Cycle Assessment of Ammonia Production Methods. In *Exergetic, Energetic and Environmental Dimensions*; Dincer, I., Colpan, C. O., Kizilkan, O., Eds.; Academic Press, 2018; pp 935–959.
- (34) Allen, A. D.; Senoff, C. V. Nitrogenopentammineruthenium(II) Complexes. *Chem. Commun. Lond.* **1965**, 0 (24), 621–622.
- (35) Chatt, J.; Heath, G. A.; Richards, R. L. The Reduction of Ligating Dinitrogen to Yield a Ligating N₂H₂ Moiety. *J. Chem. Soc. Chem. Commun.* **1972**, 0 (18), 1010–1011.
- (36) Yandulov, D. V.; Schrock, R. R. Catalytic Reduction of Dinitrogen to Ammonia at a Single Molybdenum Center. *Science* **2003**, 301 (5629), 76–78.
- (37) Anderson, J. S.; Rittle, J.; Peters, J. C. Catalytic Conversion of Nitrogen to Ammonia by an Iron Model Complex. *Nature* **2013**, 501 (7465), 84–87.
- (38) Roux, Y.; Duboc, C.; Gennari, M. Molecular Catalysts for N₂ Reduction: State of the Art, Mechanism, and Challenges. *ChemPhysChem* **2017**, 18 (19), 2606–2617.

- (39) Pickett, C. J.; Talarmin, J. Electrosynthesis of Ammonia. *Nature* **1985**, *317* (6038), 652.
- (40) Al-Salih, T. I.; Pickett, C. J. Electron-Transfer Reactions in Nitrogen Fixation. Part 1. The Electrosynthesis of Dinitrogen, Hydride, Isocyanide, and Carbonyl Complexes of Molybdenum: Intermediates, Mechanisms, and Energetics. *J. Chem. Soc. Dalton Trans.* **1985**, *6*, 1255–1264.
- (41) Pickett, C. J.; Ryder, K. S.; Talarmin, J. Electron-Transfer Reactions in Nitrogen Fixation. Part 2. The Electrosynthesis of Ammonia: Identification and Estimation of Products. *J. Chem. Soc. Dalton Trans.* **1986**, *7*, 1453–1457.
- (42) Chalkley, M. J.; Del Castillo, T. J.; Matson, B. D.; Roddy, J. P.; Peters, J. C. Catalytic N₂-to-NH₃ Conversion by Fe at Lower Driving Force: A Proposed Role for Metallocene-Mediated PCET. *ACS Cent. Sci.* **2017**, *3* (3), 217–223.
- (43) Chalkley, M. J.; Del Castillo, T. J.; Matson, B. D.; Peters, J. C. Fe-Mediated Nitrogen Fixation with a Metallocene Mediator: Exploring pK_a Effects and Demonstrating Electrocatalysis. *J. Am. Chem. Soc.* **2018**, *140* (19), 6122–6129.
- (44) Sherbow, T. J.; Thompson, E. J.; Arnold, A.; Sayler, R. I.; Britt, R. D.; Berben, L. A. Electrochemical Reduction of N₂ to NH₃ at Low Potential by a Molecular Aluminum Complex. *Chem. – Eur. J.* **2019**, *25* (2), 454–458.
- (45) Markovic, N. M. Electrocatalysis: Interfacing Electrochemistry. *Nat. Mater.* **2013**, *12* (2), 101–102.
- (46) Bullock, R. M.; Das, A. K.; Appel, A. M. Surface Immobilization of Molecular Electrocatalysts for Energy Conversion. *Chem. – Eur. J.* **2017**, *23* (32), 7626–7641.

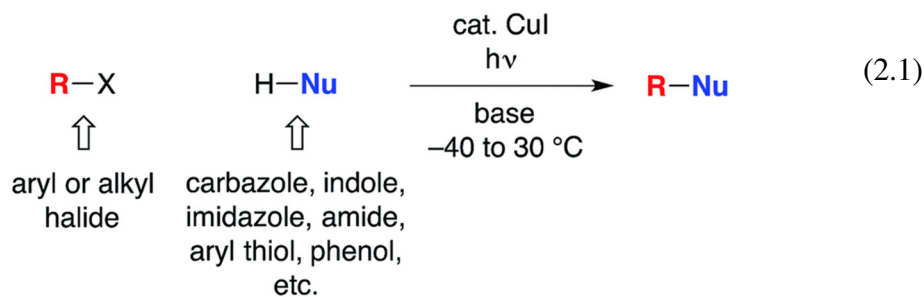
- (47) Axet, M. R.; Dechy-Cabaret, O.; Durand, J.; Gouygou, M.; Serp, P. Coordination Chemistry on Carbon Surfaces. *Coord. Chem. Rev.* **2016**, *308*, 236–345..
- (48) Kang, P.; Zhang, S.; Meyer, T. J.; Brookhart, M. Rapid Selective Electrocatalytic Reduction of Carbon Dioxide to Formate by an Iridium Pincer Catalyst Immobilized on Carbon Nanotube Electrodes. *Angew. Chem. Int. Ed.* **2014**, *53* (33), 8709–8713.
- (49) Maurin, A.; Robert, M. Noncovalent Immobilization of a Molecular Iron-Based Electrocatalyst on Carbon Electrodes for Selective, Efficient CO₂-to-CO Conversion in Water. *J. Am. Chem. Soc.* **2016**, *138* (8), 2492–2495.
- (50) Blakemore, J. D.; Gupta, A.; Warren, J. J.; Brunschwig, B. S.; Gray, H. B. Noncovalent Immobilization of Electrocatalysts on Carbon Electrodes for Fuel Production. *J. Am. Chem. Soc.* **2013**, *135* (49), 18288–18291.
- (51) Rosser, T. E.; Windle, C. D.; Reisner, E. Electrocatalytic and Solar-Driven CO₂ Reduction to CO with a Molecular Manganese Catalyst Immobilized on Mesoporous TiO₂. *Angew. Chem. Int. Ed.* **2016**, *55* (26), 7388–7392.
- (52) Yao, S. A.; Ruther, R. E.; Zhang, L.; Franking, R. A.; Hamers, R. J.; Berry, J. F. Covalent Attachment of Catalyst Molecules to Conductive Diamond: CO₂ Reduction Using “Smart” Electrodes. *J. Am. Chem. Soc.* **2012**, *134* (38), 15632–15635.
- (53) Kramer, W. W.; McCrory, C. C. L. Polymer Coordination Promotes Selective CO₂ Reduction by Cobalt Phthalocyanine. *Chem. Sci.* **2016**, *7* (4), 2506–2515.
- (54) Goff, A. L.; Artero, V.; Jusselme, B.; Tran, P. D.; Guillet, N.; Métafé, R.; Fihri, A.; Palacin, S.; Fontecave, M. From Hydrogenases to Noble Metal-Free Catalytic Nanomaterials for H₂ Production and Uptake. *Science* **2009**, *326* (5958), 1384–1387.

- (55) Rodriguez-Maciá, P.; Dutta, A.; Lubitz, W.; Shaw, W. J.; Rüdiger, O. Direct Comparison of the Performance of a Bio-Inspired Synthetic Nickel Catalyst and a [NiFe]-Hydrogenase, Both Covalently Attached to Electrodes. *Angew. Chem. Int. Ed.* **2015**, *54* (42), 12303–12307.
- (56) Zhanaidarova, A.; Moore, C. E.; Gembicky, M.; Kubiak, C. P. Covalent Attachment of [Ni(Alkynyl-Cyclam)]²⁺ Catalysts to Glassy Carbon Electrodes. *Chem. Commun.* **2018**, *54* (33), 4116–4119.
- (57) Zhanaidarova, A.; Ostericher, A. L.; Miller, C. J.; Jones, S. C.; Kubiak, C. P. Selective Reduction of CO₂ to CO by a Molecular Re(Ethynyl-Bpy)(CO)₃Cl Catalyst and Attachment to Carbon Electrode Surfaces. *Organometallics* **2019**, *38* (6), 1204–1207.

A MECHANISTIC INVESTIGATION OF PHOTOINDUCED, COPPER-
CATALYZED CROSS-COUPPLINGS OF ARYL THIOLS WITH ARYL
HALIDES

2.1 Introduction

The utility of cross-coupling chemistry has continued to expand at a rapid rate as novel or underexplored reaction pathways are exploited to achieve important new families of bond constructions.¹ We have recently reported that, in the presence of light and a simple copper catalyst, coupling reactions of a variety of nucleophiles (nitrogen, sulfur, oxygen, and carbon) with aryl or alkyl electrophiles can be accomplished under mild conditions (−40 to 30 °C; eqn 2.1).²⁻⁴



We have suggested the outline of a possible pathway for these processes (Figure 2.1, illustrated for C–S coupling),⁵ recognizing that the course of the cross-coupling is likely to vary with different coupling partners and reaction conditions. We have been interested in mechanistic similarities and dichotomies with photoredox catalysis, a mode of reactivity that has been the focus of great interest in recent years.⁶ For example, we have hypothesized that, distinct from a classical photoredox catalyst wherein a particular metal complex serves

exclusively as an electron donor/acceptor, in our processes the copper complex may play a role both in electron transfer and in the key bond-forming step (e.g., C–S bond construction in Figure 2.1).^{2a-d, 3, 7} Furthermore, the mechanism depicted in Figure 2.1 is not a radical-chain process; although non-chain pathways have frequently been invoked in earlier studies of photoredox catalysis,⁸ Yoon has recently concluded that, for three representative and mechanistically distinct transformations, the photoredox catalyst serves to initiate a chain reaction.⁹ In this report, we describe our first study focused primarily on the mechanism of a photoinduced, copper-mediated cross-coupling, specifically, an investigation of the stoichiometric coupling of an aryl iodide with a copper–thiolate (eqn 2.2).¹⁰

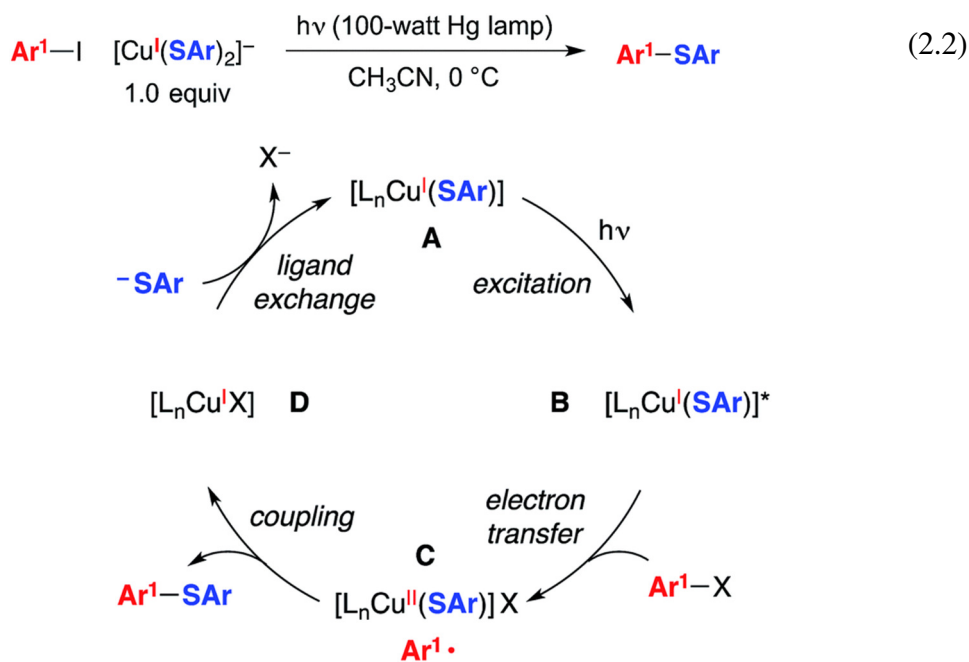
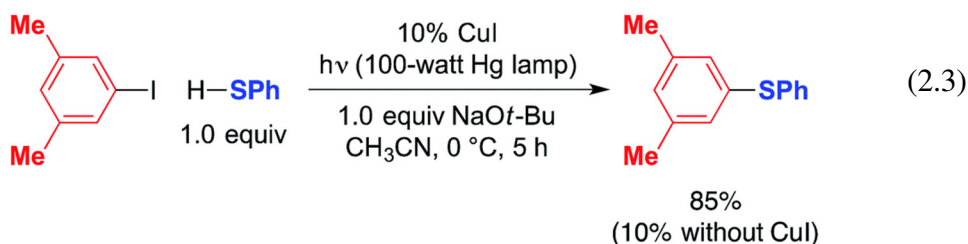


Figure 2.1: Outline of a possible catalytic cycle for photoinduced, copper-catalyzed cross-coupling: Coupling of an aryl radical with a copper(II)–thiolate as a key step.¹¹

2.2 Results and Discussion

2.2.1 Background

The photoinduced coupling of aryl thiols with aryl halides in liquid ammonia, in the absence of a catalyst, through an $S_{RN}1$ mechanism is well-established through the work of Bunnett.^{12–14} In our initial report, we observed that a model photoinduced cross-coupling proceeds significantly more rapidly in the presence of a copper catalyst than in its absence (eqn 2.3).^{2b}



Under our reported conditions, the reaction mixture is heterogeneous, with a substantial portion of the NaSPh present as a solid. We have determined that, when the same partners are coupled at much lower concentration in a homogeneous solution, the rates of product formation can be similar in the presence and in the absence of CuI.¹⁵ Thus, a copper-mediated pathway and a copper-free pathway for C–S bond formation are possible, and which one is dominant can depend on the relative concentration in solution of sodium versus copper thiolates (the latter are generally more soluble in CH_3CN). In the present investigation, we seek to gain insight into the copper-mediated pathway.

In the mechanistic framework that we have previously described (Figure 2.1), irradiation of a copper(I)–thiolate complex (A) leads to a photoexcited state (B). Electron transfer from B to the aryl halide furnishes a copper(II)–thiolate complex (C) and an aryl radical. Radical recombination then forms the C–S bond of the thioether, either directly¹⁶ or

through a copper(III) intermediate, and a copper(I)–halide complex (D). Displacement of the halide of complex D by thiolate then regenerates copper(I)–thiolate complex A.

Another mechanism under consideration largely follows the $S_{RN}1$ pathway for copper-free C–S coupling reactions,¹² the difference being that a photoexcited copper(I)–thiolate (B), rather than a photoexcited copper-free thiolate, serves as the initiating electron donor to the aryl halide, thereby generating a radical anion (F) that can participate in a chain reaction to form the thioether (Figure 2.3).¹⁷

We have also considered mechanisms that do not involve an organic radical as an intermediate. For example, in the pathway depicted in Figure 4, photoexcited complex B reacts with the aryl halide to cleave the C–X bond in a concerted process without the intermediacy of an aryl radical.¹⁸ Reductive elimination of the resulting copper(III) complex (G) leads to the thioether product (Ar^1-SAr) and copper(I)–halide adduct D. Ligand exchange then completes the catalytic cycle by regenerating copper(I)–thiolate A.

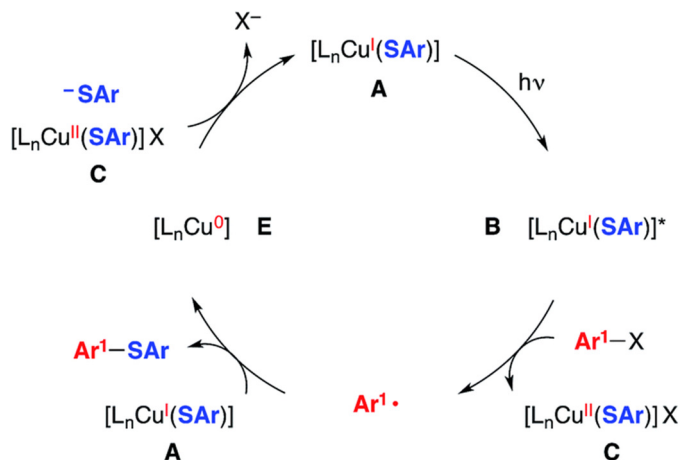
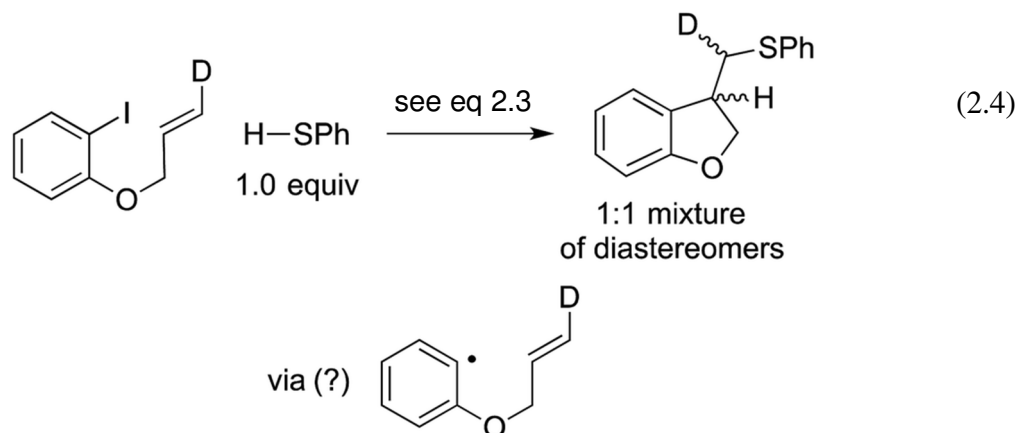


Figure 2.2: An alternative mechanism: coupling of an aryl radical with a copper(I)–thiolate as a key step.⁵

to form the thioether, as well as copper(0) (E).¹⁹ Comproportionation of copper(0) with copper(II)–thiolate C could regenerate copper(I)–thiolate A.

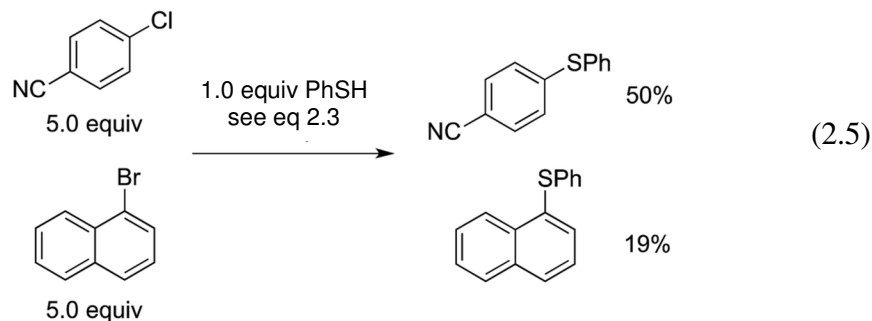
2.2.2 Previously reported mechanistic observations^{2b}

In our original report, we described cyclization/stereochemistry data (eqn 2.4) that are more readily accommodated by a radical/electron-transfer pathway (Figures 2.1–2.3) than by a concerted pathway (Figure 2.4) for C–X bond cleavage. Furthermore, in a relative-reactivity study (eqn 5), we determined that the aryl halide that is more easily reduced via electron transfer (4-chlorobenzonitrile; -2.03 V vs. SCE in DMF²¹) is more reactive than the one with the weaker C–X bond (1-bromonaphthalene; -2.17 V vs. SCE in DMF²¹); this contrasts with thermal (non-photoinduced) copper-catalyzed S-arylation, wherein essentially exclusive coupling of the aryl bromide is proposed to result from concerted oxidative addition.^{18, 22}



Our efforts to isolate a mononuclear $[\text{Cu}^{\text{I}}(\text{SPh})_2]^-$ complex (e.g., A in Figures 2.1–2.4), which we had detected in an ESI-MS study of a C–S coupling reaction, led instead to a copper(I)–thiolate cluster, $[\text{Cu}_5(\text{SPh})_7][\text{Na}(12\text{-crown-}4)_2]_2$. This cluster did, however, serve

as a suitable stoichiometric coupling partner with an aryl iodide, as well as an effective (pre)catalyst for a photoinduced C–S cross-coupling.



Although these observations are consistent with our initial working hypothesis for the mechanism of photoinduced, copper-catalyzed C–S cross-couplings (Figure 2.1), we concluded that a more detailed investigation was warranted.

2.2.3 Synthesis and characterization of a monomeric copper(I)–thiolate model complex



A copper(I)–thiolate (A) is the starting point in each of the pathways illustrated in Figure 2.1–2.4. For ease of analysis in the present investigation, we sought a model system of simple speciation (monomeric). As demonstrated by Tshuva, the use of a hindered arylthiolate (2,6-dimethylthiophenolate; SAr, Ar = 2,6-dimethylphenyl) can avoid the formation of a cluster;²³ furthermore, we had reported in our initial study that this arylthiolate serves as a suitable coupling partner in photoinduced C–S cross-couplings.^{2b} Reaction of mesitylcopper(I), 2,6-dimethylthiophenol, and NaOt-Bu in CH₃CN, followed by the addition

of 12-crown-4, provided the desired sodium salt, $[\text{Cu}^{\text{I}}(\text{SAr})_2][\text{Na}(12\text{-crown-4})_2]$ (**2.1**; “[$\text{Cu}^{\text{I}}(\text{SAr})_2$] Na^+ ”; eqn 2.6 and Figure 2.5).

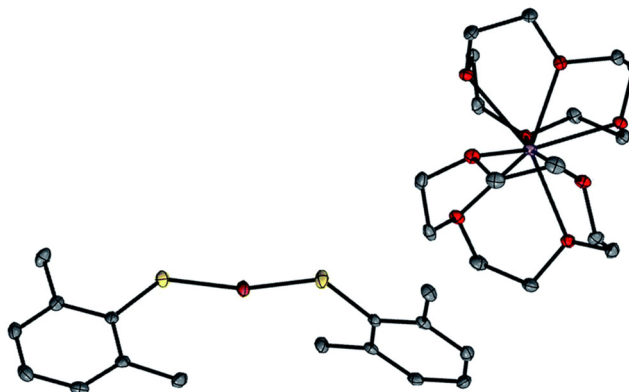
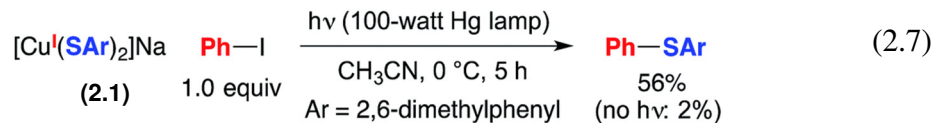


Figure 2.5: X-ray crystal structure of $[\text{Cu}^{\text{I}}(\text{SAr})_2][\text{Na}(12\text{-crown-4})_2]$ (**2.1**). Ellipsoids are shown at 50% probability, and hydrogen atoms have been omitted for clarity. Selected bond lengths and bond angle: Cu–S = 2.1477(5) Å and 2.1499(5) Å; S–Cu–S, 166.82(2)°.

Our available data are consistent with the suggestion that this copper(I)–thiolate is a monomer in solution, as in the solid state. On the basis of diffusion-ordered NMR spectroscopy (DOSY), we estimate the hydrodynamic radii of the anion and the cation to be 4.2 and 4.4 Å, respectively, which are comparable to the corresponding computed radii of 4.5 and 4.8 Å. Furthermore, the molar conductivity for complex **2.1** in acetonitrile, 128.5 S $\text{cm}^2 \text{mol}^{-1}$, falls within the range (120–160 S $\text{cm}^2 \text{mol}^{-1}$) for other coordination compounds that are 1:1 electrolytes.²⁴

NaSAr (Ar = 2,6-dimethylphenyl) is significantly more soluble in CH_3CN than is NaSPh; consequently, for the photoinduced coupling of NaSAr with Ph–I under our standard conditions, the rates of reaction in the absence and in the presence of CuI are similar, in contrast to our observations with NaSPh (eqn 2.3). Nevertheless, we have determined that

$[\text{Cu}^{\text{I}}(\text{SAr})_2]\text{Na}$ (**2.1**) couples at 0 °C with Ph-I in 56% yield, thereby substantiating the viability of photoinduced copper-mediated S-arylation with this model complex (eqn 2.7).



In an ESI-MS study of the coupling of ArSH with Ph-I under our standard copper-catalyzed cross-coupling conditions (eqn 2.3), we have detected an anion with a molecular weight of 337.2, which corresponds to that of $[\text{Cu}^{\text{I}}(\text{SAr})_2]^-$; under these conditions, we do not observe $[\text{Cu}^{\text{I}}(\text{SAr})_3]^{2-}$, despite the large excess of thiolate relative to copper. Furthermore, ^1H NMR and optical absorption spectra of complex **2.1** in the presence of excess thiolate, as well as DFT calculations,²⁵ indicate that formation of $[\text{Cu}^{\text{I}}(\text{SAr})_3]^{2-}$ is unfavorable. Collectively, our data suggest that complex **2.1** exists as a two-coordinate monomer in solution, even in the presence of excess thiolate.

2.2.4 Electrochemistry

We have examined through electrochemistry the redox behavior of $[\text{Cu}^{\text{I}}(\text{SAr})_2]\text{Na}$ (**2.1**) and of NaSAr (Figure 2.6). The cyclic voltammogram of complex **2.1** shows an irreversible oxidative feature at $E_p = -0.18\text{ V}$ vs. SCE that is also irreversible at $-20\text{ }^\circ\text{C}$ and at scan rates up to 1.5 V s^{-1} at $25\text{ }^\circ\text{C}$. Following oxidation of **2.1**, an irreversible feature is observed at -1.85 V vs. SCE, which corresponds to the reduction of bis(2,6-dimethylphenyl) disulfide (ArS-SAr), presumably formed from complex **2.1** upon electrochemical oxidation (oxidation of **2.1** with $[\text{FeCp}_2][\text{PF}_6]$ also leads to the formation of ArS-SAr).

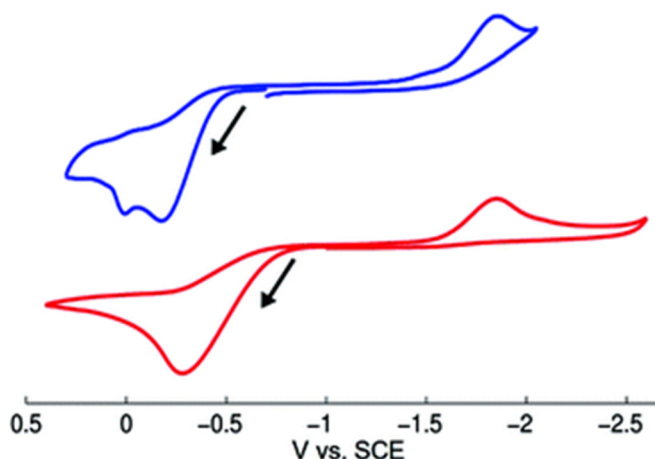


Figure 2.6: Cyclic voltammograms of $[\text{Cu}^{\text{I}}(\text{SAr})_2]\text{Na}$ (**2.1**; top) and of NaSAr (bottom). Conditions: scan rate: 100 mV s^{-1} ; supporting electrolyte: $0.08 \text{ M } [(n\text{-Bu})_4\text{N}][\text{B}(\text{C}_6\text{F}_5)_4]$; working electrode: glassy carbon; reference electrode: Ag/AgNO_3 (0.1 mM)/acetonitrile; auxiliary electrode: platinum wire; temperature: $25 \text{ }^\circ\text{C}$.

To gain insight into whether free thiolate, generated either by simple ligand dissociation or through irradiation, might play a significant role in stoichiometric reactions of complex **2.1**, we have monitored by cyclic voltammetry a solution of **2.1** (0.020 M) and $[(n\text{-Bu})_4\text{N}][\text{B}(\text{C}_6\text{F}_5)_4]$ as electrolyte in acetonitrile. The cyclic voltammogram is unchanged over 15 minutes of irradiation with a Hg lamp, suggesting that irradiation of complex **2.1** does not lead to the release of a detectable amount of free thiolate.

2.2.5 Photophysical study of $[\text{Cu}^{\text{I}}(\text{SAr})_2]\text{Na}$ (**2.1**)

Complex **2.1** absorbs strongly in the ultraviolet region (top of Figure 2.7), although only weakly at 365 nm ($\epsilon_{365} = 3 \text{ M}^{-1} \text{ cm}^{-1}$), a prominent emission band for the 100 watt Hg lamp used in our photoinduced C–S couplings.²⁶ The complex luminesces upon excitation at 355 nm with a lifetime of $\sim 7 \text{ } \mu\text{s}$ in acetonitrile, as determined by transient luminescence

spectroscopy (bottom of Figure 2.7). The lifetime of the emissive state does not change as a function of the observation wavelength, consistent with a single species being the source of luminescence. While the lack of a reversible $\text{Cu}^{\text{I}}/\text{Cu}^{\text{II}}$ redox couple precludes a true evaluation of the excited-state reduction potential for complex **2.1**, we estimate this potential to be -2.5 to -2.7 V vs. SCE on the basis of the first ground-state oxidative feature ($E_p = -0.18$ V vs. SCE) (see Electrochemistry) and an approximate E_{00} of $2.3\text{--}2.5$ eV.^{27,28} These data suggest that the excited state of complex **2.1** is sufficiently long-lived and reducing to engage in electron transfer with electrophiles such as aryl iodides (Ph-I: -1.91 V vs. SCE in DMF²¹).

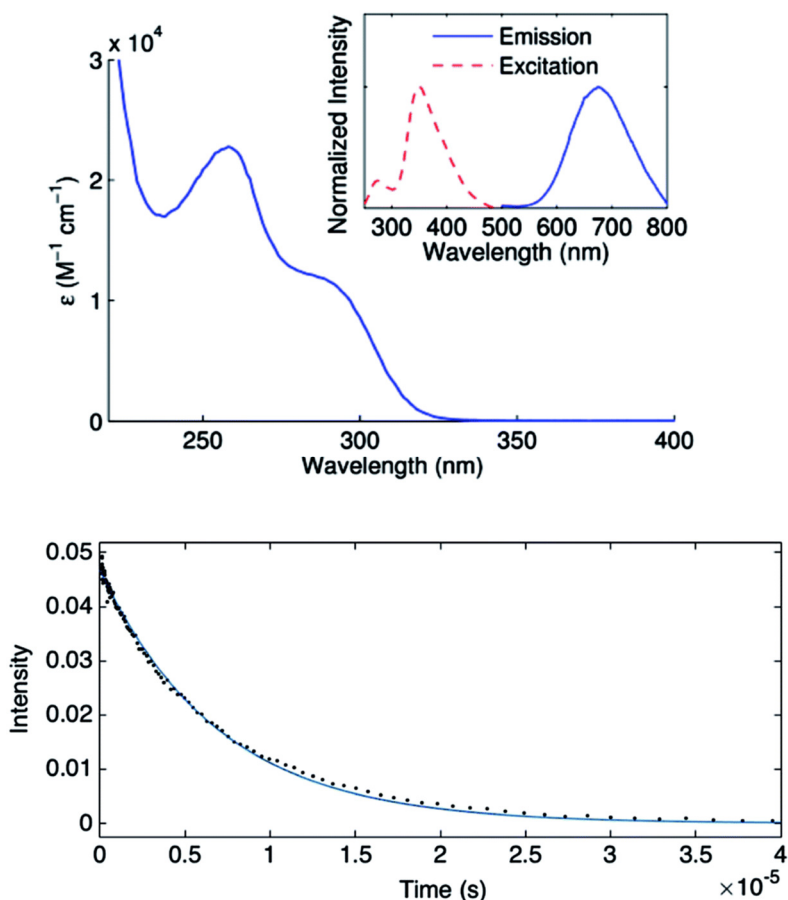


Figure 2.7: Top: Optical spectrum of [Cu^I(SAr)₂]Na (**2.1**) ($\lambda_{\text{max}} = 258$ nm, $\epsilon = 2.3 \times 10^4$ cm⁻¹ M⁻¹); inset: excitation spectrum at 675 nm emission (dashed line) and emission spectrum at 353 nm excitation (solid line); in acetonitrile at 25 °C. Bottom: Time-resolved decay of the luminescence intensity of **2.1***; in acetonitrile at 25 °C (25 μ M); Nd:YAG laser at 355 nm excitation; observation wavelength: 675 nm.

To gain insight into the predicted electronic structure of the excited state of complex **2.1**, we have performed time-dependent DFT calculations.²⁹ These calculations indicate that the lowest energy singlet state ($\lambda_{\text{calc}} = 325$ nm) consists of a transition from the HOMO (Cu–S antibonding) to the arene π^* (Figure 2.8). The population of a high-energy arene π^* orbital in the excited state is consistent with **2.1** being a potent photoreductant.

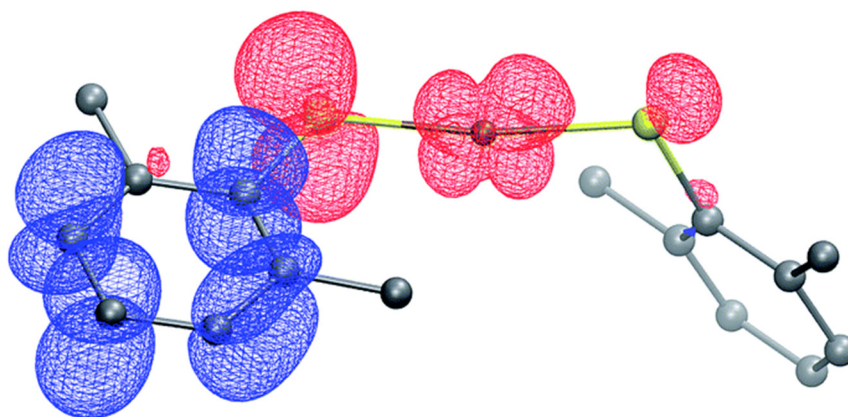


Figure 2.8: Difference density plot for the lowest energy absorption band of $[\text{Cu}^{\text{I}}(\text{SAr})_2]\text{Na}$ (**2.1**). The donor orbital is shown in red, and the acceptor orbital is shown in blue (isovalue = 0.02).

2.2.6 Stern–Volmer kinetic analysis

The mechanisms outlined in Figures 2.1–2.3 begin with electron transfer from a photoexcited copper(I)–thiolate (**B**) to the aryl halide. We have conducted a Stern–Volmer kinetic analysis of this elementary step, specifically, the reaction of the excited state of $[\text{Cu}^{\text{I}}(\text{SAr})_2]\text{Na}$ (**2.1**) with Ph–I (reduction potentials: $[\text{Cu}^{\text{I}}(\text{SAr})_2]^{-*}$: ~ -2.6 V; Ph–I: -1.91 V vs. SCE in DMF²¹), and we have determined that the rate constant for quenching is $8 \times 10^5 \text{ M}^{-1} \text{ s}^{-1}$. As expected, an increase in the concentration of Ph–I leads to a decrease in the lifetime of the excited state (Figure 2.9). The observed quenching results from electron transfer, not energy transfer; the emission spectrum of complex **2.1** exhibits no overlap with the absorption spectrum of Ph–I.^{30, 31}

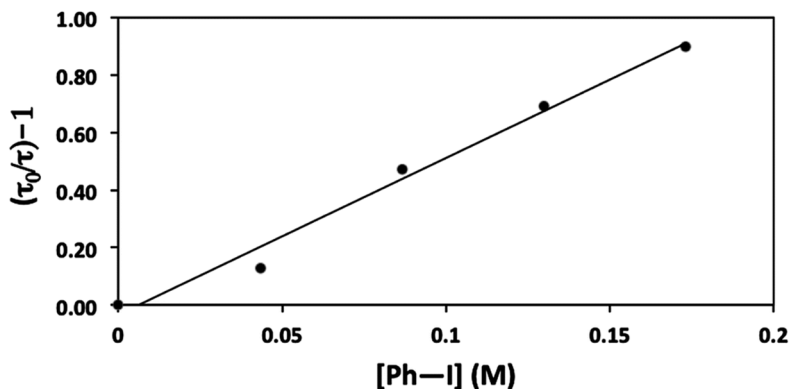


Figure 2.9: Stern–Volmer plot for the luminescence quenching of $[\text{Cu}^{\text{I}}(\text{SAr})_2]\text{Na}^*$ in the presence of Ph–I.

2.2.7 Consideration of a radical chain mechanism: quantum yield and chain length

We have established that the quantum yield (Φ) for the stoichiometric coupling of $[\text{Cu}^{\text{I}}(\text{SAr})_2]\text{Na}$ (**2.1**) with Ph–I when irradiated at 365 nm is 0.08(2),³² a value that can be accommodated either by a non-chain mechanism or by a chain mechanism with rapid chain termination. By dividing the quantum yield by the Stern–Volmer quenching fraction (Q), we have determined the chain length (the number of molecules of product formed per photoinduced electron-transfer event) for the C–S coupling of complex **2.1** with Ph–I to be 0.8 (eqn 2.8). This suggests that this cross-coupling proceeds via a non-chain pathway, as a chain mechanism would be expected to furnish more than one molecule of product from each photoinduced electron transfer. In contrast, Yoon concluded on the basis of a similar analysis that three representative reactions that involve photoredox catalysis proceed through a chain pathway.⁹

Φ = quantum yield = 0.08

Q = Stern–Volmer quenching fraction

$$\begin{aligned}
 &= \frac{k_q[\text{Ph-I}]}{\tau_0^{-1} + k_q[\text{Ph-I}]} \quad \begin{array}{l} \tau_0 = \text{excited-state lifetime of complex } \mathbf{1} \\ k_q = \text{rate of Stern–Volmer quenching of Ph-I} \end{array} \quad (2.8) \\
 &= \frac{(8 \times 10^5 \text{ M}^{-1}\text{s}^{-1})(0.02 \text{ M})}{(7 \times 10^{-6} \text{ s})^{-1} + (8 \times 10^5 \text{ M}^{-1}\text{s}^{-1})(0.02 \text{ M})} = 0.10 \\
 \text{chain length} &= \frac{\Phi}{Q} = 0.8
 \end{aligned}$$

2.2.8 Viability of coupling an aryl radical with a copper–thiolate

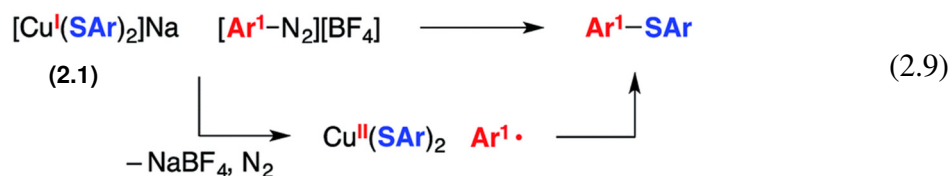
The mechanistic observations described above are consistent with the suggestion that an aryl radical is generated under our cross-coupling conditions. This intermediate could subsequently form a C–S bond by reacting with species such as a Cu(II)–thiolate (Figure 2.1) or a Cu(I)–thiolate (Figure 2.2). We sought insight into the viability of such couplings by exploring reactions of an aryldiazonium salt, which can readily be converted into an aryl radical via one-electron reduction.^{2d}

When $[\text{Cu}^{\text{I}}(\text{SAr})_2]\text{Na}$ (**2.1**; $E_p = -0.18 \text{ V vs. SCE}$) and 4-methoxyphenyldiazonium tetrafluoroborate ($E^\circ = 0.14 \text{ V vs. SCE}$ ³³) are allowed to react in CD_3CN at $-20 \text{ }^\circ\text{C}$ for 30 minutes, no coupling is evident by $^1\text{H NMR}$ spectroscopy (Table 2.1, entry 1). However, upon warming the mixture to room temperature for 30 minutes, C–S bond formation proceeds in 57% yield (entry 2). One possible pathway for this transformation begins with electron transfer from complex **2.1** to the aryldiazonium salt to afford a copper(II)–thiolate and $\text{Ar}^{\cdot}\text{N}_2$, which loses N_2 to generate an aryl radical that couples with the copper(II)–thiolate to form the C–S bond (eqn 2.9).³⁴

Table 2.1. Reactions of a copper–thiolate with an aryldiazonium salt.
$$\begin{array}{ccc}
 [\text{Cu}^{\text{I}}(\text{SAr})_2]\text{Na} & [\text{Ar}^1\text{-N}_2][\text{BF}_4] & \xrightarrow{\text{CH}_3\text{CN}} & [\text{Ar}^1\text{-SAr}] \\
 \text{(2.1)} & 1.0 \text{ equiv} & & \\
 & \text{Ar} = 2,6\text{-dimethylphenyl} & & \\
 & \text{Ar}^1 = p\text{-anisyl} & &
 \end{array}$$

entry	conditions	yield (%)
1	-20 °C, 30 min	<2 ^a
2	r.t., 30 min	57
3	1.1 equiv FeCp* ₂ , -20° C, 30 min	22
4	r.t., 30 min, 1.1 equiv [FeCp* ₂][BF ₄]	56

^a Run in CD₃CN; unreacted diazonium salt: >90%.



To assess the viability of the coupling of an aryl radical with a copper(I)–thiolate, we sought a reductant that would reduce the aryldiazonium salt and thereby generate an aryl radical under conditions in which copper(I)–thiolate **2.1** would not (CD₃CN, -20 °C; Table 2.1, entry 1). We determined that, in the presence of decamethylferrocene (FeCp*₂; E° = -0.12 V vs. SCE³⁵),³⁶ the aryldiazonium salt is completely consumed within 30 minutes at -20 °C, furnishing a mixture of compounds that includes a 22% yield of the C–S coupling product (entry 3). The low yield of the diarylsulfide indicates that under these conditions an aryl radical reacts inefficiently, at best, with a copper(I)–thiolate to form a C–S bond; control experiments suggest the alternative possibility that at least some of the cross-coupling product may be formed from reaction of the aryl radical with a small amount of copper(II)–

thiolate that is generated through a redox equilibrium between $\text{Cu}^{\text{I}}/\text{Fe}^{\text{III}}$ and $\text{Cu}^{\text{II}}/\text{Fe}^{\text{II}}$ as the ferrocenium ion is formed.³⁷ When the coupling illustrated in entry 2 is conducted in the presence of $[\text{FeCp}^*_2][\text{BF}_4]$ (entry 4), the yield of the diarylsulfide is essentially unchanged (56%; entry 2 versus entry 4). This result indicates that the ferrocenium ion that is produced in entry 3 is not responsible for the diminished yield in that reaction.

2.2.9 Rate of capture of an aryl radical by a copper–thiolate; in-cage versus out-of-cage coupling

To obtain insight into the rate of capture of the aryl radical intermediate, we have determined the ratio of uncyclized/cyclized products for C–S couplings of several aryl iodides that have previously been employed in radical-clock studies (Table 2.2).^{38,39} Our data indicate that capture of the aryl radical by a copper–thiolate occurs competitively with a cyclization process that has a first-order rate constant of $\sim 4 \times 10^8 \text{ s}^{-1}$ in benzene.

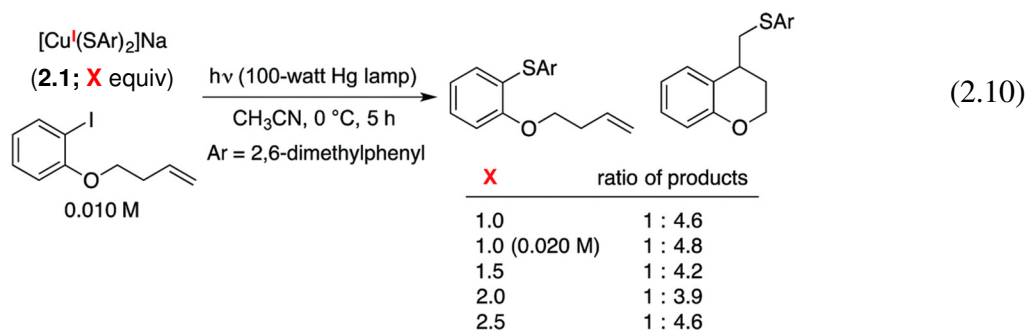
Table 2.2. Reaction of an aryl radical: Cyclization versus capture by a copper–thiolate.

$[\text{Cu}^{\text{I}}(\text{SAr})_2]\text{Na}$ (2.1)		$\text{Ar}^{\text{I}}-\text{I}$ 1.0 equiv	$\xrightarrow[\text{CH}_3\text{CN}, 0^\circ\text{C}, 5\text{ h}]{h\nu\text{ (100-watt Hg lamp)}}$	products
Ar = 2,6-dimethylphenyl				
$\text{Ar}^{\text{I}}-\text{I}$	products ^a			$k\text{ (s}^{-1}\text{)}^b$
	uncyclized	cyclized		
			1 : >20	9.6×10^9 (DMSO)
			1 : 5	4.2×10^8 (benzene)
			>20 : 1	8.0×10^5 (water)

^aRatio determined through GC analysis with dodecane as an internal standard (average of two experiments). ^bRate of cyclization of the aryl radical.

We have examined the relationship between the amount of $[\text{Cu}^{\text{I}}(\text{SAr})_2]\text{Na}$ (**2.1**) and the ratio of uncyclized/cyclized products, and we have determined that the product ratio remains essentially constant as we alter the quantity of complex **2.1** or the overall concentration (eqn 2.10). These observations can be accommodated by the mechanism illustrated in Figure 2.1, if C–S bond formation occurs between the aryl radical and copper(II)–thiolate C within the solvent cage (i.e., a single copper complex serves first as the

electron donor and then as the source of SAr). In contrast, for the mechanism illustrated in Figure 2.2, the cyclized/uncyclized product ratio should depend on parameters such as stoichiometry and concentration, since C–S bond formation requires the aryl radical to leave the solvent cage and to encounter a copper(I)–thiolate (i.e., one copper complex serves as the electron donor and a different copper complex provides the SAr group).^{40, 41}



2.2.10 Spectroscopic evidence for a copper(II)–thiolate

As noted above, electron transfer from an excited-state copper(I)–thiolate (B) to an aryl halide to generate a copper(II)–thiolate (C) is a key step in several of the mechanisms under consideration. Copper(II) species are $S = 1/2$ and therefore readily detected by EPR spectroscopy, as is the case for copper(II)–thiolate complexes.⁴² Indeed, photolysis of a solution of $[\text{Cu}^{\text{I}}(\text{SAr})_2]\text{Na}$ (**2.1**) in the presence of excess Ph–I and NaSAr in propionitrile:butyronitrile (1:1) at $-78\text{ }^\circ\text{C}$ results in a blue solution, the EPR spectrum of which is consistent with the presence of some amount of a copper(II)–thiolate radical (Figure 2.10).⁴³

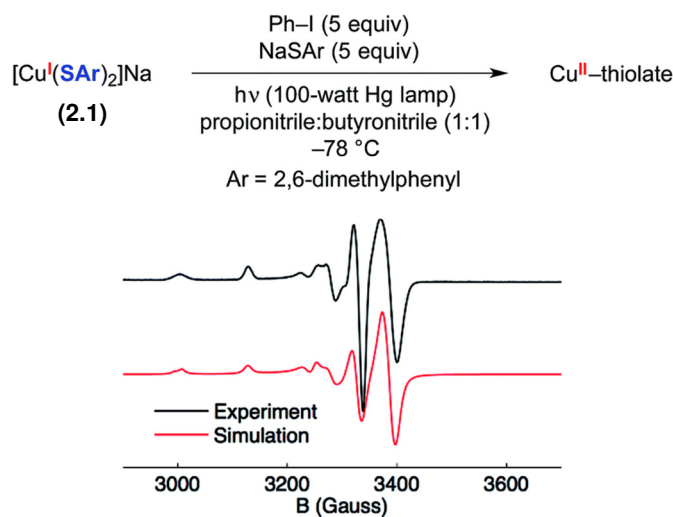


Figure 2.10: X-band EPR spectrum (77 K) of a coupling reaction following irradiation for 5 min. Simulation parameters: $g_1 = 2.022$, $g_2 = 2.032$, $g_3 = 2.104$, $A_1(\text{Cu}) = 85$ MHz, $A_2(\text{Cu}) = 130$ MHz, and $A_3(\text{Cu}) = 360$ MHz.

The four-line hyperfine coupling is consistent with an $I = 3/2$ paramagnetic copper complex with a single metal center. The spectrum shows modest g anisotropy compared to other copper(II)–thiolate complexes,⁴² which is consistent with a highly covalent Cu–S interaction.⁴⁴ This suggests that significant radical character resides in sulfur p orbitals, and DFT calculations support this assessment (see below).

Optical spectroscopy can serve as an additional technique for characterizing the putative copper(II)–thiolate. Upon irradiating complex **2.1** in the presence of Ph–I and NaSAr in propionitrile at -78 °C, a feature at 582 nm is observed (Figure 2.11), which is consistent with the blue color of the reaction mixture. This feature is near the range found for sulfur-rich copper(II) proteins (593 to 610 nm).⁴⁵

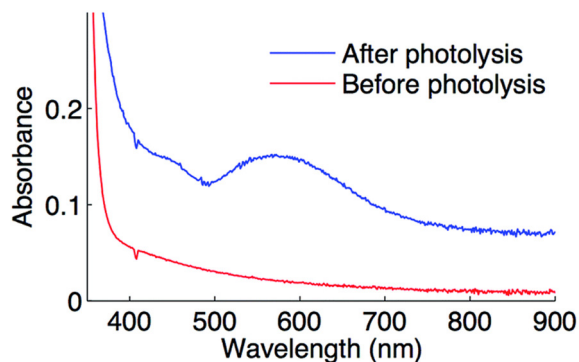
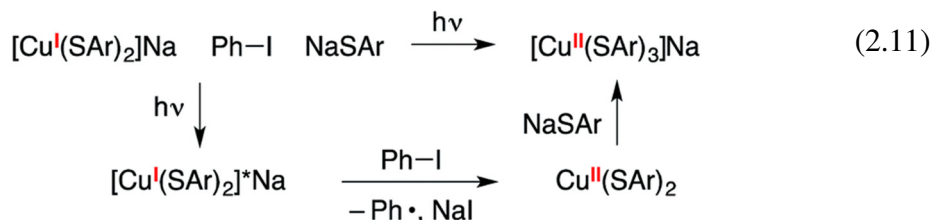


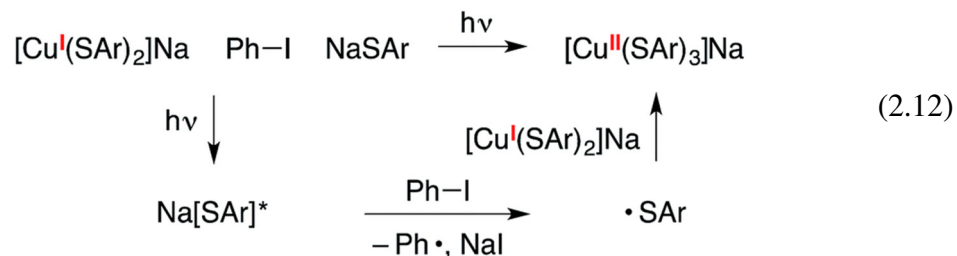
Figure 2.11: Optical spectrum of a coupling reaction prior to photolysis (red) and after photolysis (blue) in propionitrile at $-78\text{ }^{\circ}\text{C}$.

While the above data provide strong evidence for the generation of a copper(II)–thiolate radical upon photolysis of a mixture of complex **2.1**, Ph–I, and NaSAr, they do not identify the specific paramagnetic copper species, and further characterization is complicated by its instability even at $-78\text{ }^{\circ}\text{C}$. The presence not only of Ph–I, but also of NaSAr, is required for detection of this copper(II)–thiolate radical by optical and by EPR spectroscopy. In view of the need for exogenous thiolate, we hypothesize that a copper(II) tris(thiolate), $[\text{Cu}^{\text{II}}(\text{SAr})_3]^-$, may be formed, e.g., via electron transfer from $[\text{Cu}^{\text{I}}(\text{SAr})_2]^{-*}$ to the aryl halide to form $\text{Cu}^{\text{II}}(\text{SAr})_2$, followed by trapping by NaSAr (eqn 2.11).⁴⁶ DFT calculations suggest that binding of an arylthiolate to $\text{Cu}^{\text{II}}(\text{SAr})_2$ is exergonic by $\sim 4\text{ kcal mol}^{-1}$.^{47, 48}



Alternatively, the copper(II) tris(thiolate), $[\text{Cu}^{\text{II}}(\text{SAr})_3]^-$, could be generated by electron transfer to Ph–I from the excited state of NaSAr, followed by coupling of the thiyl

radical with $[\text{Cu}^{\text{I}}(\text{SAr})_2]^-$ (eqn 2.12). Our observations to date do not allow us to definitively distinguish between these two pathways for the formation of putative $[\text{Cu}^{\text{II}}(\text{SAr})_3]^-$.



DFT calculations of $[\text{Cu}^{\text{II}}(\text{SAr})_3]^-$ and of $\text{Cu}^{\text{II}}(\text{SAr})_2$ predict that significant spin density would reside on the thiolate ligands for either compound, which suggests that C-S bond formation could occur through direct reaction of the aryl radical with the copper-bound thiolate ($[\text{Cu}^{\text{II}}(\text{SAr})_3]^-$: Cu 0.23e⁻, 3S 0.57e⁻; $\text{Cu}^{\text{II}}(\text{SAr})_2$: Cu 0.14e⁻, 2S 0.63e⁻; Figure 2.12).

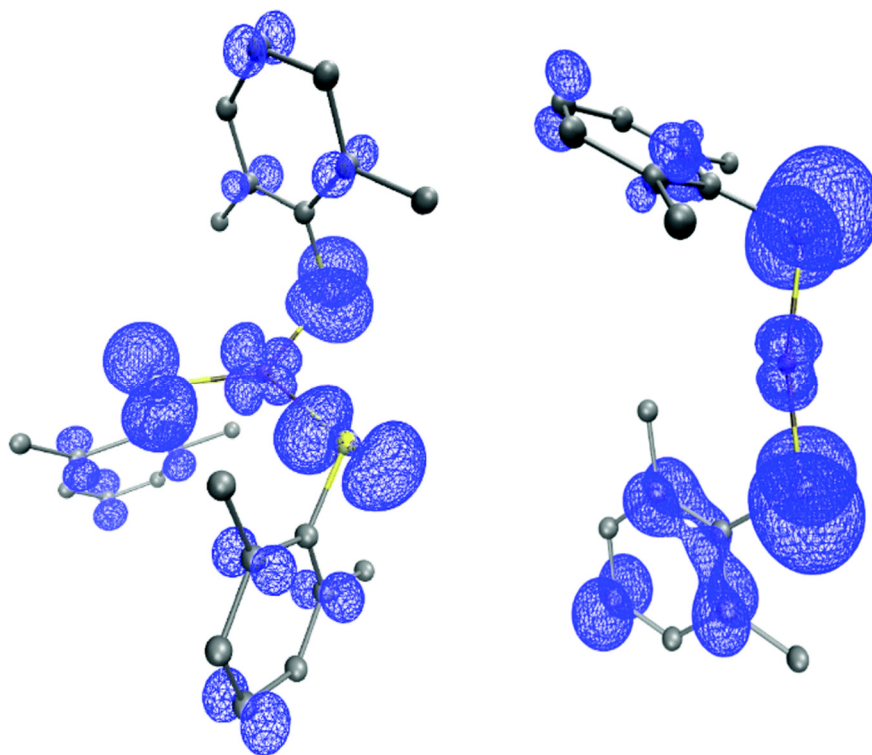


Figure 2.12: Spin density plots (0.002 isocontours) of $[\text{Cu}^{\text{II}}(\text{SAr})_3]^-$ (left) and $\text{Cu}^{\text{II}}(\text{SAr})_2$ (right).

2.3 Conclusions

In this report, we describe the first detailed mechanistic investigation of one of the photoinduced, copper-mediated cross-couplings that we have developed, specifically, the coupling of a thiol with an aryl iodide. Due to the existence of a parallel, copper-free C–S bond-forming pathway, we have focused our attention on understanding the stoichiometric chemistry of a key proposed intermediate, $[\text{Cu}^{\text{I}}(\text{SAr})_2]^-$ (Ar = 2,6-dimethylphenyl); our observations to date are consistent with the viability of the elementary steps outlined in Figures 2.1 (A \rightarrow D).

We have established that $[\text{Cu}^{\text{I}}(\text{SAr})_2]\text{Na}$ (**2.1**) is a two-coordinate monomer both in the solid state and in solution, and we have detected $[\text{Cu}^{\text{I}}(\text{SAr})_2]^-$ through ESI-MS under

cross-coupling conditions. Complex **2.1** undergoes excitation upon irradiation at 365 nm (a prominent emission band of a Hg lamp), and it luminesces with a lifetime of $\sim 7 \mu\text{s}$; we estimate its excited-state reduction potential to be $\sim -2.6 \text{ V}$ vs. SCE. Through a Stern–Volmer study, we have determined that the excited state is effectively quenched by Ph–I, as expected on the basis of its reduction potential; correspondingly, complex **2.1** reacts with Ph–I upon irradiation to afford the C–S coupling product. By employing actinometry, we have established that the chain length for the coupling of complex **2.1** with Ph–I is 0.8, indicating a non-chain mechanism. Our EPR and optical spectroscopy data suggest that a copper(II)–thiolate is formed when complex **2.1** is irradiated in the presence of Ph–I and NaSAr. Furthermore, through the use of an aryldiazonium salt, we have independently generated an aryl radical in the presence of copper(I)– and copper(II)–thiolates, and we have provided evidence that C–S bond formation is more efficient in the case of a copper(II)–thiolate. Finally, with the aid of radical clocks, we have established that C–S bond formation likely occurs via an in-cage mechanism in which a single copper complex serves both as an electron donor ($\text{Cu}^{\text{I}} \rightarrow \text{Cu}^{\text{II}}$) and a source of SAr (copper(II)–thiolate). Thus, the available data support the viability of the elementary steps for photoinduced C–S coupling that are illustrated in Figure 2.1 (A \rightarrow D), a mechanism that is distinct from most applications of photoredox catalysts in organic synthesis; other C–S coupling pathways, for example involving initial photoreduction of the aryl halide by a photoexcited copper-free thiolate, may also be operative. Our current efforts are directed at evaluating the degree to which the mechanism illustrated in Figure 2.1, or alternative mechanisms, applies to other photoinduced, copper-catalyzed cross-couplings.

2.4 References

- (1) For recent monographs, see: (a) T. Colacot, *New Trends in Cross-Coupling*, Royal Society of Chemistry, Cambridge, 2015; (b) A. de Meijere and M. Oestreich, *Metal-Catalyzed Cross-Coupling Reactions and More*, Wiley-VCH, Weinheim, 2014; (c) G. Evano and N. Blanchard, *Copper-Mediated Cross-Coupling Reactions*, John Wiley & Sons, Hoboken, NJ, 2014.
- (2) Arylations: (a) Carbazoles as nucleophiles: Creutz, S. E.; Lotito, K. J.; Fu, G. C.; Peters, J. C. Photoinduced Ullmann C–N Coupling: Demonstrating the Viability of a Radical Pathway. *Science* **2012**, *338* (6107), 647–651.; (b) Aryl thiols as nucleophiles: Uyeda, C.; Tan, Y.; Fu, G. C.; Peters, J. C. A New Family of Nucleophiles for Photoinduced, Copper-Catalyzed Cross-Couplings via Single-Electron Transfer: Reactions of Thiols with Aryl Halides Under Mild Conditions (0 °C). *J. Am. Chem. Soc.* **2013**, *135* (25), 9548–9552.; (c) Heteroaromatic nitrogen nucleophiles: Ziegler, D. T.; Choi, J.; Muñoz-Molina, J. M.; Bissember, A. C.; Peters, J. C.; Fu, G. C. A Versatile Approach to Ullmann C–N Couplings at Room Temperature: New Families of Nucleophiles and Electrophiles for Photoinduced, Copper-Catalyzed Processes. *J. Am. Chem. Soc.* **2013**, *135* (35), 13107–13112.; (d) Phenols as nucleophiles: Tan, Y.; Muñoz-Molina, J. M.; Fu, G. C.; Peters, J. C. Oxygen Nucleophiles as Reaction Partners in Photoinduced, Copper-Catalyzed Cross-Couplings: O-Arylations of Phenols at Room Temperature. *Chem. Sci.* **2014**, *5* (7), 2831–2835.; (e) For a related study, see: Yoo, W.-J.; Tsukamoto, T.; Kobayashi, S. Visible Light-Mediated Ullmann-Type C–N Coupling Reactions of

Carbazole Derivatives and Aryl Iodides. *Org. Lett.* **2015**, *17* (14), 3640–3642.

(carbazoles as nucleophiles).

- (3) Alkylations: (a) Carbazoles as nucleophiles: Bissember, A. C.; Lundgren, R. J.; Creutz, S. E.; Peters, J. C.; Fu, G. C. Transition-Metal-Catalyzed Alkylations of Amines with Alkyl Halides: Photoinduced, Copper-Catalyzed Couplings of Carbazoles. *Angew. Chem. Int. Ed.* **2013**, *52* (19), 5129–5133.; (b) Amides as nucleophiles: Do, H.-Q.; Bachman, S.; Bissember, A. C.; Peters, J. C.; Fu, G. C. Photoinduced, Copper-Catalyzed Alkylation of Amides with Unactivated Secondary Alkyl Halides at Room Temperature. *J. Am. Chem. Soc.* **2014**, *136* (5), 2162–2167.; (c) Cyanide as nucleophile: Ratani, T. S.; Bachman, S.; Fu, G. C.; Peters, J. C. Photoinduced, Copper-Catalyzed Carbon–Carbon Bond Formation with Alkyl Electrophiles: Cyanation of Unactivated Secondary Alkyl Chlorides at Room Temperature. *J. Am. Chem. Soc.* **2015**, *137* (43), 13902–13907.
- (4) For recent overviews of photoinduced, copper-catalyzed reactions, see: (a) Majek, M.; Jacobi von Wangelin, A. Ambient-Light-Mediated Copper-Catalyzed C–C and C–N Bond Formation. *Angew. Chem.-Int. Ed.* **2013**, *52* (23), 5919–5921.; (b) Paria, S.; Reiser, O. Copper in Photocatalysis. *ChemCatChem* **2014**, *6* (9), 2477–2483.
- (5) For the sake of simplicity in Figures 2.1–2.4, the copper complexes are shown without charges, and all processes are depicted as being irreversible. Halides (X) may be bound as inner-sphere or as outer-sphere ligands.
- (6) For recent reviews, see: (a) Prier, C. K.; Rankic, D. A.; MacMillan, D. W. C. Visible Light Photoredox Catalysis with Transition Metal Complexes: Applications in Organic Synthesis. *Chem. Rev.* **2013**, *113* (7), 5322–5363.; (b) Schultz, D. M.; Yoon,

T. P. Solar Synthesis: Prospects in Visible Light Photocatalysis. *Science* **2014**, *343* (6174), 985.

- (7) For a previous example of a transition-metal photoredox catalyst that also participates in bond formation, see: Huo, H.; Shen, X.; Wang, C.; Zhang, L.; Roese, P.; Chen, L.-A.; Harms, K.; Marsch, M.; Hilt, G.; Meggers, E. Asymmetric Photoredox Transition-Metal Catalysis Activated by Visible Light. *Nature* **2014**, *515* (7525), 100–103.
- (8) For example, see: Nicewicz, D. A.; MacMillan, D. W. C. Merging Photoredox Catalysis with Organocatalysis: The Direct Asymmetric Alkylation of Aldehydes. *Science* **2008**, *322* (5898), 77–80.
- (9) Cismesia, M. A.; Yoon, T. P. Characterizing Chain Processes in Visible Light Photoredox Catalysis. *Chem. Sci.* **2015**, *6* (10), 5426–5434.
- (10) For a recent review with leading references on metalcatalyzed cross-couplings to form C–S bonds, see: Lee, C.-F.; Liu, Y.-C.; Badsara, S. S. Transition-Metal-Catalyzed C-S Bond Coupling Reaction. *Chem.-Asian J.* **2014**, *9* (3), 706–722.
- (11) Although not explicitly shown, capture of $[L_nCu^{II}(SAr)]X$ by Ar^1 could generate a Cu(III) intermediate, $[L_nCu^{III}(Ar^1)(SAr)]X$, which could then reductively eliminate to afford Ar^1-SAr and complex D.
- (12) Bunnett, J.; Creary, X. Arylation of Arenethiolate Ions by $S_{RN}1$ Mechanism – Convenient Synthesis of Diary Sulfides. *J. Org. Chem.* **1974**, *39* (21), 3173–3174.
- (13) For early overviews of $S_{RN}1$ reactions, see: (a) Bunnett, J. Aromatic-Substitution by $S_{RN}1$ Mechanism. *Acc. Chem. Res.* **1978**, *11* (11), 413–420.; (b) J. Pinson and J. M.

Saveant, in *Electroorganic Synthesis*, ed. R. D. Little and N. L. Weinbert, Dekker, New York, 1991.

- (14) For reviews of photoinduced $S_{RN}1$ reactions, see: (a) M. E. Buden, S. E. Martin and R. A. Rossi, in *CRC Handbook of Organic Photochemistry and Photobiology*, ed. A. Griesbeck, M. Oelgemoller and F. Ghetti, CRC Press, Boca Raton, Florida, 2012, pp. 347–368; (b) J. I. Berdagi, V. A. Vaillard and R. A. Rossi, in *Encyclopedia of Radicals in Chemistry, Biology and Materials*, ed. C. Chatgililoglu and A. Studer, John Wiley & Sons, Chichester, U.K, 2012, ch. 14; (c) A. B. Peñeñory; J. E. Argüello, in *Handbook of Synthetic Photochemistry*, ed. A. Albini and M. Fagnoni, Wiley-VCH, Weinheim, Germany, 2010, ch. 10; (d) W. R. Bowman, in *Photoinduced Electron Transfer*, ed. M. A. Fox and M. Chanon, Elsevier, Amsterdam, 1990, pp. 487–552.
- (15) For additional information, see the Appendix A. For other classes of nucleophiles that we have examined, the rate in the presence of copper is significantly greater than in the absence of copper. For example, see ref. 2 and 3.
- (16) For early examples of copper-mediated C–S coupling processes that have been suggested to proceed without the formation of a Cu(III) intermediate, see: (a) Jenkins, C.; Kochi, J. Ligand Transfer of Halides (Cl, Br, I) and Pseudohalides (SCN, N₃, CN) from Copper(II) to Alkyl Radicals. *J. Org. Chem.* **1971**, *36* (21), 3095; (b) Jenkins, C.; Kochi, J. Homolytic and Ionic Mechanisms in Ligand-Transfer Oxidation of Alkyl Radicals by Copper(II) Halides and Pseudohalides. *J. Am. Chem. Soc.* **1972**, *94* (3), 856.

- (17) For an example of a non-chain process, see: Ahbala, M.; Hapiot, P.; Houmam, A.; Jouini, M.; Pinson, J.; Saveant, J. Nonchain Processes in Nucleophilic Substitutions Triggered by Electron Transfer ($S_{RN}1$) - Photochemical and Electrochemical Induction of the Substitution of 1-Iodoadamantane by Arenethiolate Ions. *J. Am. Chem. Soc.* **1995**, *117* (46), 11488–11498.
- (18) A concerted pathway for C–X bond cleavage is generally invoked in thermal (non-photoinduced) copper-catalyzed cross-couplings. For example, see: (a) Chen, C.; Weng, Z.; Hartwig, J. F. Synthesis of Copper(I) Thiolate Complexes in the Thioetherification of Aryl Halides. *Organometallics* **2012**, *31* (22), 8031–8037.; (b) Font, M.; Parella, T.; Costas, M.; Ribas, X. Catalytic C–S, C–Se, and C–P Cross-Coupling Reactions Mediated by a Cu^I/Cu^{III} Redox Cycle. *Organometallics* **2012**, *31* (22), 7976–7982.
- (19) Copper(0) “complex” E could be copper metal or a formal copper(0) complex that bears a redox-active ligand.
- (20) A step-wise ET process whereby $[L_nCu^II(SAr)]X$ is generated and then captured by Ar^I to generate G is also plausible. See also ref. 11.
- (21) Enemaerke, R.; Christensen, T.; Jensen, H.; Daasbjerg, K. Application of a New Kinetic Method in the Investigation of Cleavage Reactions of Haloaromatic Radical Anions. *J. Chem. Soc.-Perkin Trans. 2* **2001**, No. 9, 1620–1630.
- (22) For a mechanism wherein C–X bond cleavage occurs through halogen-atom transfer, 1-bromonaphthalene would generally be expected to be more reactive than 4-chlorobenzonitrile.

- (23) Zeevi, S.; Tshuva, E. Y. Synthesis and X-Ray Characterization of Mono- and Polynuclear Thiolatocopper(I) Complexes: The Effect of Steric Bulk on Coordination Number and Nuclearity. *Eur. J. Inorg. Chem.* **2007**, 2007 (34), 5369–5376. These workers have crystallographically characterized [CuI(SAr)₂][NEt₄].
- (24) Geary, W. J. The Use of Conductivity Measurements in Organic Solvents for the Characterisation of Coordination Compounds. *Coord. Chem. Rev.* **1971**, 7 (1), 81–122.
- (25) A DFT study indicates that binding of thiolate to [Cu^I(SAr)₂]⁻ to produce [Cu^I(SAr)₃]²⁻ is unfavorable by ~20 kcal mol⁻¹ (see the Appendix A).
- (26) Less than 5% decomposition of complex **2.1** was observed after irradiation (Hg lamp) in CH₃CN at 0 °C for five hours.
- (27) The lower limit of this range is based on the onset of emission, and the upper limit of this range is calculated from the midpoint of the maxima of the emission and excitation spectra (inset of Figure 2.7).
- (28) Rehm, D.; Weller, A. Kinetics of Fluorescence Quenching by Electron and H-atom Transfer. *Isr. J. Chem.* **1970**, 8 (2), 259.
- (29) Time-dependent DFT calculations were performed using the BP86 functional within the Tamm–Dancoff approximation employing the def2-TZVP basis set. The 50 lowest-lying singlet excited states were calculated, based on the DFT-optimized geometry of complex **2.1**.
- (30) Ferguson, J., Iredale, T. Low-Temperature Absorption and Phosphorescence Spectra of Some Iodo-Compounds. *J. Chem. Soc.* **1953**, 2959–2966

- (31) The triplet state of Ph-I is 3.5–3.6 eV (see ref. 30), whereas the triplet-state energy of **2.1*** is 1.8 eV based on an emission maximum of 675 nm. These data exclude the possibility of Dexter energy transfer.
- (32) For an example of an earlier determination of the quantum yield of a photoinduced coupling of a sulfur nucleophile with an aryl halide, see: Schmidt, L. C.; Argüello, J. E.; Peñeñory, A. B. Nature of the Chain Propagation in the Photostimulated Reaction of 1-Bromonaphthalene with Sulfur-Centered Nucleophiles. *J. Org. Chem.* **2007**, *72* (8), 2936–2944.
- (33) Elofson, R.; Gadallah, F. Substituent Effects in Polarography of Aromatic Diazonium Salts. *J. Org. Chem.* **1969**, *34* (4), 854.
- (34) We have investigated the possibility that C–S bond formation is occurring through a nucleophilic aromatic substitution reaction ($\text{S}_{\text{N}}\text{Ar}$) of the copper(I)–thiolate with the aryldiazonium salt. For the cross-coupling of complex **2.1** with an aryldiazonium salt that bears a pendant olefin that is suitably positioned for intramolecular addition by an aryl radical, we observe none of the “direct” coupling product, indicating that substitution via an $\text{S}_{\text{N}}\text{Ar}$ pathway is not favored under these conditions (see Appendix A).
- (35) Robbins, J. L.; Edelstein, N.; Spencer, B.; Smart, J. C. Syntheses and Electronic Structures of Decamethylmetallocenes. *J. Am. Chem. Soc.* **1982**, *104* (7), 1882–1893.
- (36) When the aryldiazonium salt is mixed with FeCp^*_2 in CD_3CN at $-20\text{ }^\circ\text{C}$ for 30 minutes, anisole is produced in ~85% yield.
- (37) For details, see Appendix A.

- (38) Radical cyclization rates: (a) Entries 1 and 2: Annunziata, A.; Galli, C.; Marinelli, M.; Pau, T. Determination of Rate Constants for the Reaction of Aryl Radicals with Enolate Ions. *Eur. J. Org. Chem.* **2001**, No. 7, 1323–1329; (b) Entry 3: Hanson, P.; Hammond, R.; Goodacre, P.; Purcell, J.; Timms, A. Sandmeyer Reactions 2. Estimation of Absolute Rate Constants for Some Hydrogen-Transfer Reactions and for the Transfer of Water Ligands on Cu(II) to Aryl Radicals by Use of a Pschorr Radical Clock. *J. Chem. Soc.-Perkin Trans. 2* **1994**, No. 4, 691–696.
- (39) We have conducted control experiments that establish that these aryl iodides are stable to irradiation under the indicated conditions.
- (40) When the cross-coupling illustrated in entry 2 of Table 2.1 is conducted at different concentrations (0.010 M versus 0.0050 M), the yield of the coupling product does not change, which is also consistent with a single copper complex serving as the electron donor and the source of SAr.
- (41) When the cross-coupling illustrated in eqn 2.10 is conducted with NaSAr in place of $[\text{Cu}^{\text{I}}(\text{SAr})_2]\text{Na}$, a different ratio (1 : 18) of uncyclized : cyclized products is observed, consistent with the suggestion that different thiolates (copper versus sodium) are coupling with the organic radical in the two processes.
- (42) For example, see: (a) Holland, P. L.; Tolman, W. B. Three-Coordinate Cu(II) Complexes: Structural Models of Trigonal-Planar Type 1 Copper Protein Active Sites. *J. Am. Chem. Soc.* **1999**, *121* (31), 7270–7271; (b) Holland, P.; Tolman, W. A Structural Model of the Type 1 Copper Protein Active Site: $\text{N}_2\text{S}(\text{Thiolate})\text{S}(\text{Thioether})$ Ligation in a Cu(II) Complex. *J. Am. Chem. Soc.* **2000**, *122* (26), 6331–6332.

- (43) As determined by spin quantification, the copper(II) species is present at a concentration of 0.2 mM, which corresponds to ~5% of the starting copper(I) complex.
- (44) Chen, P.; Fujisawa, K.; Solomon, E. Spectroscopic and Theoretical Studies of Mononuclear Copper(II) Alkyl- and Hydroperoxo Complexes: Electronic Structure Contributions to Reactivity. *J. Am. Chem. Soc.* **2000**, *122* (41), 10177–10193.
- (45) Solomon, E.; Baldwin, M.; Lowery, M. Electronic Structures of Active Sites in Copper Proteins – Contributions to Reactivity. *Chem. Rev.* **1992**, *92* (4), 521–542.
- (46) Intermolecular trapping of $\text{Cu}^{\text{II}}(\text{SAr})_2$ by free thiolate requires cage escape by the aryl radical generated via electron transfer to Ar-I. While our radical-clock studies are most consistent with in-cage recombination between a copper(II)–thiolate and an aryl radical at 0° C, bimolecular reactions that follow Eyring behavior can, when there is no coulombic term and the viscosity change is not dramatic, be expected to exhibit enhanced cage escape as the temperature is lowered in fluid solution, according to the Eigen equation (see: Olmsted, J.; Meyer, T. Factors Affecting Cage Escape Yields Following Electron-Transfer Quenching. *J. Phys. Chem.* **1987**, *91* (6), 1649–1655). In general, the temperature dependence of the partitioning between in-cage versus out-of-cage radical pathways is challenging to predict (see Appendix A for additional information).
- (47) According to a DFT calculation, binding of iodide anion to $\text{Cu}^{\text{II}}(\text{SAr})_2$ is approximately thermoneutral (see Appendix A).
- (48) We have examined whether evidence for $[\text{Cu}^{\text{II}}(\text{SAr})_3]$ might be obtained, if electrochemical oxidation of $[\text{Cu}^{\text{I}}(\text{SAr})_2]\text{Na}$ (**2.1**) is conducted in the presence of

NaSAr. However, the cyclic voltammogram of complex **2.1** is unchanged in the presence of 10 equivalents of NaSAr, and its oxidation remains irreversible. This result is consistent with our expectations. As evident in Figure 2.6, the onset for the oxidation feature of NaSAr is cathodically shifted relative to that for complex **2.1**.

*Chapter 3***ELECTROCHEMICAL AMMONIA PRODUCTION BY A SURFACE-
ATTACHED IRON COMPLEX****3.1 INTRODUCTION**

The reduction of N_2 to NH_3 is an essential transformation for life and is performed on a massive scale both industrially and biologically.¹⁻³ The high stability of the $N\equiv N$ triple bond necessitates a catalyst to achieve this transformation selectively.⁴ Assembling systems for the conversion of solar energy to NH_3 requires the development of electrodes capable of selective reduction of N_2 to NH_3 .⁵⁻⁸ Inorganic complexes have attracted significant attention as homogeneous catalysts for N_2 reduction, although electrochemical N_2 reduction by molecular complexes remains challenging.⁹ Immobilization of molecular catalysts on electrode surfaces presents further challenges; immobilization methods require harsh conditions with limited functional group compatibility and are often not general.¹⁰ In principle, attachment of molecular catalysts onto conducting electrodes allows their thorough investigation by electrochemical methods, delivering a deeper understanding of the mechanisms and redox events involved in the catalytic process. Surface attachment may also provide further benefits, such as higher stability, decrease in potentially deleterious bimolecular pathways, and ability to operate in a broader range of solvents.^{8, 11}

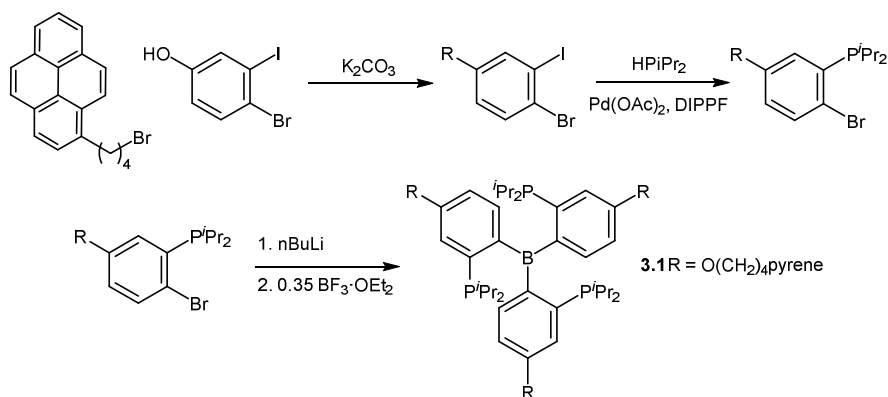
Attachment of a molecular N_2 reduction catalyst to an electrode would demonstrate the compatibility of surface immobilization strategies with conditions required to effect N_2 reduction, as well as allow further study of the immobilized species by electrochemical and spectroscopic methods. Non-covalent attachment between a pyrene-appended

electrocatalyst and a graphitic surface has been applied successfully to the hydrogen evolution reaction (HER), the carbon dioxide reduction reaction (CO₂RR), and the oxygen evolution reaction (OER).¹⁰ This attachment strategy requires modification and new synthetic methods, and often requires multiple pyrene groups to provide long-lived surface-bound species.^{12, 13} Furthermore, it is unclear if this attachment strategy is compatible with the highly reducing potentials required for N₂ reduction. Herein we report the electrochemical production of ammonia by a P₃^BFe complex immobilized on a graphite electrode through three tethered pyrene groups.

3.2 RESULTS AND DISCUSSION

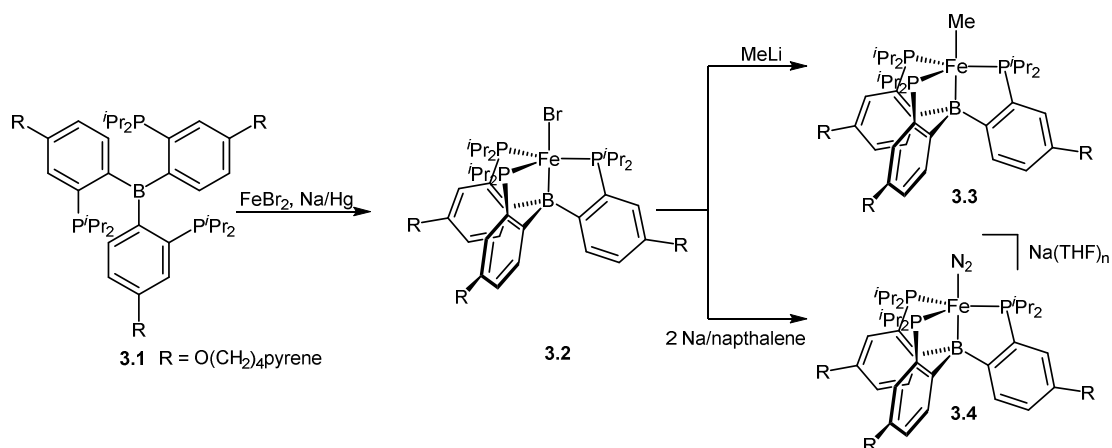
Recently, our group reported the electrocatalytic reduction of N₂ to NH₃ using a cocatalytic electron mediator. Controlled potential electrolysis (CPE) at -2.1 V vs Fc⁺⁰ with a glassy carbon plate electrode using P₃^BFe⁺ as a precatalyst in the presence of [Ph₂NH₂][OTf] acid and [Cp*₂Co][BAR^F₄] gave 5.5 equiv of NH₃ per Fe.^{9c} This catalysis occurs slowly, consuming 100 equiv acid per Fe over the course of ca. 35 hours. To increase the rate of catalysis and limit unproductive bimolecular pathways, we sought to immobilize a P₃^BFe species on a carbon surface.

Scheme 3.1



To immobilize P_3^BFe on a carbon surface, the ligand framework was modified to incorporate three pyrene groups through a butoxy linker (Scheme 3.1). Pyrene groups were attached to the ligand aryl backbone through alkylation of 3-bromo-2-iodophenol with 1-(4-bromobutyl)pyrene followed by cross-coupling with $HPiPr_2$. Lithiation and reaction with $BF_3 \cdot OEt_2$ in toluene/ Et_2O then afforded the desired $^{py}P_3^B$ ligand (**3.1**). Metalation with $FeBr_2$ and reduction with Na/Hg afforded $^{py}P_3^BFeBr$ (**3.2**) as a red solid. Reaction with methyl lithium then gave $^{py}P_3^BFeMe$ (**3.3**), which was purified by extraction with benzene (Scheme 3.2).

Scheme 3.2



Reduction of **3.2** with 2 equiv of $Na/naphthalene$ at $-78^\circ C$ yields $[^{py}P_3^BFeN_2][Na(THF)_n]$ (**3.4**). The IR spectrum of **3.4** shows two intense N_2 stretching

bands at 1930 cm^{-1} and 1880 cm^{-1} , which are attributable to the free anion ${}^{\text{py}}\text{P}_3{}^{\text{B}}\text{FeN}_2^-$ and tight ion pair ${}^{\text{py}}\text{P}_3{}^{\text{B}}\text{FeN}_2\cdots\text{Na}$, respectively.¹⁴ Cyclic voltammetry of **3.4** on a glassy carbon electrode shows a reversible oxidation event at -2.2 V vs $\text{Fc}^{+/0}$ in $0.1\text{ M NaBar}^{\text{F}_4}/\text{Et}_2\text{O}$, compared to -2.1 V vs $\text{Fc}^{+/0}$ for the parent $\text{P}_3{}^{\text{B}}\text{FeN}_2^{0/-}$ couple.^{9c}

We next investigated the N_2 fixation ability of ${}^{\text{py}}\text{P}_3{}^{\text{B}}\text{FeMe}$. We hypothesized that ${}^{\text{py}}\text{P}_3{}^{\text{B}}\text{FeMe}$ would serve as a suitable complex for surface attachment due to its high stability relative to $[{}^{\text{py}}\text{P}_3{}^{\text{B}}\text{FeN}_2][\text{Na}(\text{THF})_n]$, and therefore sought to probe its chemical reactivity to determine if it could serve as a suitable precatalyst for N_2 reduction. Reaction of ${}^{\text{py}}\text{P}_3{}^{\text{B}}\text{FeMe}$ with 108 equiv $[\text{Ph}_2\text{NH}_2][\text{OTf}]$ acid and 54 equiv Cp^*Co reductant at -78°C in Et_2O gave 6.5 equiv NH_3 per Fe, demonstrating the viability of ${}^{\text{py}}\text{P}_3{}^{\text{B}}\text{FeMe}$ as a precatalyst for the reduction of N_2 to NH_3 .

To study the electrochemistry and stability of ${}^{\text{py}}\text{P}_3{}^{\text{B}}\text{FeMe}$ immobilized on a surface, functionalized electrodes were prepared. The precatalyst was immobilized on the surface by soaking rectangular plates ($10\text{ mm} \times 15\text{ mm} \times 1\text{ mm}$) of basal plane highly ordered pyrolytic graphite (HOPG) electrodes in a 1 mM THF solution of ${}^{\text{py}}\text{P}_3{}^{\text{B}}\text{FeMe}$ for 16 hours, followed by rinsing with THF to remove any loosely bound species. The stability of ${}^{\text{py}}\text{P}_3{}^{\text{B}}\text{FeMe}$ to surface attachment was probed by analysis upon desorption by soaking in THF solution (Figure 3.1). UV-visible spectroscopy of **3.3** recovered from a functionalized electrode matched that of an authentic sample, demonstrating that **3.3** is appended to an electrode without decomposition. In total, 27 nmol cm^{-2} of **3** was recovered.

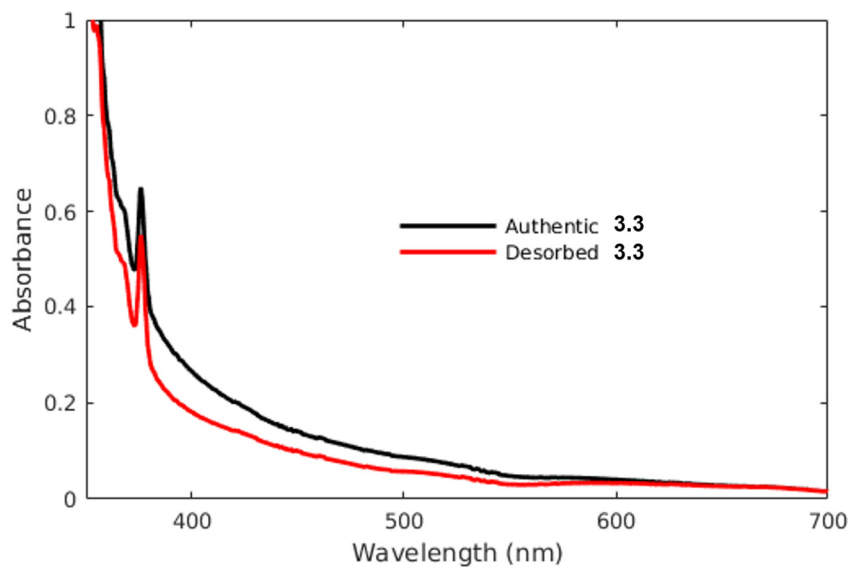


Figure 3.1: UV-vis spectra of authentic sample of **3.3** (black) and sample of **3.3** recovered from functionalized electrode (red).

Cyclic voltammetry of **3.3** immobilized on an HOPG electrode shows an irreversible reduction feature with an onset of -2.1 V vs $\text{Fc}^{+/0}$ (Figure 3.2). Upon addition of $[\text{Ph}_2\text{NH}_2][\text{OTf}]$ at -35 °C, current enhancement is observed with an onset of -1.8 V vs $\text{Fc}^{+/0}$, consistent with current enhancement previously observed with $\text{P}_3^{\text{B}}\text{Fe}^+$ in the presence of acid.^{9c}

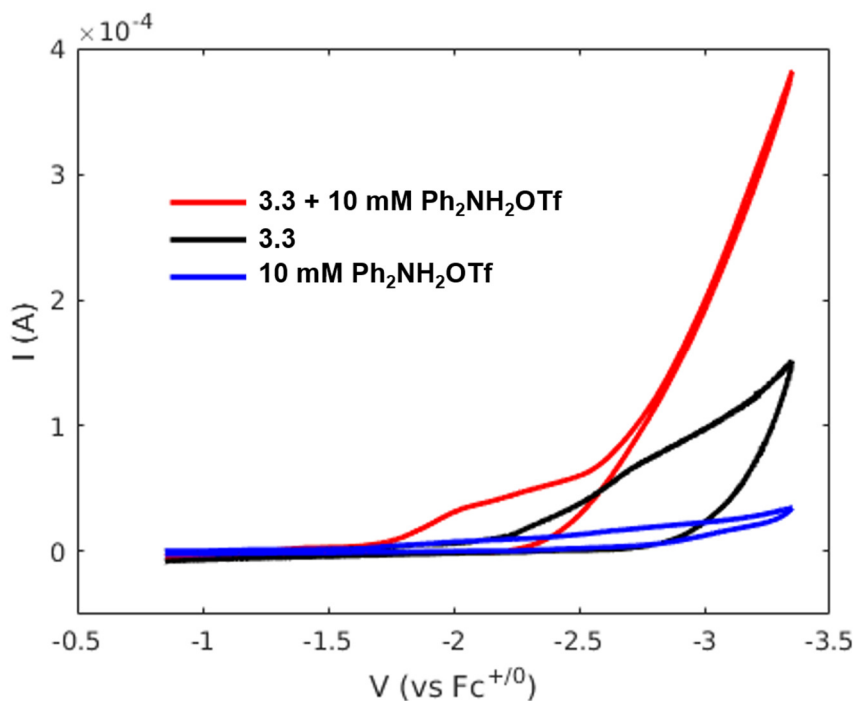
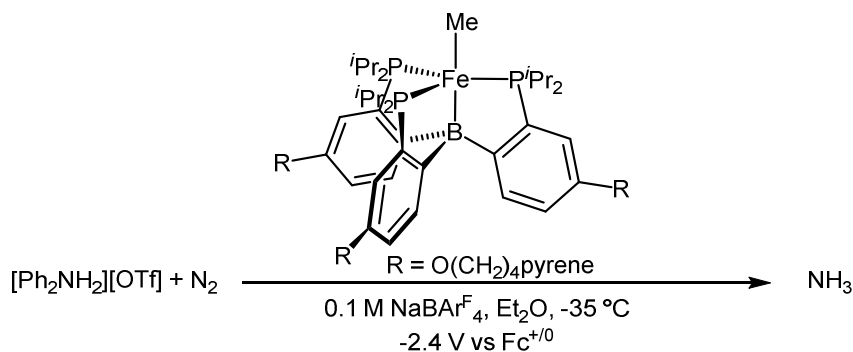


Figure 3.2: Cyclic voltammograms of unfunctionalized electrode in the presence of 10 mM $[\text{Ph}_2\text{NH}_2][\text{OTf}]$ acid (blue trace), electrode functionalized with **3.3** in the absence of acid (black trace), and electrode functionalized with **3.3** in the presence of 10 mM $[\text{Ph}_2\text{NH}_2][\text{OTf}]$ acid (red trace). All voltammograms are collected with a scan rate of 50 mV/s in 0.1 M $\text{NaBAR}_4^{\text{F}_4}$ solution in Et_2O at -35°C and externally referenced to the $\text{Fc}^{+/0}$ couple.

To determine the product profile upon reduction, CPE experiments were conducted in the presence of 100 μmol $[\text{Ph}_2\text{NH}_2][\text{OTf}]$ (Table 3.1). Over a 6 h period at -2.4 V vs $\text{Fc}^{+/0}$, 9.6 C net charge was passed, consistent with nearly full consumption of acid. 1.4 equiv NH_3 were produced per Fe, as determined by the indophenol method. Over the course of the 6 h electrolysis, the current remained above background but decreased at a rate of roughly 10% per hour, likely due to a combination of acid consumption and desorption of the catalyst from the electrode. XPS measurements on electrodes post-electrolysis shows

decreased signals for Fe and P after 6 hours, consistent with partial desorption of ${}^{\text{py}}\text{P}_3{}^{\text{B}}\text{Fe}$ (Figure 3.3).

Table 3.1: Yields of NH_3 from CPE experiments with ${}^{\text{py}}\text{P}_3{}^{\text{B}}\text{FeMe}$ -functionalized electrodes.



entry	hours	charge passed (C)	equiv (per Fe)	Faradaic Efficiency (H_2)
1	6.0	9.6(3) ^a	1.4(1)	89(2)
2 ^b	6.0	0.7	<0.2 ^c	92
3 ^d	6.0	2.7	<0.2 ^c	90

^aAverage of two runs ^bBare HOPG electrode. ^cRelative to Fe loading in entry 1. ^dHOPG electrode functionalized with ligand **3.1**.

To demonstrate that ${}^{\text{py}}\text{P}_3{}^{\text{B}}\text{FeMe}$ is required for NH_3 production, a CPE experiment was conducted employing a non-functionalized electrode. This electrolysis gave <0.2 equiv NH_3 over 6 h, with a net charge of 0.7 C passed. To then demonstrate that Fe is required for NH_3 production, electrodes were functionalized with ${}^{\text{py}}\text{P}_3{}^{\text{B}}$ and employed in CPE experiments. Over 6 h, <0.2 equiv NH_3 was produced, with a net charge of 2.7 C passed. This increased current relative to a bare electrode may be due to protonation of the surface-

bound pyP_3^{B} , which would increase the acid concentration at the electrode and facilitate proton reduction.

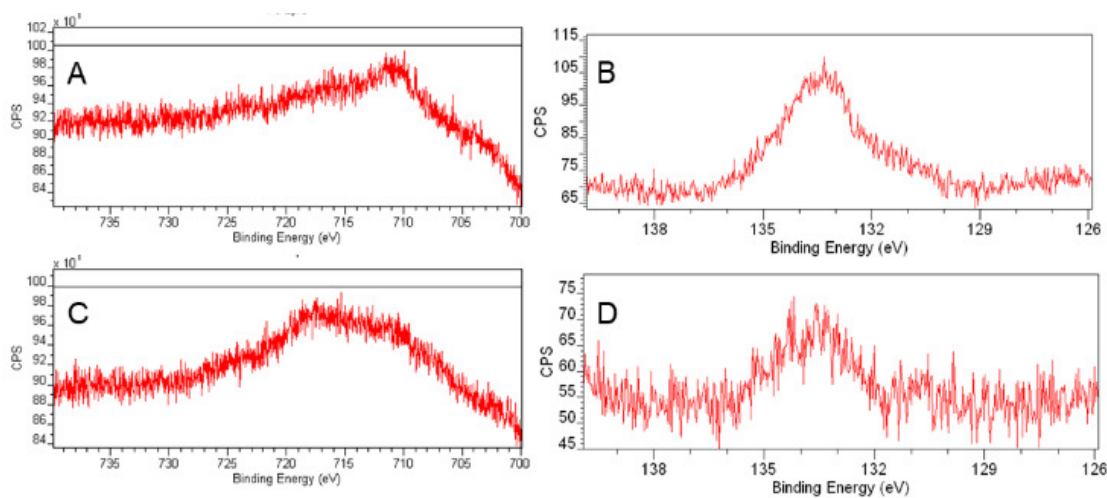


Figure 3.3: XPS spectra of an HOPG electrode with immobilized **3.3** (A) in the Fe 2p region pre-electrolysis, (B) in the P 2p region pre-electrolysis, (C) in the Fe 2p region post-electrolysis, and (D) in the P 2p region post-electrolysis.

3.3 CONCLUSION

In summary, we have demonstrated electrochemical production of NH_3 from a $\text{pyP}_3^{\text{B}}\text{FeMe}$ species immobilized on a graphite surface. To our knowledge, this is the first report of surface attachment of a molecular N_2 reduction catalyst. The functionalized electrode displays reasonable stability over the course of 6 h despite the highly reducing potentials required for N_2 reduction. This stability demonstrates that electrode surface attachment strategies are compatible with the highly reducing potentials required for electrochemical N_2 reduction, and will aid in the optimization and study of N_2 reduction by immobilized catalysts.

3.4 REFERENCES

- (1) Smil, V. *Enriching the Earth*; MIT Press: Cambridge, Mass, 2001.
- (2) Galloway, J. N.; Dentener, F. J.; Capone, D. G.; Boyer, E. W.; Howarth, R. W.; Seitzinger, S. P.; Asner, G. P.; Cleveland, C. C.; Green, P. A.; Holland, E. A.; et al. Nitrogen Cycles: Past, Present, and Future. *Biogeochemistry* **2004**, *70* (2), 153–226.
- (3) Fowler, David; Coyle, Mhairi; Skiba, Ute; Sutton, Mark A.; Cape, J. Neil; Reis, Stefan; Sheppard, Lucy J.; Jenkins, Alan; Grizzetti, Bruna; Galloway, James N.; et al. The Global Nitrogen Cycle in the Twenty-First Century. *Philos. Trans. R. Soc. B: Biol. Sci.* **2013**, *368* (1621), 20130164.
- (4) Ham, C. J. M. van der; Koper, M. T. M.; Hettterscheid, D. G. H. Challenges in Reduction of Dinitrogen by Proton and Electron Transfer. *Chem. Soc. Rev.* **2014**, *43* (15), 5183–5191.
- (5) Shipman, M. A.; Symes, M. D. Recent Progress towards the Electrosynthesis of Ammonia from Sustainable Resources. *Catal. Today* **2017**, *286*, 57–68.
- (6) Rosca, V.; Duca, M.; de Groot, M. T.; Koper, M. T. M. Nitrogen Cycle Electrocatalysis. *Chem. Rev.* **2009**, *109* (6), 2209–2244.
- (7) Kyriakou, V.; Garagounis, I.; Vasileiou, E.; Vourros, A.; Stoukides, M. Progress in the Electrochemical Synthesis of Ammonia. *Catal. Today* **2017**, *286*, 2–13.
- (8) Dalle, K. E.; Warnan, J.; Leung, J. J.; Reuillard, B.; Karmel, I. S.; Reisner, E. Electro- and Solar-Driven Fuel Synthesis with First Row Transition Metal Complexes. *Chem. Rev.* **2019**, *119* (4), 2752–2875.
- (9) (a) Roux, Y.; Duboc, C.; Gennari, M. Molecular Catalysts for N₂ Reduction: State of the Art, Mechanism, and Challenges. *ChemPhysChem* **2017**, *18* (19), 2606–

2617. (b) Pickett, C. J.; Talarmin, J. Electrosynthesis of Ammonia. *Nature* **1985**, *317* (6038), 652. (c) Chalkley, M. J.; Del Castillo, T. J.; Matson, B. D.; Peters, J. C. Fe-Mediated Nitrogen Fixation with a Metallocene Mediator: Exploring pKa Effects and Demonstrating Electrocatalysis. *J. Am. Chem. Soc.* **2018**, *140* (19), 6122–6129. (d) Sherbow, T. J.; Thompson, E. J.; Arnold, A.; Sayler, R. I.; Britt, R. D.; Berben, L. A. Electrochemical Reduction of N₂ to NH₃ at Low Potential by a Molecular Aluminum Complex. *Chem. – Eur. J.* **2019**, *25* (2), 454–458. (e) Lindley, B. M.; van Alten, R. S.; Finger, M.; Schendzielorz, F.; Würtele, C.; Miller, A. J. M.; Siewert, I.; Schneider, S. Mechanism of Chemical and Electrochemical N₂ Splitting by a Rhenium Pincer Complex. *J. Am. Chem. Soc.* **2018**, *140* (25), 7922–7935. (f) Becker, J. Y.; Avraham (Tsarfaty), S.; Posin, B. Nitrogen Fixation: Part I. Electrochemical Reduction of Titanium Compounds in the Presence of Catechol and N₂ in MeOH or THF. *J. Electroanal. Chem. Interfacial Electrochem.* **1987**, *230* (1), 143–153. (g) Becker, J. Y.; Posin, B. Nitrogen Fixation: Part II. Nitrogen Reduction by Electrochemically Generated Vanadium(II) Promoted by Various Organic Ligands in Basic Methanol. *J. Electroanal. Chem. Interfacial Electrochem.* **1988**, *250* (2), 385–397.
- (10) (a) Collman J. P.; Denisevich, P.; Konai, Y.; Marrocco, M.; Koval, C.; Anson, F. C. Electrode Catalysis of the Four-Electron Reduction of Oxygen to Water by Dicobalt Face-to-Face Porphyrins. *J. Am. Chem. Soc.* **1980**, *102* (19), 6027–6036. (b) Yao, S. A.; Ruther, R. E.; Zhang, L.; Franking, R. A.; Hamers, R. J.; Berry, J. F. Covalent Attachment of Catalyst Molecules to Conductive Diamond: CO₂ Reduction Using “Smart” Electrodes. *J. Am. Chem. Soc.* **2012**, *134* (38), 15632–

15635. (c) Axet, M. R.; Dechy-Cabaret, O.; Durand, J.; Gouygou, M.; Serp, P. Coordination Chemistry on Carbon Surfaces. *Coord. Chem. Rev.* **2016**, *308*, 236-345.
- (11) Bullock, R. M.; Das, A. K.; Appel, A. M. Surface Immobilization of Molecular Electrocatalysts for Energy Conversion. *Chem. – Eur. J.* **2017**, *23* (32), 7626–7641.
- (12) Mann, J. A.; Rodríguez-López, J.; Abruña, H. D.; Dichtel, W. R. Multivalent Binding Motifs for the Noncovalent Functionalization of Graphene. *J. Am. Chem. Soc.* **2011**, *133* (44), 17614–17617.
- (13) Kohmoto, M.; Ozawa, H.; Yang, L.; Hagio, T.; Matsunaga, M.; Haga, M. Controlling the Adsorption of Ruthenium Complexes on Carbon Surfaces through Noncovalent Bonding with Pyrene Anchors: An Electrochemical Study. *Langmuir* **2016**, *32* (17), 4141–4152.
- (14) Moret, M.-E.; Peters, J. C. Terminal Iron Dinitrogen and Iron Imide Complexes Supported by a Tris(Phosphino)Borane Ligand. *Angew. Chem. Int. Ed.* **2011**, *50* (9), 2063–2067.

SUPPLEMENTARY DATA FOR CHAPTER 2

A.1 General Considerations

A.1.1 Chemicals

Toluene, acetonitrile, and diethyl ether were degassed with nitrogen and dried by passage through activated alumina using a solvent purification system. Acetonitrile used in photophysical studies was purchased from Alfa Aesar (HPLC Grade, 99.9%+), degassed by three freeze-pump-thaw cycles, and passed through activated alumina prior to use. Phenyl halides were stored over 4 Å molecular sieves and passed through activated alumina prior to use. The following compounds were synthesized according to literature procedures: mesitylcopper,¹ 3-methyl-2,3-dihydrobenzofuran,² 1,2-bis(2,6-dimethylphenyl) disulfide,³ 1-(allyloxy)-2-iodobenzene,⁴ 2,6-dimethylphenyl phenyl sulfide,⁵ 2-(allyloxy)benzenediazonium tetrafluoroborate,⁶ [*n*-Bu₄N][B(C₆F₅)₄],⁷ 1-hydroxyl-2,2,6,6-tetramethylpiperidine,⁸ and 1-(but-3-en-1-yloxy)-2-iodobenzene.⁹ All other chemicals were purchased from commercial suppliers.

A.1.2 Infrared, EPR, and UV-Vis Spectroscopy

UV-vis experiments were conducted with sealable 1-cm path length fused quartz cuvettes (Starna Cells) using a Cary 50 UV-vis spectrometer equipped with a UNISOKU Scientific Instruments Coolspek cryostat. X-band EPR measurements were made with a Bruker EMX spectrometer at 77 K. Simulation of EPR data was conducted using EasySpin.¹⁰ IR measurements were recorded on a Bruker ALPHA Diamond ATR.

A.1.3 NMR Spectroscopy

All NMR spectra were obtained at ambient temperature using Varian 400 and 500 MHz spectrometers unless otherwise noted. ^1H NMR chemical shifts (δ) are reported in parts per million (ppm) relative to the proteo solvent impurity (7.26 ppm for CHCl_3 , 1.94 ppm for CD_2HCN). ^{13}C NMR chemical shifts were also reported relative to the solvent peak (77.16 for CDCl_3).

A.1.4 Mass Spectrometry

The ESI-MS experiment for **2.1** was conducted using a Thermo LCQ ion trap mass spectrometer. Mass spectral data for all organic compounds were collected on an Agilent 5973.

A.1.5 Photophysical Methods

Time-resolved luminescence measurements were conducted using a Q-switched Nd:YAG laser (Spectra-Physics Quanta-Ray PRO-Series) with 8 ns pulses (repetition rate of 10 Hz) in the Beckman Institute Laser Resource Center at the California Institute of Technology. The luminescence was dispersed through a monochromator onto a photomultiplier tube (Hamamatsu R928). Samples were stirred continuously. Steady-state emission spectra were recorded on a Jobin Yvon Spec Fluorolog-3-11. Sample excitation was accomplished with a xenon arc lamp and the right angle emission detected with a photomultiplier tube (Hamamatsu R928P). All measurements were conducted with 1-cm path length fused quartz cuvettes (Starna Cells).

A.1.6 Cyclic Voltammetry

Electrochemical experiments were performed in acetonitrile with 0.1 M [*n*-Bu₄N][B(C₆F₅)₄] as the electrolyte in a nitrogen-filled glovebox. A CH 600B potentiostat was used with a glassy carbon working electrode and a platinum wire auxiliary electrode.

The reference electrode was a Ag/AgNO₃ (0.1 mM)/acetonitrile reference electrode (also contained 0.1 M [*n*-Bu₄N][B(C₆F₅)₄]) separated from the solution by a Vycor frit. The reference electrode was externally referenced to ferrocene. All reported potentials were determined against the reference electrode and converted to SCE by adding 380 mV.

A.1.7 Photolytic Reactions

Photolytic reactions were performed using a 100-W Blak-Ray Long Wave Ultraviolet Lamp (Hg), 100-W Blak-Ray B-100Y High Intensity Inspection Lamp (Hg), or a Luzchem LZC-4V photoreactor equipped with LZC-UVA lamps centered around 350 nm. Temperature control was maintained with either an ice water bath, or isopropanol bath cooled by an SP Scientific cryostat. For reactions using mercury lamps, the light source was placed approximately 20 cm above the sample and the reaction mixture was stirred vigorously using a magnetic stir bar. All reactions were performed in VWR 16 x 100 mm borosilicate culture tubes that were capped with septa and electrical tape. Punctures in the septa were sealed with vacuum grease.



Figure A.1: Representative example of reaction setup using a 100-W Hg lamp. Ice is excluded for clarity.

A.1.8 Chromatography

Normal phase column chromatography was performed using Silicycle 230-400 mesh silica gel. Analytical thin layer chromatography was conducted with Merck aluminum-backed TLC plates (silica gel 60 F₂₅₄) and plates were visualized under UV light. Reverse-phase chromatography was performed with a Biotage Isolera Spektra Four system.

A.1.8 Other Characterization Methods

Elemental analysis was performed by Midwest Microlab, LLC. Calibrated GC yields were obtained using an Agilent 6890N gas chromatograph (FID detector) with dodecane as an internal standard.

A.1.9 X-ray Crystallography

XRD studies were carried out at the Beckman Institute Crystallography Facility on a Bruker D8 Venture kappa duo photon 100 CMOS instrument (Mo K α radiation). Structures

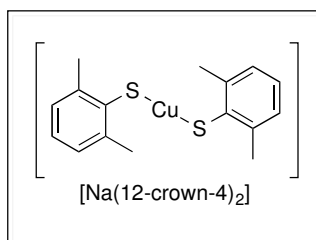
were solved using SHELXT and refined against F^2 by full-matrix least squares with SHELXL and OLEX2. Hydrogen atoms were added at calculated positions and refined using a riding model. The crystals were mounted on a glass fiber or a nylon loop with Paratone N oil.

A.2 Synthesis and Characterization

Reported yields have not been optimized.

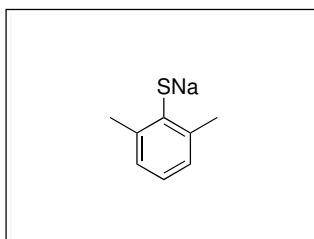
General Procedure A: This procedure is a modification of that developed by Peters, Fu, and co-workers.⁵ In a nitrogen-filled glovebox, electrophile, NaOt-Bu, CuI, and acetonitrile were added to a borosilicate tube. The tube was then capped with a septum and sealed with electrical tape. On a Schlenk line, 2,6-dimethylthiophenol was added *via* syringe. The vessel was then immersed in a cooling bath and irradiated for the specified period. The reaction mixture was then concentrated and the crude material extracted in diethyl ether and filtered through a thin pad of silica. Following concentration, the material was purified by column chromatography.

General Procedure B: The method developed by Venkataraman and coworkers was used for the synthesis of the following compounds.^{10, 11} In a nitrogen-filled glovebox, a borosilicate test tube or round bottom flask was charged with CuI (10 mol%), neocuproine (DMPHEN) or its hemihydrate (10 mol%), aryl iodide (1 equiv.), NaOt-Bu (1.5 equiv.), and toluene. The reaction vessel was removed from the glovebox and connected to a Schlenk line. The reaction mixture was charged with 2,6-dimethylthiophenol (1.1 equiv.) *via* syringe. The reaction mixture was heated at 105 to 110 °C for the specified time, cooled to room temperature, and filtered. The crude material was purified by column chromatography.



Copper(I) bis(2,6-dimethylthiophenolate) sodium bis(12-crown-4) ($[\text{Cu}^{\text{I}}(\text{SAr})_2]\text{Na}$) A Schlenk bomb was charged with NaOt-Bu (90.7 mg, 0.943 mmol), mesitylcopper (181 mg, 0.991 mmol), and acetonitrile (4 mL) in the glovebox. The bomb was

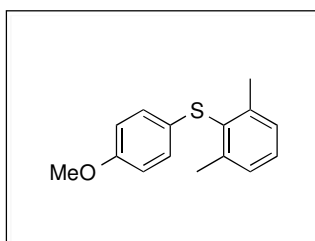
removed from the glovebox and connected to a Schlenk line. 2,6-dimethylthiophenol (250 μL , 1.88 mmol) was added *via* syringe, causing the orange suspension to turn white. The reaction mixture was stirred for 30 min at which time the bomb was returned to the glovebox and its contents filtered through a plug of Celite. 12-crown-4 (162 μL , 1.00 mmol) was added to the filtrate, inducing precipitation of a white solid. The supernatant was removed *via* pipette and the solid washed with diethyl ether. The desired product was isolated as an analytically pure white solid (214 mg, 0.300 mmol, 32% yield) following removal of solvent *in vacuo*. X-ray quality crystals were grown from an acetonitrile solution at ambient temperature over 12 h. ^1H NMR (400 MHz, CD_3CN): δ 6.91 (d, $J = 7.4$ Hz, 4H), 6.70 (t, $J = 7.4$ Hz, 2H), 3.62 (s, 32H), 2.42 (s, 12H). HR-MS (ESI) (m/z) calcd for $[\text{C}_{16}\text{H}_{18}\text{CuS}_2]^-$: 337.0146, found: 337.1133. Calculated for $\text{C}_{32}\text{H}_{50}\text{CuNaO}_8\text{S}_2$: C, 53.88; H, 7.06. Found: C, 53.69, H, 7.14. UV-vis (MeCN): $\lambda_{\text{max}} = 258$ nm, $\epsilon = 2.3 \times 10^4$ $\text{M}^{-1} \text{cm}^{-1}$.



Sodium 2,6-dimethylthiophenolate A Schlenk flask was charged with oil-free sodium hydride (175 mg, 7.29 mmol) and diethyl ether (20 mL) in the glovebox and the vessel sealed with a septum. The reaction mixture was cooled to 0 $^\circ\text{C}$ and 2,6-

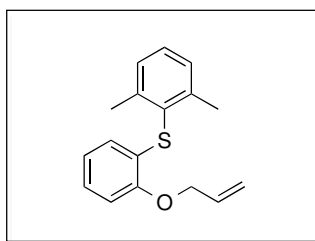
dimethylthiophenol (1.00 mL, 7.51 mmol) delivered to the suspension *via* syringe on a Schlenk line. White precipitate immediately formed. Following stirring for 48 h at ambient

temperature, the solvent was cannulated from the flask and the solid triturated with pentane (*ca.* 100 mL). The desired product was isolated as a spectroscopically pure white solid (1.05 g mg, 6.52 mmol, 89% yield) following removal of solvent *in vacuo*. ^1H NMR (400 MHz, CD_3CN) δ 6.80 (d, $J = 7.3$ Hz, 2H), 6.44 (t, $J = 7.5$ Hz, 1H), 2.30 (s, 6H). UV-vis (MeCN): $\lambda_{\text{max}} = 292$ nm, $\epsilon = 1.9 \times 10^4 \text{ M}^{-1} \text{ cm}^{-1}$.



4-Methoxyphenyl 2,6-dimethylphenyl sulfide According to

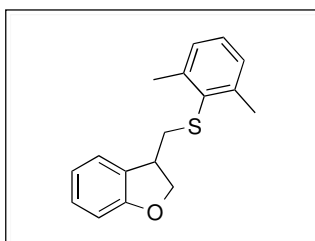
General Procedure B, CuI (42.0 mg, 0.22 mmol), DMPHEN hemihydrate (43.6 mg, 0.20 mmol), 4-iodoanisole (463 mg, 1.98 mmol), 2,6-dimethylthiophenol (280 μL , 2.21 mmol), toluene (6 mL) and NaOt-Bu (293 mg, 3.05 mmol) were heated for 48 h. The product was isolated as a white solid (251 mg, 1.03 mmol, 52% yield) following column chromatography (SiO_2 , 4% EtOAc:hexanes). ^1H NMR (400 MHz, CDCl_3): δ 7.23 – 7.12 (m, 3H), 6.91 (d, $J = 8.7$ Hz, 2H), 6.75 (d, $J = 8.7$ Hz, 2H), 3.75 (s, 3H), 2.43 (s, 6H). ^{13}C NMR (101 MHz, CDCl_3): δ 157.6, 143.6, 132.0, 129.0, 128.7, 128.5, 128.0, 114.8, 55.4, 22.1. LR-MS (EI) (m/z) calculated for $[\text{C}_{15}\text{H}_{19}\text{OS}]^+$: 244.1, found: 244.1. FT-IR (thin film): 3059, 2954, 2832, 1592, 1572, 1490, 1459, 1439, 1283, 1238, 1173, 1032, 820, 769, 638, 625, 536, 507 cm^{-1} .



2-(Allyloxy) 2,6-dimethylphenyl sulfide According to General

Procedure B, CuI (19.3 mg, 0.10 mmol), DMPHEN hemihydrate (22.1 mg, 0.10 mmol), 1-(allyloxy)-2-iodobenzene (251 mg, 0.96 mmol), 2,6-dimethylthiophenol (140 μL , 1.10 mmol), toluene (6 mL) and NaOt-Bu (147 mg, 1.5 mmol) were heated for 14 h. The product was isolated as a white solid (178 mg, 0.658 mmol, 69% yield) by column chromatography (SiO_2 , 4% EtOAc:hexanes). ^1H NMR (400 MHz, CDCl_3) δ 7.30 – 7.14 (m, 3H), 7.07 – 6.97 (m,

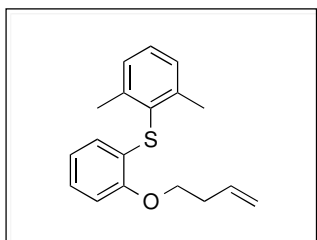
1H), 6.84 (d, $J = 8.1$ Hz, 1H), 6.72 (td, $J = 7.6, 1.2$ Hz, 1H), 6.33 (dd, $J = 7.8, 1.6$ Hz, 1H), 6.11 (ddt, $J = 17.4, 10.3, 5.0$ Hz, 1H), 5.51 (dq, $J = 17.3, 1.7$ Hz, 1H), 5.32 (dq, $J = 10.6, 1.6$ Hz, 1H), 4.67 (dt, $J = 5.1, 1.7$ Hz, 2H), 2.42 (s, 6H). ^{13}C NMR (101 MHz, CDCl_3): δ 154.6, 144.5, 133.3, 129.8, 129.3, 128.6, 127.1, 125.2, 124.9, 121.6, 117.6, 112.1, 69.6, 21.9. LR-MS (EI) (m/z) calculated for $[\text{C}_{17}\text{H}_{18}\text{OS}]^+$: 270.1, found: 270.1. FT-IR (thin film): 3059, 3017, 2955, 2920, 2894, 1575, 1474, 1439, 1233, 1103, 1040, 994, 919, 767, 742 cm^{-1} .



3-(2,6-dimethylphenylthiomethyl)-2,3-dihydrobenzo-furan

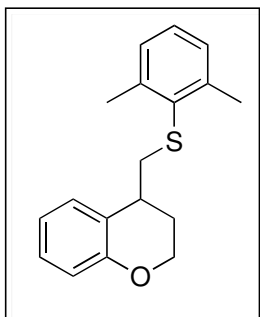
According to General Procedure A, CuI (15.7 mg, 0.082 mmol), NaOt-Bu (76.5 mg, 0.796 mmol), 1-(allyloxy)-2-iodobenzene (208 mg, 0.800 mmol), 2,6-dimethylthiophenol (102 μL , 0.800 mmol), and acetonitrile (2.5 mL) were combined and photolyzed with a mercury lamp for 19 h at -20 $^{\circ}\text{C}$. The reaction mixture was concentrated, and the resulting material suspended in diethyl ether and filtered to remove insoluble byproducts. The product was isolated as a pale yellow oil (96.6 mg, 0.358 mmol, 45% yield) by column chromatography on silica gel (0 \rightarrow 2% EtOAc/hexanes), followed by column chromatography using reverse-phase C-18 silica gel (0 \rightarrow 100% acetonitrile/water). Due to coelution of the title compound and its uncyclized isomer despite multiple attempts at purification, $< 2\%$ of the contaminant is detectable by GC and ^1H NMR analysis. ^1H NMR (400 MHz, CDCl_3): δ 7.19 (d, $J = 7.4$ Hz, 1H), 7.13 (m, 4H), 6.85 (td, $J = 7.4, 1.0$ Hz, 1H), 6.79 (d, $J = 8.0$ Hz, 1H), 4.63 (t, $J = 9.0$ Hz, 1H), 4.45 (dd, $J = 9.1, 5.8$ Hz, 1H), 3.63 – 3.45 (m, 1H), 3.06 (dd, $J = 12.6, 4.6$ Hz, 1H), 2.75 (dd, $J = 12.7, 10.0$ Hz, 1H), 2.56 (s, 6H). ^{13}C NMR (101 MHz, CDCl_3): δ 160.0, 143.0, 133.0, 129.4, 128.9, 128.5, 128.4, 124.5, 120.6, 109.9, 76.3, 42.6, 39.9, 22.2. LR-MS (EI) (m/z) calculated

for $[C_{17}H_{18}OS]^+$: 270.1, found: 270.1. FT-IR (thin film): 3056, 2952, 2923, 2877, 1582, 1488, 1459, 1221, 1023, 772, 753 cm^{-1} .

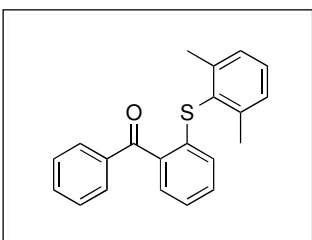


2-(but-3-en-yloxy) 2,6-dimethylphenyl sulfide According to General Procedure B, CuI (20.9 mg, 0.11 mmol), DMPHEN (11.0 mg, 0.0528 mmol), 1-(but-3-en-1-yloxy)-2-iodobenzene (136 mg, 0.990 mmol), 2,6-dimethylthiophenol (140 μ L, 0.496

mmol), toluene (3 mL) and NaOt-Bu (73.2 mg, 0.761 mmol) were heated for 16 h. The product was isolated as a colorless oil (101 mg, 0.354 mmol, 54% yield) following column chromatography (SiO₂, 1 \rightarrow 2% EtOAc/hexanes). ¹H NMR (400 MHz, CDCl₃) δ 7.34 – 7.18 (m, 3H), 7.07 (ddd, J = 8.0, 7.3, 1.6 Hz, 1H), 6.88 (dd, J = 8.1, 1.3 Hz, 1H), 6.75 (td, J = 7.5, 1.2 Hz, 1H), 6.40 (dd, J = 7.7, 1.6 Hz, 1H), 6.04 (ddt, J = 17.0, 10.2, 6.8 Hz, 1H), 5.35 – 5.12 (m, 2H), 4.17 (t, J = 6.8 Hz, 2H), 2.68 (qt, J = 6.8, 1.4 Hz, 2H), 2.47 (s, 6H). ¹³C NMR (101 MHz, CDCl₃) δ 154.9, 144.3, 134.5, 129.9, 129.2, 128.5, 127.0, 125.3, 124.9, 121.4, 117.2, 111.8, 68.3, 33.8, 21.8. LR-MS (EI) (m/z) calculated for $[C_{18}H_{20}OS]^+$: 284.1, found: 284.3. FT-IR (thin film): 3058, 2922, 1576, 1462, 1441, 1237, 1041, 1027, 918, 771, 743 cm^{-1} .



4-(methylchromane) 2,6-dimethylphenyl sulfide According to General Procedure A, CuI (9.0 mg, 0.047 mmol), 1-(allyloxy)-2-iodobenzene (122 mg, 0.445 mmol), 2,6-dimethylthiophenol (66.0 μ L, 0.496 mmol), and NaOt-Bu (47.0 mg, 0.489 mmol) in acetonitrile (5 mL) were photolyzed with 350 nm light in a photobox at ambient temperature for 18 h. The product was isolated as a colorless semi-solid (24.0 mg, 0.084 mmol, 19% yield) by column chromatography on silica gel (0 \rightarrow 2% EtOAc/hexanes), followed by column chromatography using reverse-phase C-18 silica gel (0 to 100% acetonitrile/water). ^1H NMR (400 MHz, CDCl_3): δ 7.14 (ap s, 3H), 7.09 (tdd, $J = 7.3, 1.9, 0.6$ Hz, 2H), 7.02 – 6.94 (m, 1H), 6.88 – 6.73 (m, 1H), 4.30 – 4.20 (m, 1H), 4.20 – 4.09 (m, 1H), 3.12 – 3.04 (m, 1H), 2.96 – 2.87 (m, 1H), 2.88 – 2.79 (m, 1H), 2.59 (d, $J = 0.7$ Hz, 6H), 2.31 – 2.23 (m, 1H), 2.22 – 2.08 (m, 1H). ^{13}C NMR (101 MHz, CDCl_3): δ 154.6, 142.8, 133.6, 129.2, 128.2, 127.8, 124.7, 120.3, 116.9, 62.9, 41.7, 33.9, 26.0, 22.1. LR-MS (EI) (m/z) calculated for $[\text{C}_{18}\text{H}_{20}\text{OS}]^+$: 284.1, found: 284.4. FT-IR (thin film): 3052, 2951, 2919, 1596, 1480, 1459, 1230, 965, 771, 747 cm^{-1} .



2-(2,6-dimethylphenylthio)-benzophenone According to General Procedure B, CuI (20.9 mg, 0.11 mmol), DMPHEN hemihydrate (21.7 mg, 0.10 mmol), 2-iodobenzophenone (305 mg, 0.990 mmol), 2,6-dimethylthiophenol (140 μ L, 1.10 mmol), toluene (6 mL), and NaOt-Bu (143 mg, 1.5 mmol) were heated for 20 h. The product was isolated as a white solid (170 mg, 0.534 mmol, 54% yield) by column chromatography (SiO_2 , hexanes). ^1H NMR (400 MHz, CDCl_3): δ 7.86 (d, $J = 6.8$ Hz, 2H), 7.61 (t, $J = 7.4$ Hz, 1H),

7.54 – 7.46 (m, 2H), 7.44 (d, $J = 7.6$ Hz, 1H), 7.25 – 7.06 (m, 5H), 6.68 (d, $J = 8.0$ Hz, 1H), 2.38 (s, 6H). ^{13}C NMR (101 MHz, CDCl_3): δ 196.7, 144.0, 139.7, 137.7, 136.2, 133.1, 131.3, 131.0, 130.6, 130.3, 129.5, 128.6, 128.5, 126.3, 123.9, 21.9. LR-MS (EI) (m/z) calculated for $[\text{C}_{21}\text{H}_{18}\text{OS}]^+$: 318.1, found: 318.1. FT-IR (thin film): 3057, 2972, 2949, 2919, 1656 (C=O), 1597, 1580, 1462, 1432, 1315, 1284, 1254, 924, 762, 742, 699, 638 cm^{-1} .

A.3 Molar Conductivity Measurements

Conductivity measurements were made using a VWR SB80PC symphony Meter and conductivity probe. The meter was calibrated using aqueous NaCl solutions. All measurements were made using 1 mM solutions of analyte in acetonitrile at 21 °C and corrected to 25 °C using a linear correction of 2.1% per °C.

Table A.1: Molar conductivities of measured compounds.

Compound	Λ_m ($\text{S cm}^2 \text{mol}^{-1}$)
Ferrocene	0.45
[TBA][PF ₆]	168.1
2.1	128.5

A.4 Spectroscopic Identification of Copper(II) Species

Identification by UV-vis. Using propionitrile stock solutions to deliver each reagent, solutions of $[\text{Cu}^{\text{I}}(\text{SAr})_2]\text{Na}$ (4.6 mM, 1 mL, 4.6 μmol), PhI (49 mM, 0.5 mL, 24.5 μmol), and sodium 2,6-dimethylthiophenolate (24 mM, 1 mL, 24.0 μmol) were transferred to a cuvette in a nitrogen-filled glovebox. The reaction mixture was diluted with additional propionitrile (1.5 μM in $[\text{Cu}^{\text{I}}(\text{SAr})_2]\text{Na}$), and the cuvette sealed with a Teflon valve and brought outside of the glovebox. The vessel was cooled to -78 °C and irradiated with a 100-W Hg lamp for 5 min resulting in a blue solution. The cuvette was quickly transferred to the cooled UV-vis cryostat (-80 °C) and the spectrum collected. Control experiments were

prepared identically but with exclusion of one or more components and dilution to a total volume of 3 mL.

Identification by EPR. The model complex $[\text{Cu}^{\text{I}}(\text{SAr})_2]\text{Na}$ (7.0 mg, 0.010 mmol), sodium 2,6-dimethylthiophenolate (8.2 mg, 0.051 mmol), and iodobenzene (0.070 mmol) were diluted in 1:1 propionitrile:butyronitrile (2 mL). An aliquot of the solution was transferred to an EPR tube and sealed. Outside of the glovebox, the tube was irradiated with a 100-W Hg lamp for 5 min at $-78\text{ }^\circ\text{C}$. The sample was immediately transferred to a liquid nitrogen-filled dewar and analyzed by EPR spectroscopy. Control experiments were prepared identically but with exclusion of one or more components.

A.5 Identification of 2.1 by ESI-MS

To a borosilicate tube in a nitrogen-filled glovebox was added, sequentially, CuI (6.3 mg, 0.033 mmol), NaOt-Bu (31.9 mg, 0.33 mmol), iodobenzene (37 μL , 0.33 mmol), and acetonitrile (1 mL). The vessel was fitted with a septum and removed from the glovebox. 2,6-dimethyl thiophenol (44 μL , 0.33 mmol) was added *via* syringe. The heterogeneous reaction mixture was stirred at $0\text{ }^\circ\text{C}$ for 1 h under continuous illumination by a 100-W Hg lamp. An aliquot was drawn *via* a syringe equipped with a filter, and the sample diluted in acetonitrile. Subsequently, the sample was analyzed by ESI-MS.

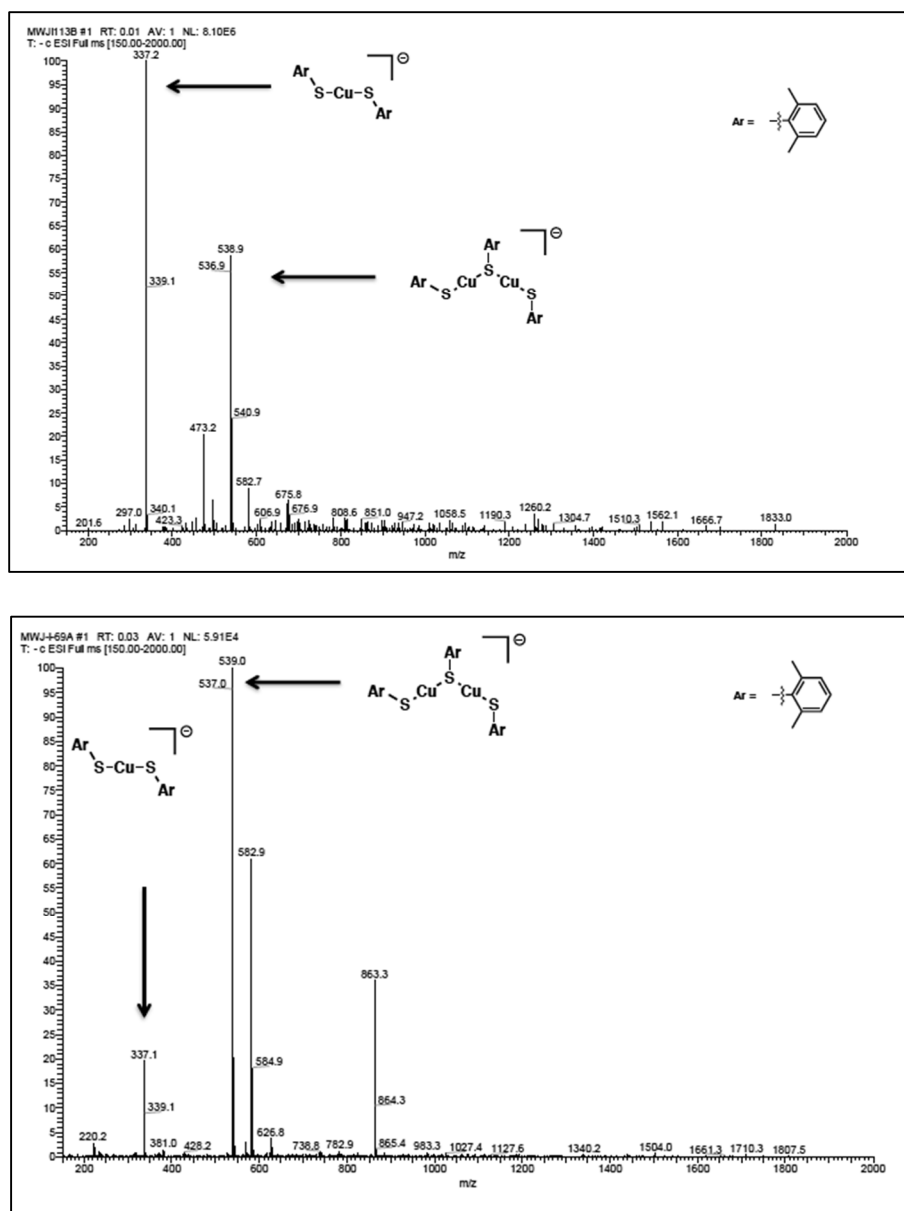


Figure A.2: ESI-MS of **2.1**. Generated during catalysis (top) and independently synthesized (bottom).

A.6 Radical Clock Experiments

All reaction mixtures were analyzed for coupled cyclized product, uncyclized coupled product, starting material, protodehalogenated starting material, and cyclized

protodehalogenated product. Yields were determined by GC with the assistance of dodecane as an internal standard.

Stoichiometric Reaction 2.1 with Radical Clocks. In a nitrogen filled glovebox, a borosilicate test tube was charged with **2.1** (7.1 mg, 0.010 mmol), electrophile (0.010 mmol), and acetonitrile (0.02 M). The reaction mixture was photolyzed for 5 h at which time it was diluted with diethyl ether and dodecane was added (0.010 mmol). The mixture was filtered through silica and analyzed by GC.

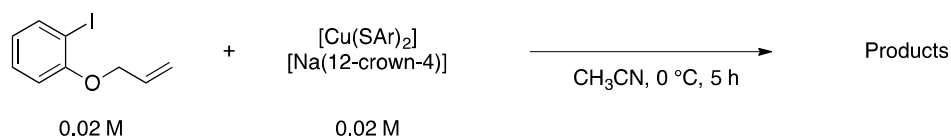


Table A.2: Reactivity of **2.1** with 1-(allyloxy)-2-iodobenzene.

Run 1	2%	50%	0%	4%	38%
Run 2	2%	46%	0%	4%	44%

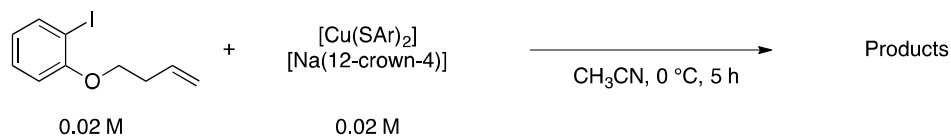
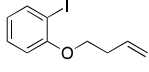
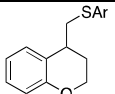
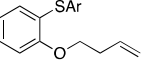
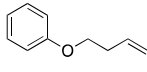
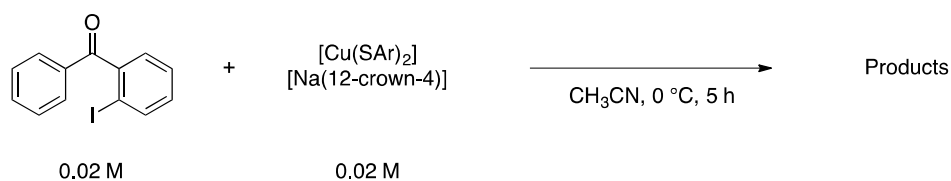
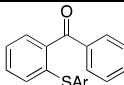
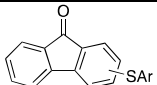
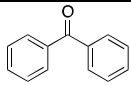
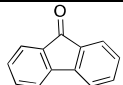
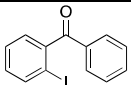


Table A.3: Reactivity of **2.1** with 1-(but-3-en-1-yloxy)-2-iodobenzene.

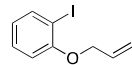
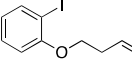
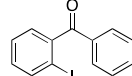
					
Run 1	43%	39%	8%	—	—
Run 2	35%	46%	8%	—	—

**Table A.4:** Reactivity of **2.1** with 2-iodobenzophenone.

					
Run 1	46	0%	8%	0%	11%
Run 2	41	0%	4%	0%	23%

Determination of Radical Clock Stability. All radical clocks were subjected to the same conditions as in the stoichiometric reaction (*vide supra*) but in the absence of $[\text{Cu}^{\text{I}}(\text{SAr})_2]\text{Na}$.

Table A.5: Stability of radical clocks.

Clock	Percent Recovery
	92
	96
	98

A.7 Stoichiometric of $[\text{Cu}^{\text{I}}(\text{SAr})_2]\text{Na}$ with Phenyl Halides

All reaction mixtures were analyzed for product, unreacted phenyl halide, biphenyl, and succinonitrile. Yields were determined by GC with the assistance of dodecane as an internal standard.

Stoichiometric Reaction of 2.1 with Phenyl Halides. In a nitrogen filled glovebox, a borosilicate test tube was charged with **2.1** (7.1 mg, 0.010 mmol), electrophile (0.010 mmol), and acetonitrile (0.02 M). The reaction mixture was photolyzed for 5 h at which time it was diluted with diethyl ether and dodecane was added (0.010 mmol). The mixture was filtered through silica and analyzed by GC.

Table A.6: Reactivity of **2.1** with iodobenzene and control experiments.

	Run 1 (% yeld)	Run 2 (% yield)
PhI	54	57
No light	0	0
No light or catalyst	0	0

A.8 Stern-Volmer Quenching Experiment

Stern-Volmer Kinetic Analysis. Complex **2.1** (30.1 mg, 0.0422 mmol) was diluted in acetonitrile (10 mL, 4.22 mM). Iodobenzene (618 mg, 3.03 mmol) was diluted in acetonitrile (10 mL, 303 mM). An acetonitrile solution of **2.1** (1.2 mM) was prepared with varying amounts of iodobenzene solution. Data were analyzed using Matlab R2015A with the default curve fitting function.

Table A.7: Excited-state lifetime as a function of quencher concentration.

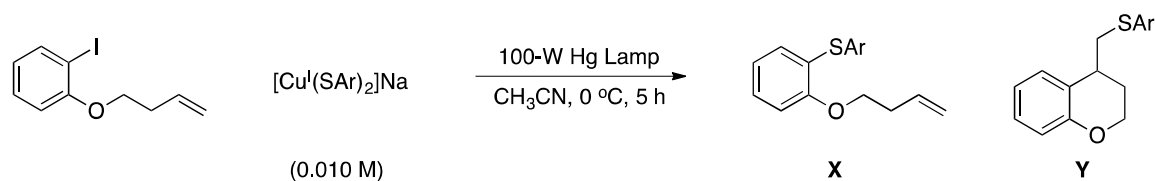
Concentration of PhI (mM)	Lifetime (μs)
0	6.8
43.3	6.0
86.6	4.6
130	4.0
173	3.6

A.9 Steady-State Fluorimetry Experiment

Emission and Excitation of 2.1. A 25 μM solution of **2.1** in acetonitrile was excited using a Xe arc lamp (425 W) at 353 nm and the right angle emission detected at 675 nm. A 470 nm long-pass filter was used in determining both the excitation maximum and minimum.

A.10 Reactivity of 1-(but-3-en-1-yloxy)-2-iodobenzene with $[\text{Cu}^{\text{I}}(\text{SAr})_2]\text{Na}$

A stock solution of 1-(but-3-en-1-yloxy)-2-iodobenzene (1.0 mL, 0.010 M, 0.010 mmol) was added to a borosilicate tube containing $[\text{Cu}^{\text{I}}(\text{SAr})_2]\text{Na}$. The reaction mixtures were photolyzed at 0 $^\circ\text{C}$ for 5 h with a mercury lamp. The reaction mixtures were then passed through a plug of silica diluted with ether, and the product distribution determined by GC.

**Table A.8:** Product distribution in the reaction of **2.1** with 1-(but-3-en-1-yloxy)-2-iodobenzene.

$[\text{Cu}^{\text{I}}(\text{SAr})_2]\text{Na}$ (mmol)	Yield X (%)	Yield Y (%)	Ratio
1.0	6.8	31	4.6
1.5	9.3	39	4.2
2.0	5.9	23	3.9
2.5	9.6	44	4.6

A.11 VT-NMR Study of **2.1**

The ^1H NMR spectrum of **2.1** in CD_3CN (5 mM) was collected at 22 °C (bottom).

The sample was cooled to -30 °C in the probe and an additional spectrum collected.

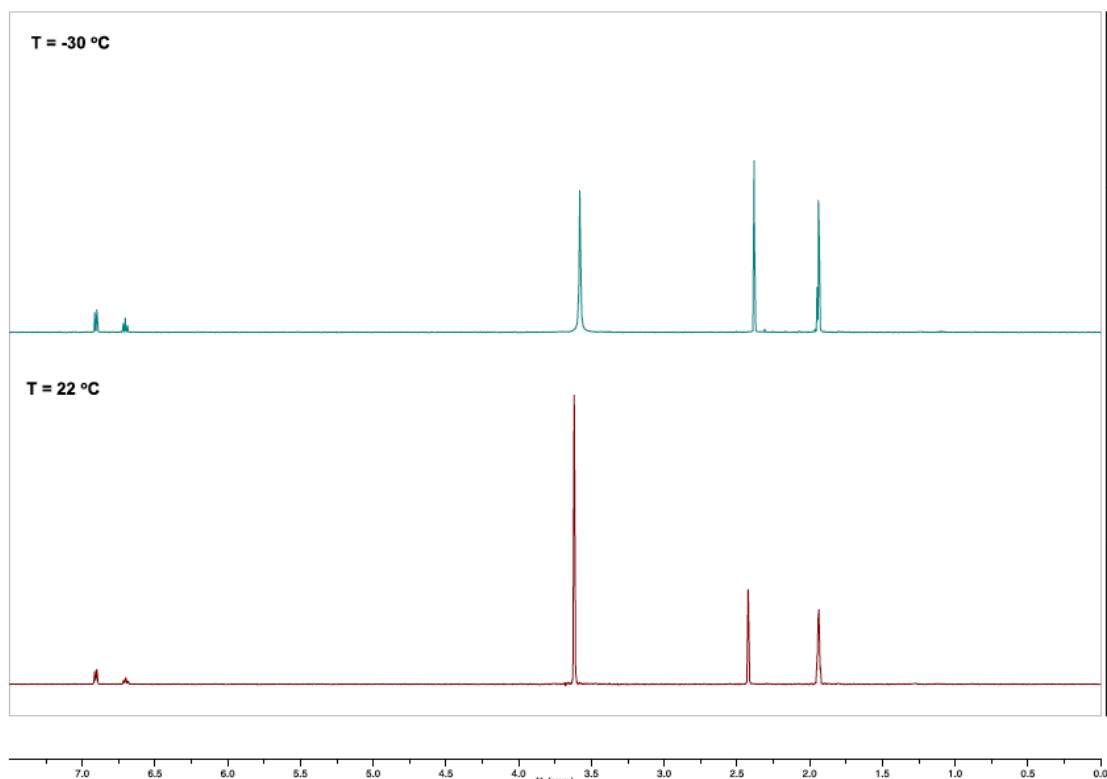


Figure A.3: Low temperature (-30 °C, center) and ambient temperature (22 °C, bottom) ^1H NMR of **2.1**.

A.12 DOSY Experiment

DOSY Procedure. $[\text{Cu}^{\text{I}}(\text{SAr})_2]\text{Na}$ (5 mg, 7 μmol) and decamethylferrocene (0.3 mg, 0.9 μmol) were weighed into an NMR tube, and CD_3CN (0.5 mL) was added. A DOSY spectrum was acquired on a Varian 500 MHz spectrometer with a probe temperature of 25.0 °C, and the diffusion constants were calculated by exponential fit to the individual spectra.

Hydrodynamic radii were calculated from the diffusion constants using the Stokes-Einstein equation.

Table A.9: Measured Hydrodynamic Radii.

δ (ppm)	Assignment	D (10^{-10} m ² /s)	Hydrodynamic Radius (Å)
1.71	Cp* ₂ Fe	17.22(7)	3.70
1.98	CD ₃ CN	39.2(6)	1.62
2.47	[Cu(SAr) ₂] ⁻	14.58(4)	4.19
3.66	[Na(12-crown-4) ₂] ⁺	15.23(6)	4.39

Calculation of Molar Volumes. Molar volumes were calculated from the DFT-optimized geometries. In Gaussian 09, a single point calculation was run using the BP86 functional and def2-TZVP basis set for all atoms. The molar volume was then calculated by Monte-Carlo integration over the electron density grid ('Volume' keyword, 0.001 e-/Bohr³ cutoff density, 1000 test points/Bohr³). All volume calculations were run in triplicate due to the random error associated with Monte-Carlo methods.

Table A.10: DFT-Calculated Radii.

Species	Volume (1 st run, cm ³ /mol)	Volume (2 nd run, cm ³ /mol)	Volume (3 rd run, cm ³ /mol)	Average (cm ³ /mol)	Radius (Å)
[Na(12-crown-4) ₂] ⁺	280.4	286.0	281.6	282.7(23)	4.82
[Cu(SAr) ₂] ⁻	236.9	238.8	242.7	239.5(21)	4.55
[Cu ₂ (SAr) ₃] ⁻	364.2	359.3	361.8	361.8(14)	5.25
[Cu ₂ (SAr) ₄] ²⁻	476.2	461.5	460.6	466.1(30)	5.74
Cp* ₂ Fe	256.1	256.4	255.4	256.0(5)	4.66

A.13 Actinometric Studies

Determination of light intensity. All actinometric experiments were conducted in a Jobin Yvon Spec Fluorolog-3-11 fluorimeter with a 425 W Xe arc lamp using an excitation

wavelength of 365 nm and an excitation slit width of 10 nm. The fluorimeter lamp was allowed to warm up for at least one hour prior to irradiation of samples. The photon flux of the fluorimeter was determined by ferrioxalate actinometry using the method of Bolton,¹² using a quantum yield of 1.28 for ferrioxalate reduction.¹³ Solutions were irradiated for 0, 20, 40, and 60 seconds, and the quantum yield was determined for each sample. A photon flux of $2.9(3) * 10^{-8}$ einsteins s^{-1} was calculated by averaging all time points.

Sample photon flux calculation for 20 second photolysis:

$$\begin{aligned} \text{mol Fe(II)} &= \frac{V * 10 * A}{1000 * \epsilon * V_1} = \frac{3.0 \text{ mL} * 10 * 0.28}{1.0 \text{ mL} * 1000 * 11,100 \text{ L mol}^{-1} \text{ cm}^{-1}} \\ &= 7.5 * 10^{-7} \text{ mol} \end{aligned}$$

$$\text{photon flux} = \frac{\text{mol Fe(II)}}{\text{Phi} * t * f} = \frac{7.5 * 10^{-7}}{1.28 * 20} = 2.9 * 10^{-8} \text{ einsteins s}^{-1}$$

Where V_1 is the volume irradiated, V is the aliquot volume, and ϵ is the extinction coefficient of the Fe(II) phenanthroline complex.

Determination of quantum yield for stoichiometric model reaction. To a 1-cm cuvette with a Kontes valve or screw cap was added $[\text{Cu}^{\text{I}}(\text{SAr})_2]\text{Na}$ (0.06 mmol, 1 equiv), PhI (0.06 mmol, 1 equiv), and MeCN (3.0 mL). A stir bar was added, and the cuvette was sealed. The absorbance of the solution at 365 nm was measured by UV-vis prior to irradiation. The sample was cooled to 0 °C and placed in a cuvette holder cooled to 0 °C with an internal cooling loop. While stirring, the sample was irradiated for one hour. The absorbance of the solution at 365 nm was measured by UV-vis following irradiation. After

irradiation, Et₂O (3 mL) and dodecane (0.06 mmol, 1 equiv) was added. The resulting mixture was passed through a silica plug and was analyzed by GC.

The fraction of light absorbed by the solutions at 365 nm was determined by taking the average between the absorbance prior to irradiation and post irradiation. This was converted to fraction of light absorbed (f), where A is the average absorbance.

$$f = 1 - 10^{-A}$$

The quantum yield of the reaction was then determined using the following equation:

$$\Phi = \frac{\text{mol Fe(II)}}{\text{photon flux} * t * f}$$

The reported quantum yield of 0.08 is the average of two experiments that gave quantum yields of 0.079 and 0.074.

A.14 Emission Spectrum of 100-W Hg Lamp

The emission spectrum was measured using a J & M Analytik TIDAS S 300 K detector.

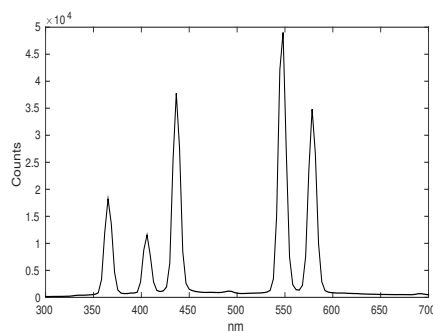


Figure A.4: Emission spectrum of 100-W Blak-Ray Long Wave Ultraviolet Lamp (Hg).

A.14 Determination of Molar Absorptivities (ϵ)

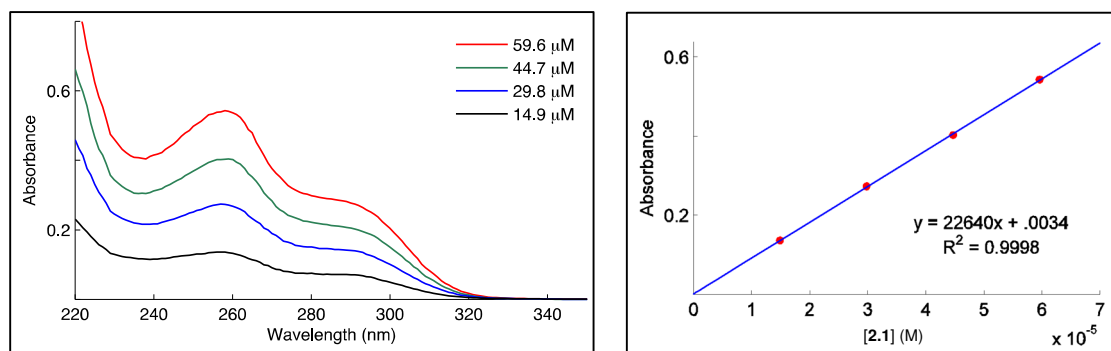


Figure A.5: Absorbance spectra of $[\text{Cu}^{\text{I}}(\text{SAr})_2]\text{Na}$ in acetonitrile at various concentrations (left). Absorbance at 258 nm as a function of concentration (right).

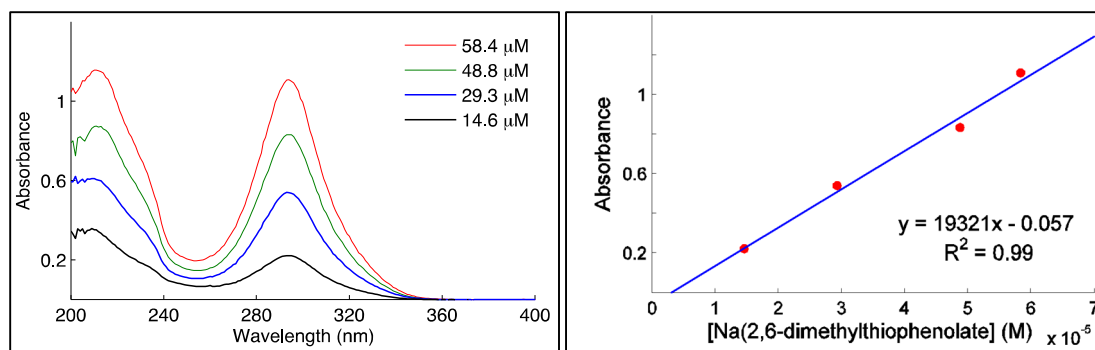


Figure A.6: Absorbance spectra of sodium 2,6-dimethylthiophenolate in acetonitrile at various concentrations (left). Absorbance at 292 nm as a function of concentration (right).

A.15 Absorption Spectra of 2.1 in the Presence of NaSAr

UV-Vis Spectra of [Cu^I(SAr)₂]Na in Varying Concentrations of Sodium 2,6-Dimethylthiophenolate. A propionitrile solution of [Cu^I(SAr)₂]Na (30 μM, 2.5 mL) was added to a septum-sealed cuvette and its spectrum collected. A propionitrile solution of NaSAr (8.1 mM) was added in 20-μL volumes *via* syringe to the cuvette and the spectrum of the resulting solution collected.

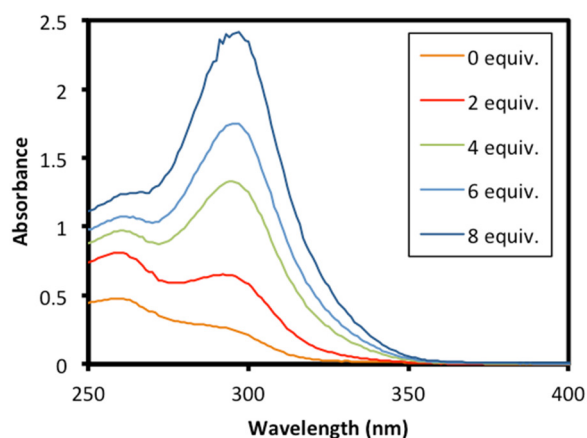


Figure A.7: Optical spectra of 2.1 in the presence of increasing concentrations of sodium 2,6-dimethylthiophenolate.

UV-Vis Spectra of $[\text{Cu}^{\text{I}}(\text{SAr})_2]\text{Na}$ at Various Temperatures in the Presence of Sodium 2,6-Dimethylthiophenolate. A propionitrile solution of $[\text{Cu}^{\text{I}}(\text{SAr})_2]\text{Na}$ ($30 \mu\text{M}$) in the presence of sodium 2,6-dimethylthiophenolate ($80 \mu\text{M}$) was cooled from 25 to $-80 \text{ }^\circ\text{C}$ and the spectrum collected in 20 -degree intervals.

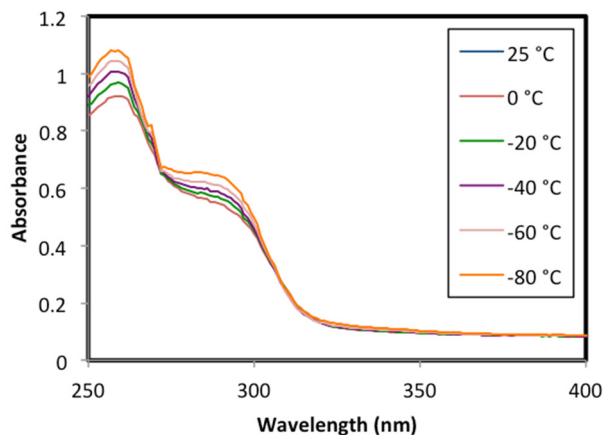


Figure A.8: Optical spectra of **2.1** in the presence of sodium 2,6-dimethylthiophenolate at variable temperature.

A.16 DFT Calculations

General Considerations. The Orca 3.0.1 program was used for all calculations.¹⁴ All optimizations and energy calculations were conducted with tight convergence criteria using the BP86 functional and def2-TZVP basis set,^{15, 16} with the def2-TZVP effective core potential used for iodine.¹⁷ Open and closed shell species were modeled within the unrestricted and restricted Kohn-Sham formalisms, respectively. When energies were compared between open- and closed-shell species, the unrestricted Kohn-Sham formalism was used for all species. All geometry optimizations were conducted without symmetry constraints using gradient methods. Ground state geometries were verified as true minima by the absence of imaginary frequencies. All energies reported are Gibbs free energies at 298.15

K which include translational, rotational, vibrational, and solvation energy contributions. Solvation was treated with the conductor-like screening model, using default parameters for acetonitrile in all cases.

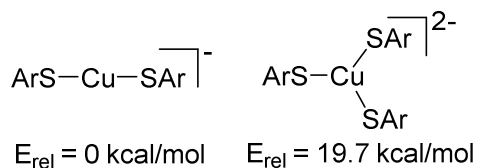


Figure A.9: Calculated free energies of two possible Cu(I) speciations.

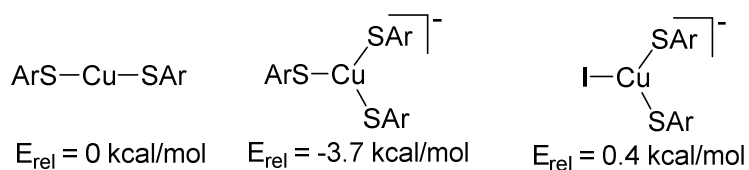


Figure A.10: Calculated free energies of three possible Cu(II) speciations.

Table A.11: Free energies of computed molecules.

Compound	Gibbs Free Energy (Hartrees)
[2,6-dimethylthiophenolate] ⁻	-708.6642
[Cu(2,6-dimethylthiophenolate) ₂] ⁻	-3058.0630
[Cu(2,6-dimethylthiophenolate) ₃] ²⁻	-3766.6958
Cu(2,6-dimethylthiophenolate) ₂	-3057.8949
[Cu(2,6-dimethylthiophenolate) ₃] ⁻	-3766.5650
[Cu(2,6-dimethylthiophenolate) ₂ I] ⁻	3355.9502
I ⁻	-298.0560

EPR Parameter Simulation. DFT calculations of the EPR parameters were conducted using the BP86 functional, the CP(PPP) basis set¹⁸ for copper, and the def2-TZVP

basis set for all other atoms. Integration was performed over a Lebedev grid with 770 points (Grid7) for copper and 590 points (Grid 6) for all other atoms. TD-DFT calculations were conducted using the Tamm-Dancoff approximation.¹⁹

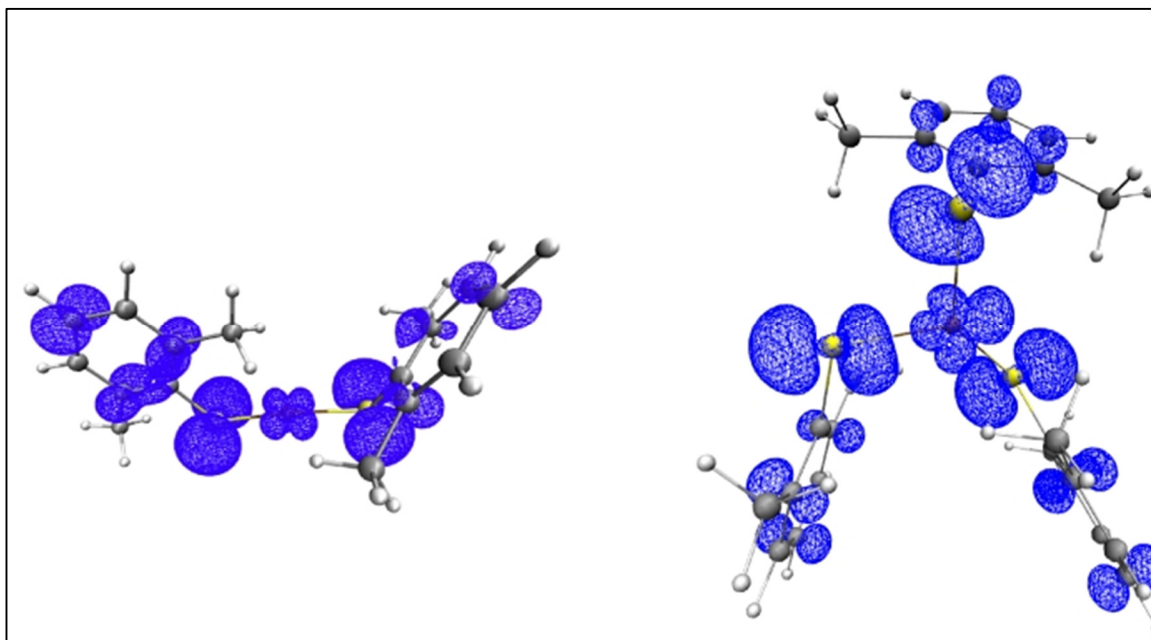


Figure A.11: Spin density plots of $\text{Cu}(\text{2,6-dimethylthiophenolate})_2$ (left) and $[\text{Cu}(\text{2,6-dimethylthiophenolate})_3]^-$ (right).

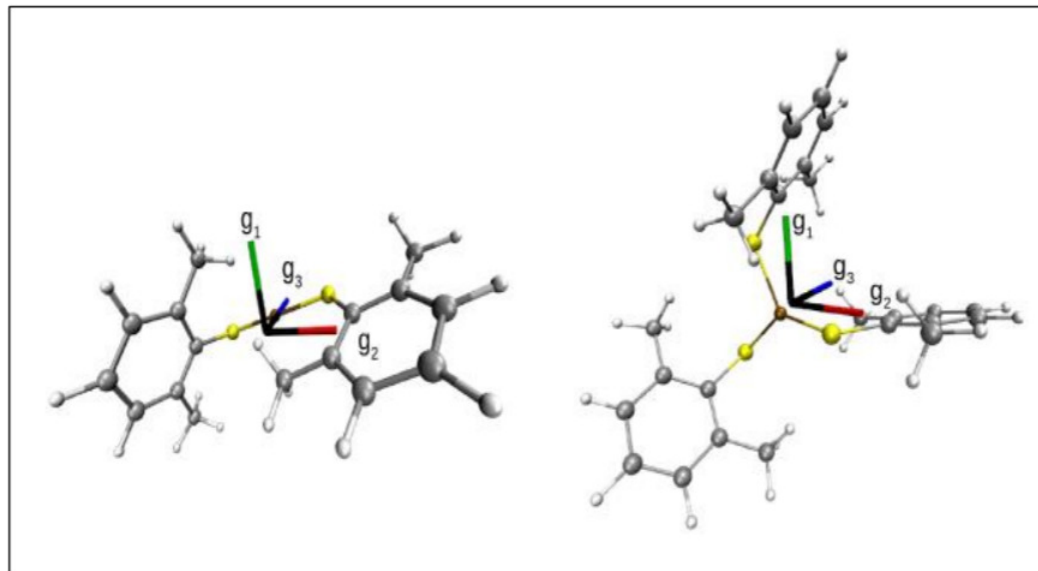


Figure A.12: DFT structures of $\text{Cu}(\text{2,6-dimethylthiophenolate})_2$ (left) and $[\text{Cu}(\text{2,6-dimethylthiophenolate})_3]^-$ (right) showing the orientation of the g tensor.

A.17 Probe of Direct Coupling between $[\text{Cu}^{\text{I}}(\text{SAr})_2]\text{Na}$ (**2.1**) and Aryl Radical

Monitoring of 2.1 and *p*-anisyl-diazonium tetrafluoroborate (2.2) at $-20\text{ }^\circ\text{C}$. In the glovebox, **2.1** (7.2 mg, 0.010 mmol, 1.0 equiv) and **2.2** (2.2 mg, 0.010 mmol, 1.0 equiv) were weighed into a J. Young NMR tube. The tube was sealed and 1.0 mL CD_3CN was added by vacuum transfer. The tube was thawed to $-20\text{ }^\circ\text{C}$ and mixed by gently stirring for 5 minutes before refreezing. The frozen tube was then transferred to an NMR spectrometer pre-cooled to $-20\text{ }^\circ\text{C}$ and the reaction was monitored by ^1H NMR spectroscopy over 30 minutes, showing minimal (<2%) formation of ArSAr^{I} (**2.3**).

Reaction of 2.1 and 2.2. In the glovebox, **2.1** (7.2 mg, 0.010 mmol, 1.0 equiv) and **2.2** (2.2 mg, 0.010 mmol, 1.0 equiv) were weighed into a 4-mL septum-capped vial with a stir bar and acetonitrile (1.0 mL) was added *via* syringe. The reaction was then stirred for 30 minutes at ambient temperature. After stirring for 30 minutes, dodecane (4.5 μL , 0.020 mmol, 2.0 equiv) and 1 mL diethyl ether were added, and the reaction mixtures were filtered

through a short plug of silica and analyzed by GC. Yield of **2.3** = 57% (average of three experiments).

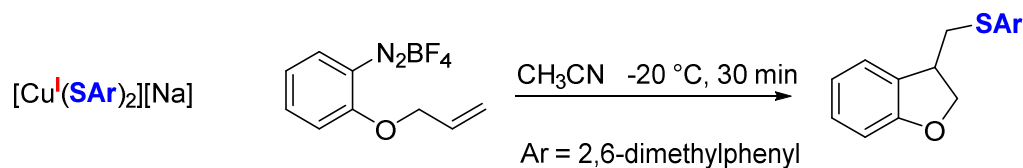
Reaction of 2.1 and 2.2 with Cp*₂Fe. In the glovebox, **2.1** (7.2 mg, 0.010 mmol, 1.0 equiv), **2.2** (2.2 mg, 0.010 mmol, 1.0 equiv), and decamethylferrocene (3.5 mg, 0.011 mmol, 1.1 equiv) were weighed into a 4-mL septum-capped vial with a stir bar. The vial was cooled to -20 °C and acetonitrile (1.0 mL) at -20 °C was added *via* syringe. The reaction was then stirred for 30 minutes at -20 °C and warmed to ambient temperature. After warming for 30 minutes, dodecane (4.5 μL, 0.020 mmol, 2.0 equiv) and 1 mL diethyl ether were added, and the reaction mixtures were filtered through a short plug of silica and analyzed by GC. Yield of **2.3** = 22% (average of two experiments).

Monitoring of 2.1 and 2.2 with Cp*₂Fe at -20 °C. In the glovebox, **2.1** (7.2 mg, 0.010 mmol, 1.0 equiv), **2.6** (2.2 mg, 0.010 mmol, 1.0 equiv), and decamethylferrocene (3.5 mg, 0.011 mmol, 1.1 equiv) were weighed into a J. Young NMR tube. The tube was sealed and 1.0 mL CD₃CN was added by vacuum transfer. The tube was thawed to -20 °C and mixed by gently stirring for 5 minutes before refreezing. The frozen tube was then transferred to an NMR spectrometer pre-cooled to -20 °C. ¹H NMR measurements taken 5 minutes after insertion of the NMR tube into the spectrometer show complete consumption of **2.2**, demonstrating that the reaction between **2.2** and Cp*₂Fe does in fact occur at -20 °C and not upon warming.

Reaction of 2.1 and 2.2 with [Cp*₂Fe][BF₄]. In the glovebox, **2.1** (7.2 mg, 0.010 mmol, 1.0 equiv), **2.2** (2.2 mg, 0.010 mmol, 1.0 equiv), and decamethylferrocenium tetrafluoroborate (4.1 mg, 0.010 mmol, 1.0 equiv) were weighed into a 4-mL septum-capped vial with a stir bar. The vial was cooled to -20 °C and acetonitrile (1.0 mL) at -20 °C was

added *via* syringe. The reaction was then stirred for 30 minutes at $-20\text{ }^{\circ}\text{C}$ and warmed to ambient temperature. After warming for 30 minutes, dodecane ($4.5\text{ }\mu\text{L}$, 0.020 mmol , 2.0 equiv) and 1 mL diethyl ether were added, and the reaction mixtures were filtered through a short plug of silica and analyzed by GC. Yield of **2.3** = 56% (average of two experiments).

Reaction of 2.1 and 2-(allyloxy)benzenediazonium tetrafluoroborate. In the glovebox, **2.1** (7.2 mg, 0.010 mmol , 1.0 equiv) and 2-(allyloxy)benzenediazonium tetrafluoroborate (2.5 mg, 0.010 mmol , 1.0 equiv) were weighed into a 4-mL septum-capped vial with a stir bar. The vial was cooled to $-20\text{ }^{\circ}\text{C}$ and acetonitrile (1.0 mL) at $-20\text{ }^{\circ}\text{C}$ was added *via* syringe. The reaction was then stirred for 30 minutes at $-20\text{ }^{\circ}\text{C}$. After stirring for 30 minutes, dodecane ($4.5\text{ }\mu\text{L}$, 0.020 mmol , 2.0 equiv) and 1 mL diethyl ether were added, and the reaction mixtures were filtered through a short plug of silica and analyzed by GC. Yield of 3-(2,6-dimethylphenylthiomethyl)-2,3-dihydrobenzo-furan = 99% (average of two experiments).



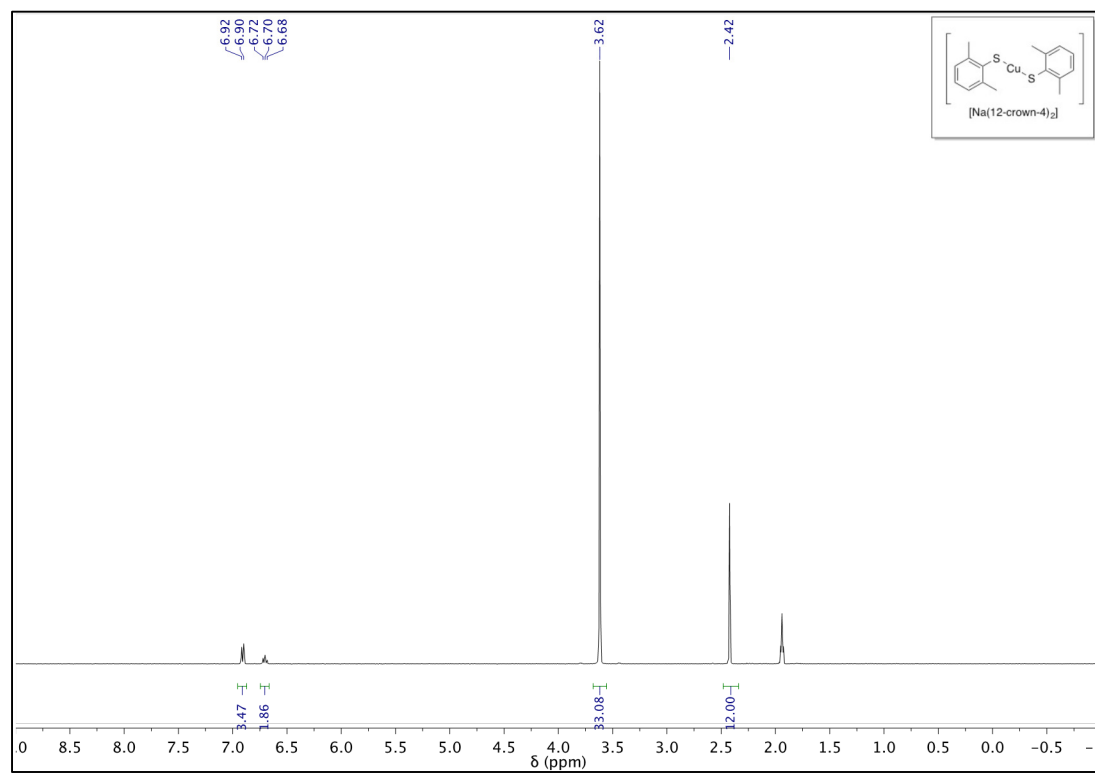
Probe for Redox Equilibrium between 2.1 and $[\text{Cp}^*_2\text{Fe}][\text{BF}_4]$ at $-20\text{ }^{\circ}\text{C}$. To probe the possibility of a redox equilibrium between **2.1** and $[\text{FeCp}^*_2][\text{BF}_4]$, we reacted **2.1** with $[\text{FeCp}^*_2][\text{BF}_4]$ at $-20\text{ }^{\circ}\text{C}$ in CH_3CN and observed $\sim 20\%$ consumption of $[\text{FeCp}^*_2][\text{BF}_4]$ over 30 minutes, consistent with a redox equilibrium between **2.1** and $[\text{FeCp}^*_2][\text{BF}_4]$ involving a thermally unstable Cu(II)-thiolate. To provide further support for this redox equilibrium, we employed TEMPOH as a trap for any generated Cu(II)-thiolate (TEMPOH = 1-hydroxyl-2,2,6,6-tetramethylpiperidine). Reaction of **2.1** with $[\text{FeCp}^*_2][\text{BF}_4]$ and TEMPOH at $-20\text{ }^{\circ}\text{C}$

in CH₃CN resulted in complete consumption of [FeCp*₂][BF₄] within 10 minutes, consistent with a redox equilibrium between [FeCp*₂]⁺ and **2.1**. This redox equilibrium would lead to a Cu(II)-thiolate, which could then couple with an aryl radical to yield the diarylsulfide.

A.18 X-Ray Crystallographic Data

Table A.12: Crystal Data and Structure Refinement for **2.1**.

Identification Code	2.1
Empirical Formula	$C_{32}H_{50}CuNaO_8S_2$
Formula Weight	713.37
Temperature/K	100
Crystal System	monoclinic
Space Group	$P2_1/c$
$a/\text{\AA}$	10.5883(14)
$b/\text{\AA}$	21.967(2)
$c/\text{\AA}$	14.4286(16)
$\alpha/^\circ$	90
$\beta/^\circ$	95.682(6)
$\gamma/^\circ$	90
Volume/ \AA^3	3339.6(7)
Z	4
ρ_{calc} mg/mm ³	1.419
F(000)	1512
Crystal Size/mm ³	0.16 x 0.15 x 0.09
Radiation	Mo K α ($\lambda = 0.71073$)
2 θ range for data collection	4.6 to 74.0
Indices Ranges	$-17 \leq h \leq 17, -37 \leq k \leq 36, -24 \leq l \leq 24$
Reflections Collected	141854
Independent Reflections	16419 ($R_{\text{int}} = 0.1249$)
Data/Restraints/Parameters	16419/0/401
Goodness-of-fit on F^2	1.036
Final R indices [$I > 2\sigma(I)$]	$R_1 = 0.0673, wR_2 = 0.0931$
Final R Indices [all data]	$R_1 = 0.1542, wR_2 = 0.1114$
Largest diff. Peak/hole / $e\text{\AA}^{-3}$	0.640 / -0.547

A.19 ^1H and ^{13}C NMR Data**Figure A.13:** ^1H NMR of $[\text{Cu}^{\text{I}}(\text{SAr})_2]\text{Na}$.

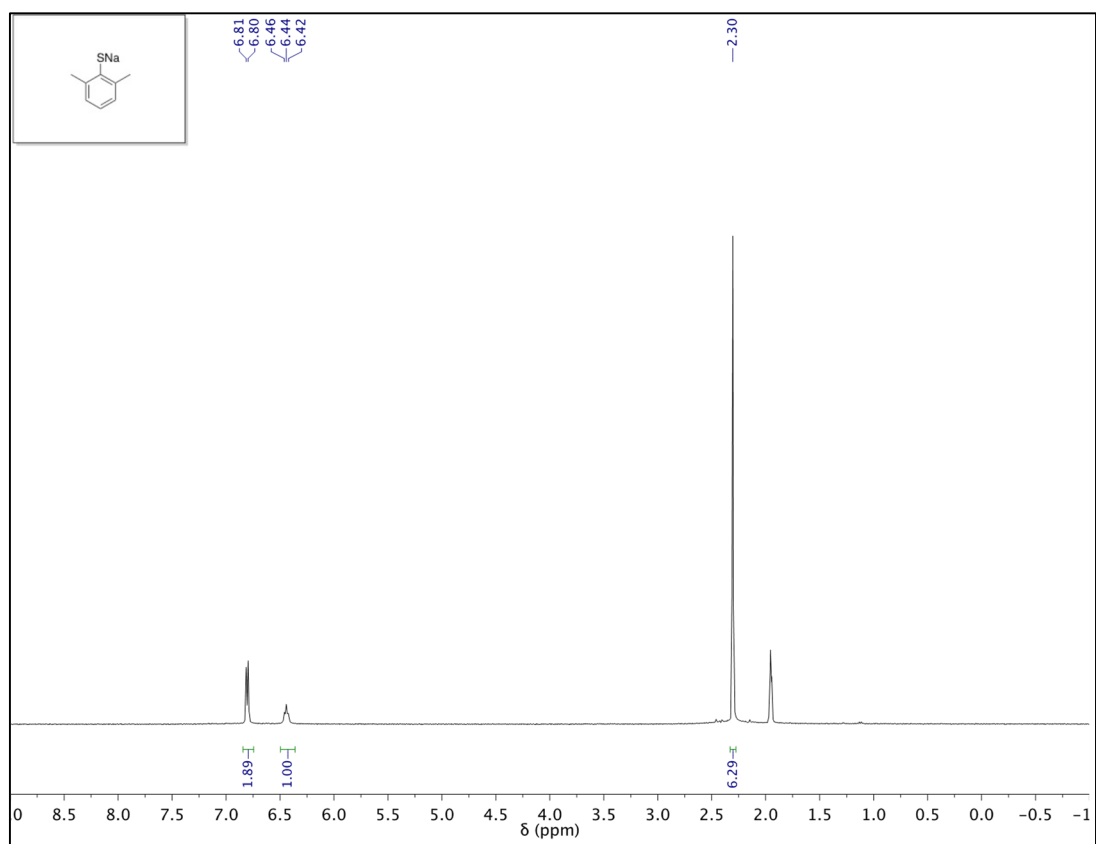


Figure A.14: ^1H NMR of Sodium 2,6-dimethylthiophenolate.

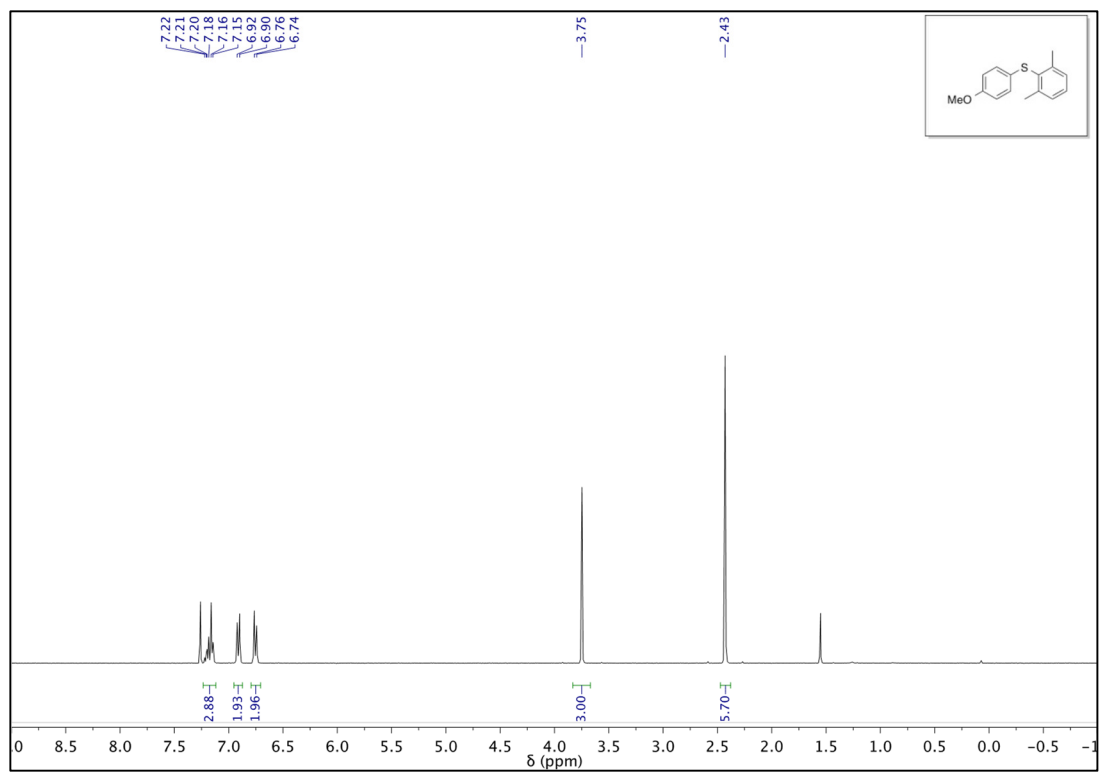


Figure A.15: ^1H NMR of 4-Methoxyphenyl 2,6-dimethylphenyl sulfide.

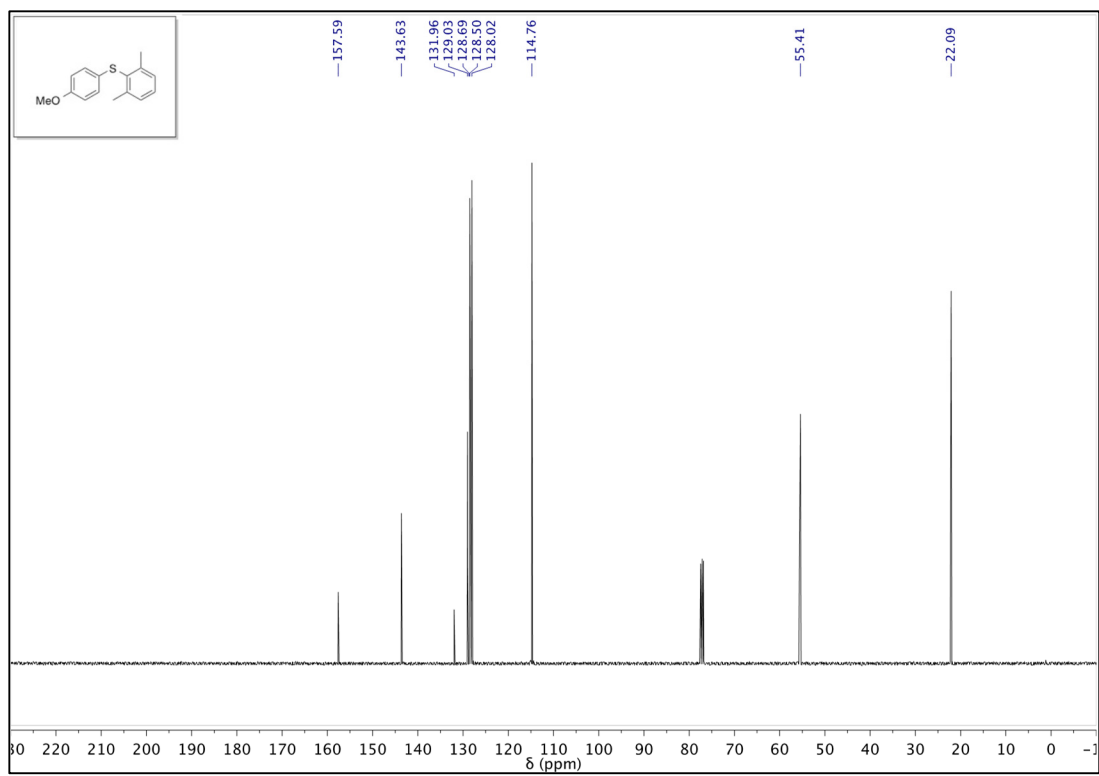


Figure A.16: ^{13}C NMR of 4-Methoxyphenyl 2,6-dimethylphenyl sulfide.

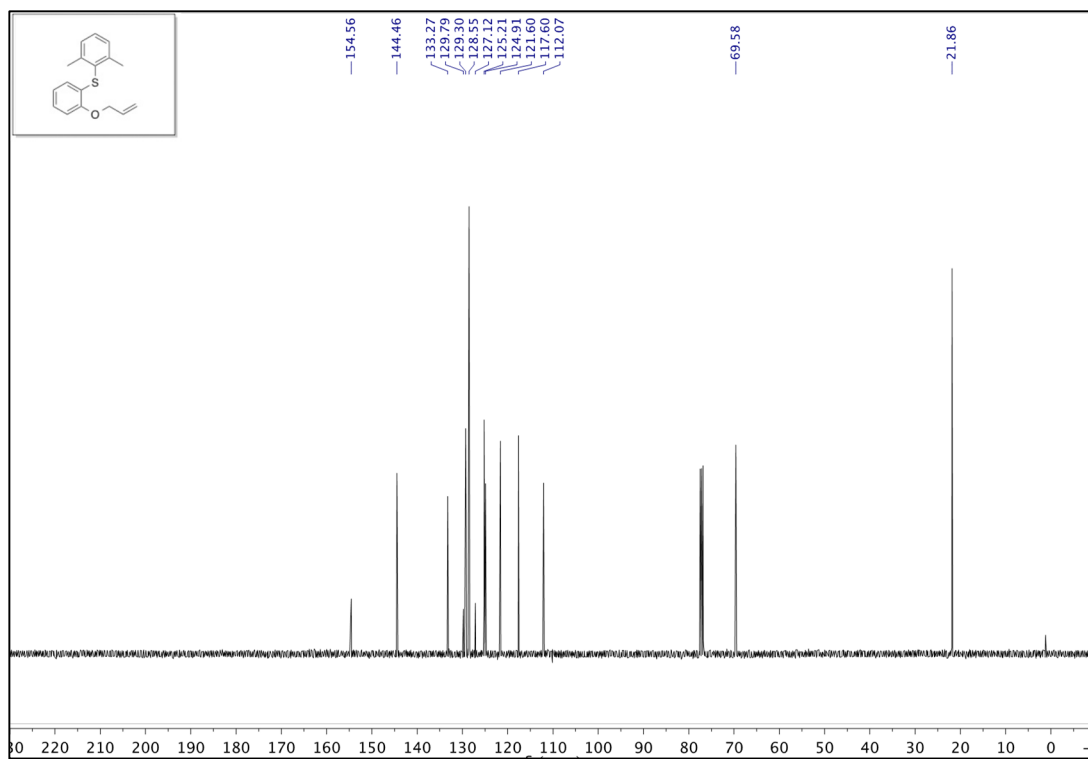


Figure A.18: ^{13}C NMR of 2-(Allyloxy) 2,6-dimethylphenyl sulfide.

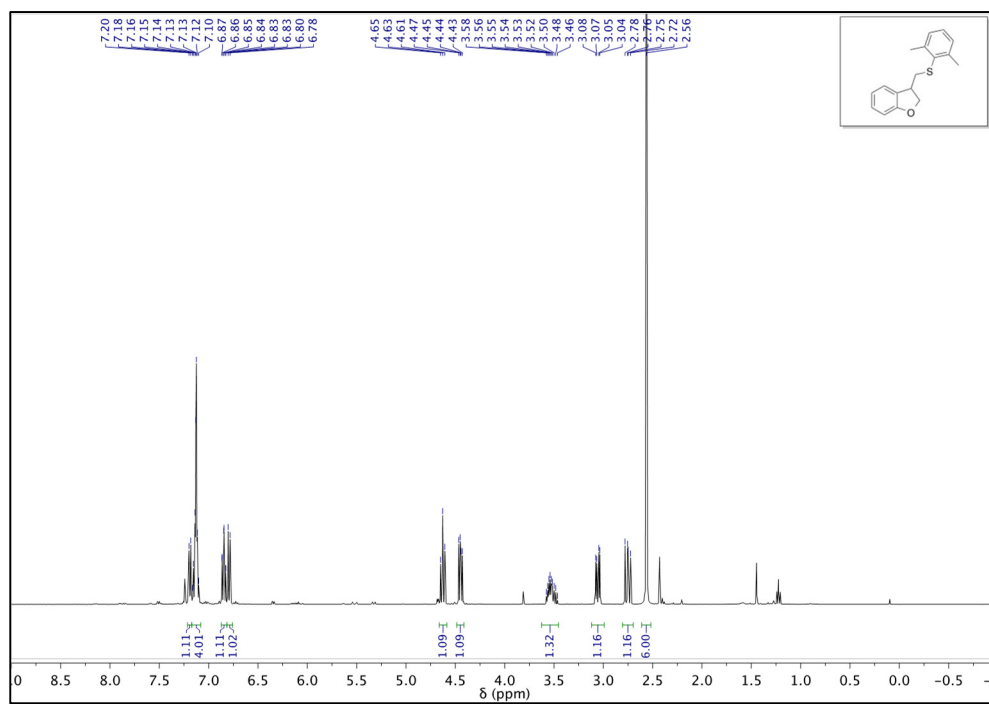


Figure A.19: ¹H NMR of 3-(2,6-dimethylphenylthiomethyl)-2,3-dihydrobenzo-furan.

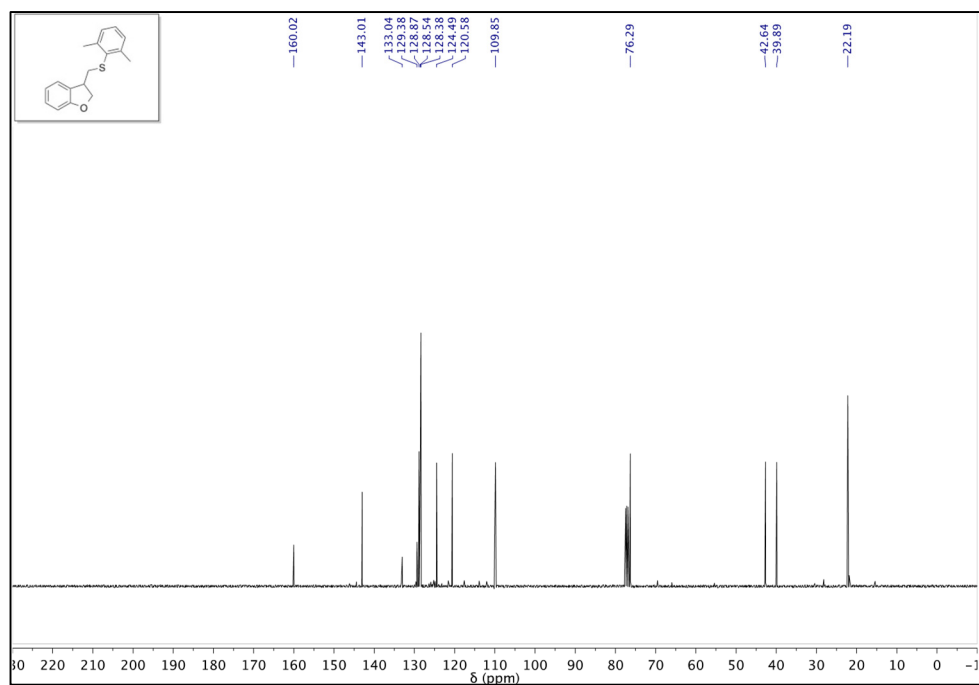


Figure A.20: ^{13}C NMR of 3-(2,6-dimethylphenylthiomethyl)-2,3-dihydrobenzo-furan.

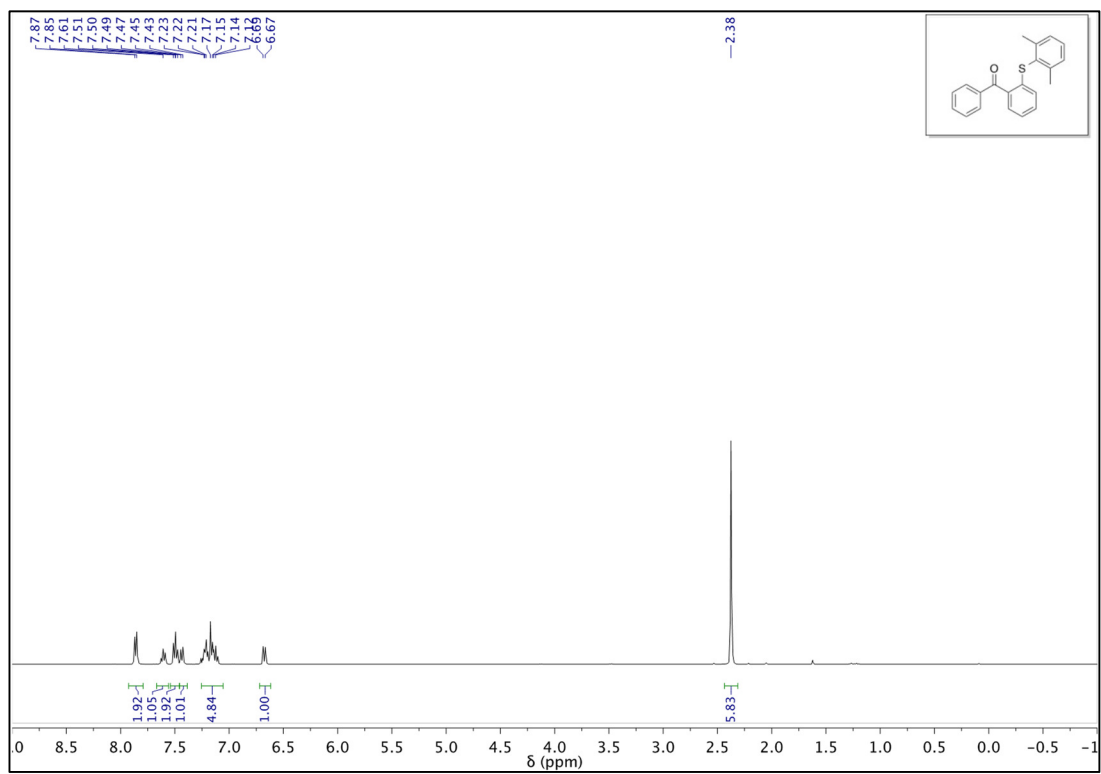


Figure A.21: ^1H NMR of 2-(2,6-dimethylphenylthio)-benzophenone.

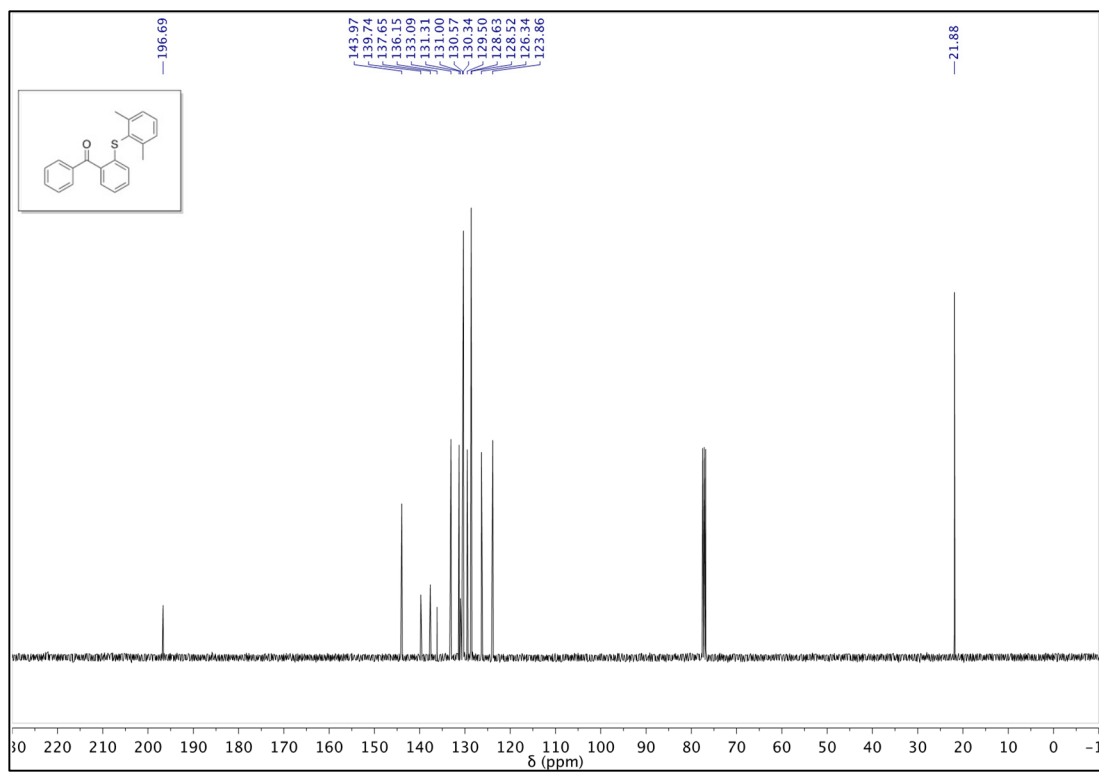


Figure A.22: ^{13}C NMR of 2-(2,6-dimethylphenylthio)-benzophenone.

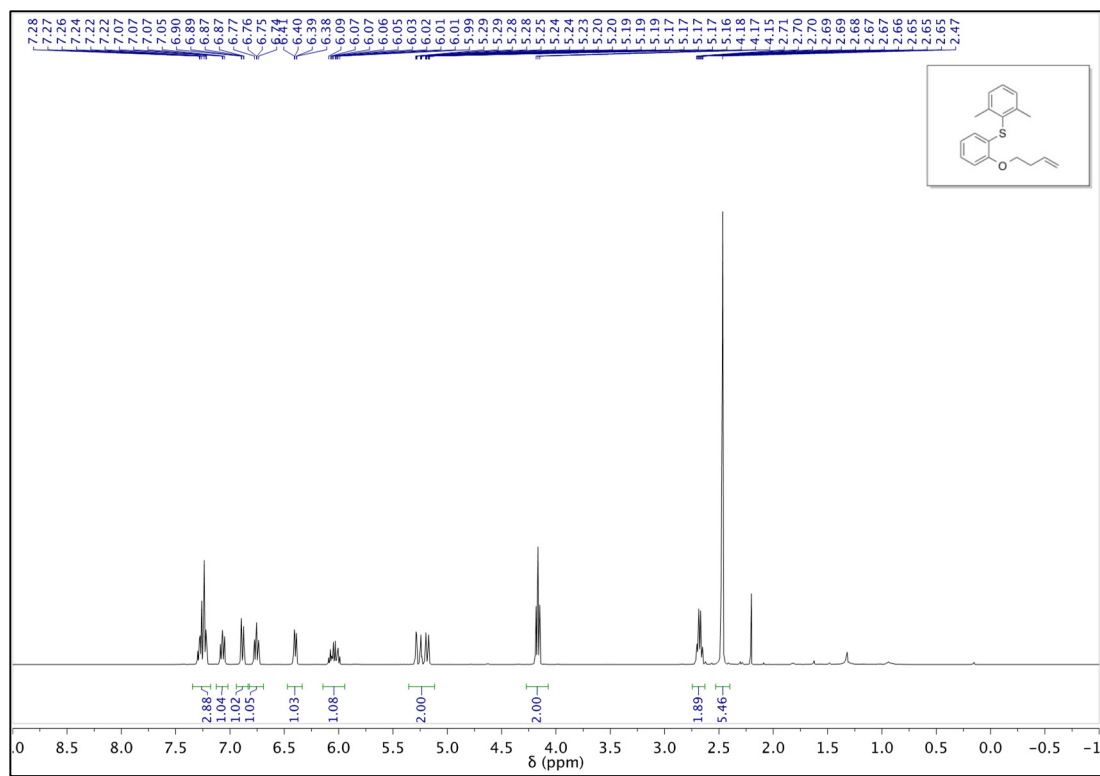


Figure A.23: ¹H NMR of 2-(but-3-en-yloxy) 2,6-dimethylphenyl sulfide.

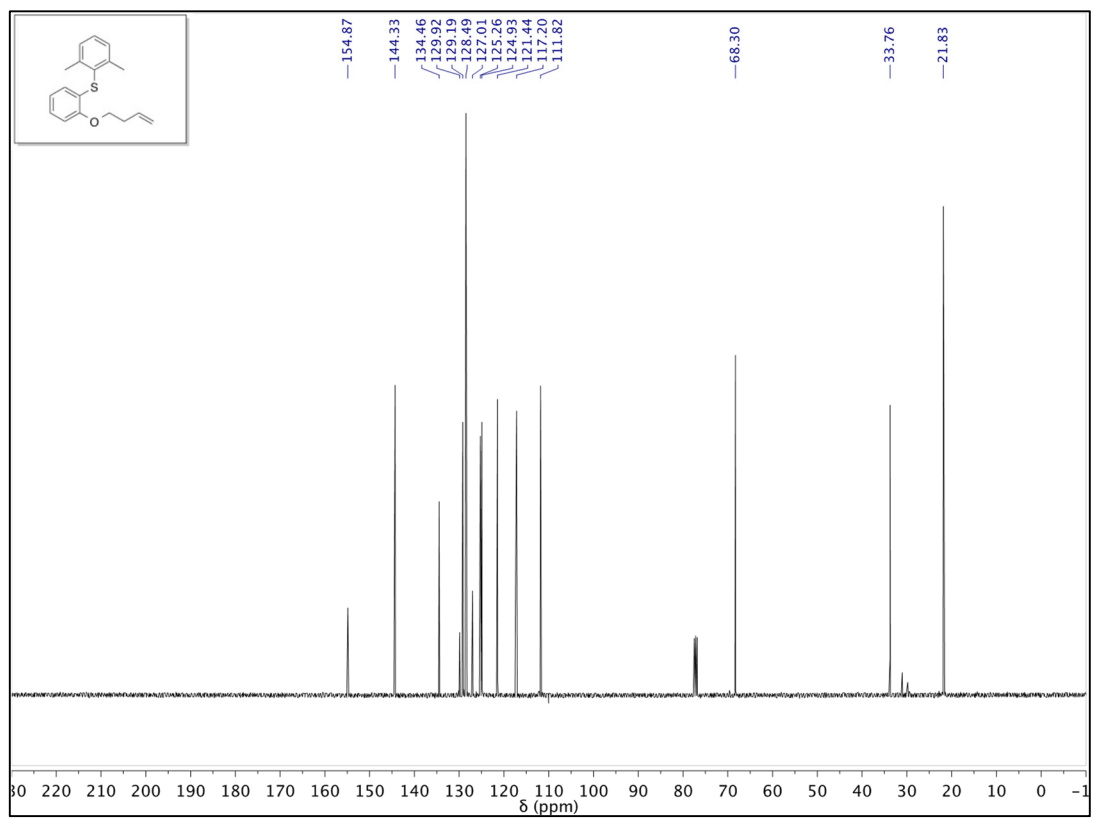
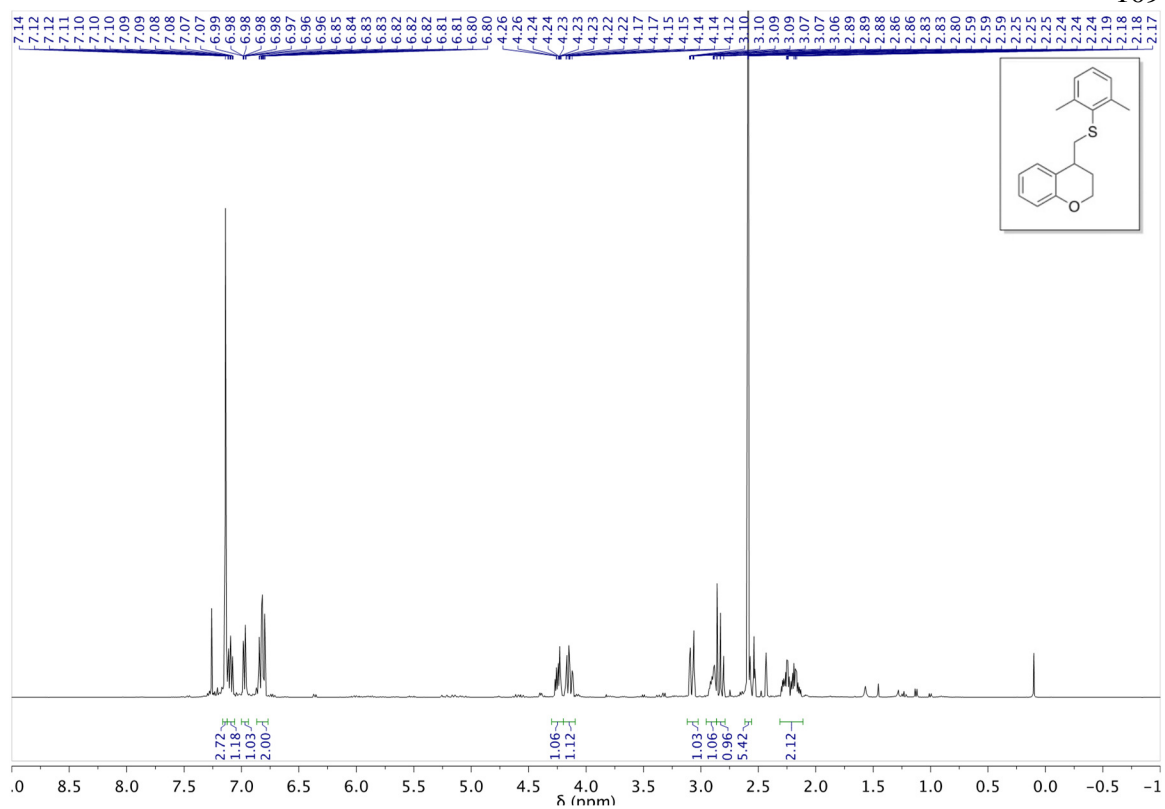


Figure A.24: ^{13}C NMR of 2-(but-3-en-yloxy) 2,6-dimethylphenyl sulfide.



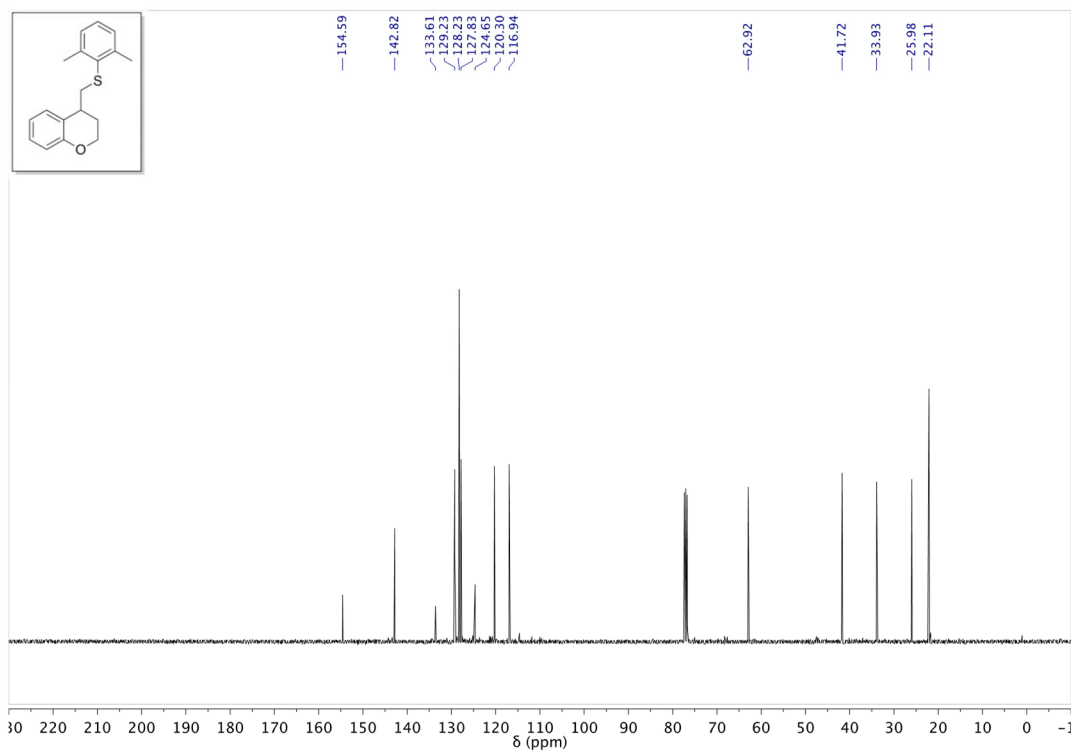


Figure A.26: ¹³C NMR of 4-(methylchromane) 2,6-dimethylphenyl sulfide.

A.20 References

- (1) Tsuda, T.; Yazawa, T.; Watanabe, K.; Fujii, T.; Saegusa, T. Preparation of Thermally Stable and Soluble Mesitylcopper(I) and Its Application in Organic Synthesis. *J. Org. Chem.* **1981**, *46* (1), 192–194.
- (2) Jiang, H.; Bak, J. R.; López-Delgado, F. J.; Jørgensen, K. A. Practical Metal- and Additive-Free Methods for Radical-Mediated Reduction and Cyclization Reactions. *Green Chem.* **2013**, *15* (12), 3355–3359.
- (3) Carril, M.; SanMartin, R.; Domínguez, E.; Tellitu, I. A Highly Advantageous Metal-Free Approach to Diaryl Disulfides in Water. *Green Chem.* **2007**, *9* (4), 315–317.

- (4) Dahlén, A.; Petersson, A.; Hilmersson, G. Diastereoselective Intramolecular SmI₂-H₂O-Amine Mediated Couplings. *Org. Biomol. Chem.* **2003**, *1* (14), 2423–2426.
- (5) Uyeda, C.; Tan, Y.; Fu, G. C.; Peters, J. C. A New Family of Nucleophiles for Photoinduced, Copper-Catalyzed Cross-Couplings via Single-Electron Transfer: Reactions of Thiols with Aryl Halides Under Mild Conditions (0 °C). *J. Am. Chem. Soc.* **2013**, *135* (25), 9548–9552.
- (6) Erb, W.; Hellal, A.; Albin, M.; Rouden, J.; Blanchet, J. An Easy Route to (Hetero)Arylboronic Acids. *Chem. – Eur. J.* **2014**, *20* (22), 6608–6612.
- (7) LeSuer, R. J.; Buttolph, C.; Geiger, W. E. Comparison of the Conductivity Properties of the Tetrabutylammonium Salt of Tetrakis(Pentafluorophenyl)Borate Anion with Those of Traditional Supporting Electrolyte Anions in Nonaqueous Solvents. *Anal. Chem.* **2004**, *76* (21), 6395–6401.
- (8) Giffin, N. A.; Makramalla, M.; Hendsbee, A. D.; Robertson, K. N.; Sherren, C.; Pye, C. C.; Masuda, J. D.; Clyburne, J. A. C. Anhydrous TEMPO-H: Reactions of a Good Hydrogen Atom Donor with Low-Valent Carbon Centres. *Org. Biomol. Chem.* **2011**, *9* (10), 3672–3680.
- (9) Kim, H.; Lee, C. Visible-Light-Induced Photocatalytic Reductive Transformations of Organohalides. *Angew. Chem. Int. Ed.* **2012**, *51* (49), 12303–12306.
- (10) Stoll, S.; Schweiger, A. EasySpin, a Comprehensive Software Package for Spectral Simulation and Analysis in EPR. *J. Magn. Reson.* **2006**, *178* (1), 42–55.
- (11) Bates, C. G.; Gujadhur, R. K.; Venkataraman, D. A General Method for the Formation of Aryl-Sulfur Bonds Using Copper(I) Catalysts. *Org. Lett.* **2002**, *4* (16), 2803–2806.

- (12) Bolton, J. R.; Stefan, M. I.; Shaw, P.-S.; Lykke, K. R. Determination of the Quantum Yields of the Potassium Ferrioxalate and Potassium Iodide–Iodate Actinometers and a Method for the Calibration of Radiometer Detectors. *J. Photochem. Photobiol. Chem.* **2011**, 222 (1), 166–169.
- (13) Bowman, W. D.; Demas, J. N. Ferrioxalate Actinometry. A Warning on Its Correct Use. *J. Phys. Chem.* **1976**, 80 (21), 2434–2435.
- (14) Neese, F. The ORCA Program System. *Wiley Interdiscip. Rev. Comput. Mol. Sci.* **2012**, 2 (1), 73–78.
- (15) Perdew, J. P. Density-Functional Approximation for the Correlation Energy of the Inhomogeneous Electron Gas. *Phys. Rev. B* **1986**, 33 (12), 8822–8824.
- (16) Becke, A. D. Density-Functional Exchange-Energy Approximation with Correct Asymptotic Behavior. *Phys. Rev. A* **1988**, 38 (6), 3098–3100.
- (17) Weigend, F.; Furche, F.; Ahlrichs, R. Gaussian Basis Sets of Quadruple Zeta Valence Quality for Atoms H–Kr. *J. Chem. Phys.* **2003**, 119 (24), 12753–12762.
- (18) Neese, F. Prediction and Interpretation of the ^{57}Fe Isomer Shift in Mössbauer Spectra by Density Functional Theory. *Inorganica Chim. Acta* **2002**, 337, 181–192.
- (19) Hirata, S.; Head-Gordon, M. Time-Dependent Density Functional Theory within the Tamm–Dancoff Approximation. *Chem. Phys. Lett.* **1999**, 314 (3–4), 291–299.

SUPPLEMENTARY DATA FOR CHAPTER 3

B.1 General Considerations

Chemicals. All manipulations were carried out using standard Schlenk or glovebox techniques under an N₂ atmosphere. Solvents were deoxygenated and dried by thoroughly sparging with N₂ followed by passage through an activated alumina column in a solvent purification system by SG Water, USA LLC. Solvents were tested with sodium benzophenone ketyl in tetrahydrofuran (THF) in order to confirm the absence of oxygen and water. Deuterated solvents were purchased from Cambridge Isotope Laboratories, Inc., degassed, and dried over activated 3 Å molecular sieves prior to use. Cp*₂Co,¹ NaBAr^F₄,² Ph₂NH₂OTf,³ 1-(4-bromobutyl)pyrene,⁴ 3-iodo-4-bromophenol,⁵ and diisopropylphosphine⁶ were prepared according to literature procedures. All other reagents were purchased from commercial vendors and used without further purification unless otherwise stated.

Infrared, EPR, and UV-Vis Spectroscopy. UV-vis experiments were conducted with sealable 1-cm path length fused quartz cuvettes (Starna Cells) using a Cary 50 UV-vis spectrometer. X-band EPR measurements were made with a Bruker EMX spectrometer at 77 K. IR measurements were recorded on a Bruker ALPHA Diamond ATR.

NMR Spectroscopy. All NMR spectra were obtained at ambient temperature using Varian 400 and 500 MHz spectrometers unless otherwise noted. ¹H and ¹³C NMR chemical shifts (δ) are reported in parts per million (ppm) relative to TMS. ³¹P NMR spectra are

reported relative to 85% aqueous H₃PO₄. Solution phase magnetic measurements were performed by the method of Evans.⁷

Mass Spectrometry. The ESI-MS data was collected using a Thermo LTQ ion trap mass spectrometer.

X-ray Photoelectron Spectroscopy. The surface composition of the carbon electrode surface before and after controlled potential electrolysis measurements was determined via XPS on a Kratos Axis Ultra spectrometer with DLD (Kratos Analytical; Manchester, UK). The excitation source for all analysis was monochromatic Al K $\alpha_{1,2}$ ($h\nu = 1486.6$ eV) operating at 10 mA and 15 kV. The X-ray source was directed at 54° with respect to the sample normal. A base pressure of 1×10^{-9} Torr is maintained in the analytical chamber, which rises to 5×10^{-9} Torr during spectral acquisition. All spectra were acquired using the hybrid lens magnification mode and slot aperture, resulting in an analyzed area of $700 \mu\text{m} \times 400 \mu\text{m}$. Survey scans were collected using 160 eV pass energy, while narrow region scans used 10 eV; charge compensation via the attached e⁻-flood source was not necessary in this study.

Gas Chromatography. H₂ was quantified on an Agilent 7890A gas chromatograph (HP-PLOT U, 30 m, 0.32 mm ID; 30 °C isothermal; nitrogen carrier gas) equipped with a thermal conductivity detector. A 10 mL injection was used for all measurements and integration area was converted to percent H₂ using a calibration obtained from injection of mixtures of known amounts of H₂ and N₂.

Combustion Analysis. Combustion analysis measurements were collected using a PerkinElmer 2400 Series II CHN Elemental Analyzer by facility staff.

Ammonia Quantification. Reaction mixtures were transferred to a Schlenk tube and frozen at 77 K. The frozen reaction mixture was treated with a solution of [Na][O-*t*-Bu] (40 mg, 0.4 mmol) in THF (2 mL) over 1 minute, ensuring no thawing of the reaction mixture, and sealed. The resulting suspension was allowed to stir for 10 minutes before all volatiles were vacuum transferred into a Schlenk charged with HCl (3 mL of a 2.0 M solution in Et₂O, 6 mmol). After completion of the vacuum transfer, the collection flask was sealed and warmed to room temperature. Solvent was removed in vacuo and [NH₄][Cl] was quantified by the Indophenol method.⁸

B.2 Synthesis and Characterization

Synthesis of 3-Iodo-4-Bromo-*O*-(1-pyrenyl-butyl)phenol

In a 250 mL flask, 1.6 g 4-bromobutyl-(1-pyrene) (4.7 mmol), 1.6 g 3-bromo-4-iodophenol (5.4 mmol, 1.2 equiv), and 1.6 g K₂CO₃ (11.6 mmol, 2.5 equiv) were added to 80 mL DMF. The reaction was heated to 80 °C and stirred for 16 h. After cooling, the reaction was diluted into 200 mL DCM and washed with water (2 x 200 mL). The organic layer was dried on a rotovap, and the resulting yellow solid was recrystallized from DCM/pentane to give white crystals (2.5 g, 95%). ¹H NMR (400 MHz, CDCl₃) δ 8.27 (d, *J* = 9.3 Hz, 1H), 8.18 (d, *J* = 2.7 Hz, 1H), 8.16 (d, *J* = 3.0 Hz, 1H), 8.12 (d, *J* = 3.6 Hz, 1H), 8.10 (d, *J* = 5.1 Hz, 1H), 8.03 (s, 1H), 8.03 (s, 1H), 8.00 (t, *J* = 7.6 Hz, 1H), 7.88 (d, *J* = 7.8 Hz, 1H), 7.42 (d, *J* = 8.8 Hz, 1H), 7.37 (d, *J* = 2.9 Hz, 1H), 6.72 (dd, *J* = 8.9, 2.9 Hz, 1H), 3.94 (t, *J* = 6.2 Hz, 2H), 3.41 (t, *J* = 7.5 Hz, 2H), 2.27-1.82 (M, 4H). ¹³C NMR (101 MHz, CDCl₃) δ 158.15, 136.29, 132.59,

131.43, 130.88, 129.89, 128.62, 127.51, 127.32, 127.26, 126.67, 125.99, 125.86, 125.11, 125.02, 124.94, 124.81, 124.75, 123.30, 120.09, 116.40, 101.05, 68.21, 33.11, 29.02, 28.07.

Synthesis of 3-diisopropylphosphino-4-Bromo-*O*-(1-pyrenyl-butyl)phenol

1.67 g 3-Iodo-4-Bromo-*O*-(1-pyrenyl-butyl)phenol (3.0 mmol), 0.50 g K₂CO₃ (3.62 mmol, 1.2 equiv), 36 mg Pd(OAc)₂ (0.16 mmol, 5.3 mol %), and 80 mg 1,1'-bis(diisopropylphosphino)ferrocene (0.14 mmol, 4.8 mol %) were weighed into a 100 mL sealable Schlenk tube. 5 mL dioxane and 1 mL THF were then added, and the suspension was stirred at 25 °C (Note: solvents must be extremely dry to prevent ether cleavage). After 1 h, 590 μL HPiPr₂ (470 mg, 4.0 mmol) was added and the tube was sealed. The reaction was stirred 22 h at 85 °C. The reaction was cooled, 2 mL THF was added, and the resulting suspension was filtered over Celite. The filtrate was dried in vacuo, and the resulting residue was purified by silica gel column chromatography (2:1 hexane/DCM performed in air with solvents used as received, R_f = 0.38) to give a white solid (1.28 g, 77%). ¹H NMR (300 MHz, C₆D₆) δ 8.15 (dd, *J* = 9.3, 0.8 Hz, 1H), 8.03 – 7.89 (m, 4H), 7.84 (d, *J* = 3.7 Hz, 1H), 7.79 (td, *J* = 7.6, 1.1 Hz, 1H), 7.67 (d, *J* = 7.8 Hz, 1H), 7.43 (ddd, *J* = 8.7, 3.3, 0.9 Hz, 1H), 7.08 (dd, *J* = 3.0, 1.2 Hz, 1H), 6.40 (ddd, *J* = 8.8, 3.0, 0.9 Hz, 1H), 3.52 (t, *J* = 6.3 Hz, 2H), 3.13 (t, *J* = 7.5 Hz, 2H), 1.97 – 1.61 (m, 6H), 1.07 (dd, *J* = 14.2, 7.0 Hz, 5H), 0.92 (dd, *J* = 12.0, 6.9 Hz, 4H). ³¹P NMR (121 MHz, C₆D₆) δ 9.83.

Synthesis of Tris(2-diisopropylphosphino-4-(1-pyrenyl-butoxy)phenyl)borane (^{py}P₃^B, 3.1)

550 mg 3-diisopropylphosphino-4-Bromo-*O*-(1-pyrenyl-butyl)phenol (1.0 mmol) was dissolved in a mixture of 75 mL toluene and 15 mL Et₂O. The resulting solution was cooled to -78 °C and 0.66 mL nBuLi (1.6 M in hexanes, 1.05 mmol, 1.05 equiv) was added. After stirring 20 min, the reaction was warmed to 25 °C and stirred for a further 30 min. The resulting yellow solution was cooled back to -78 °C and 45 μL BF₃·OEt₂ (0.36 mmol, 0.36 equiv) was added. The reaction was then stirred 8 h at -78 °C and allowed to warm to 25 °C. After 16 h, 20 mL pentane was added and the resulting suspension was stirred 1 h and filtered over Celite. The reaction was then concentrated to 5 mL and layered with 20 mL pentane and allowed to crystallize at -40 °C. The resulting product was recrystallized two more times, giving **1** as a white solid (285 mg, 61%). ¹H NMR (400 MHz, C₆D₆) δ 8.11 (d, *J* = 8.6 Hz, 1H), 7.99 – 7.84 (m, 5H), 7.79 (q, *J* = 6.6 Hz, 2H), 7.74 (d, *J* = 9.2 Hz, 1H), 7.62 (d, *J* = 7.4 Hz, 1H), 7.29 (s, 1H), 6.80 (d, *J* = 7.9 Hz, 1H), 3.71 (t, *J* = 6.1 Hz, 2H), 3.10 (t, *J* = 7.6 Hz, 2H), 2.08 – 1.95 (m, 2H), 1.79 (p, 2H), 1.68 (p, *J* = 169.2 Hz, 2H), 1.19 – 0.81 (m, 12H). ³¹P NMR (162 MHz, C₆D₆) δ 2.7. Anal. calcd for C₉₆H₁₀₂O₃P₃B: C 81.92, H 7.30, N 0.0; found: C 81.19, H 7.48 N 0.0.

Synthesis of ^{py}P₃^BFeBr (**3.2**)

In a vial, 70 mg ^{py}P₃^B (**3.1**) (0.050 mmol) and 11 mg FeBr₂ (0.050 mmol, 1 equiv) were suspended in 4 mL THF. The suspension was vigorously stirred for 2 h, giving a bright yellow solution. Excess 1% Na/Hg (3 mg Na, 0.13 mmol, 2.6 equiv) was added and the solution was stirred a further 2 h. The green-brown solution was decanted and dried in vacuo and extracted with benzene (2 x 2 mL) and lyophilized to give the product as a brown powder (55 mg, 71%). ES-MS (positive mode, *m/z*) calcd for ^{py}P₃^BFeBr: 1543.6, found 1543.8. ¹H

NMR (400 MHz, C₆D₆) δ 91.11, 33.68, 19.09, 7.99, 7.85, 7.79, 7.73, 7.50, 3.62, 3.28, 3.00, 2.64, 1.68, 1.32, 1.03, 0.90, 0.26, -1.54, -23.14. Evans, μ_{eff} (C₆D₆, Evans method, 20 °C): 3.7 μ_{B} . Anal. calcd for C₉₆H₁₀₂O₃P₃BFeBr: C 74.71, H 6.66, N 0.0; found: C 75.64, H 6.90, N 0.2.

Synthesis of ^{py}P₃^BFeMe (3.3)

15.4 mg ^{py}P₃^BFeBr (3.2) (0.010 mmol) was dissolved in a mixture of 1.5 mL THF and 1.5 mL Et₂O and cooled to -78 °C. 13 μ L methyllithium solution (1.6 M in Et₂O, 0.021 mmol, 2.1 equiv) was added, and the reaction was stirred 1 h at -78 °C then allowed to warm to room temperature. The solution was stirred 2 h at 25 °C, and the solvent was removed in vacuo. The residue was washed with pentane (2 x 3 mL) and extracted with 2 mL benzene and lyophilized to give the product as a red powder (14.2 mg, 96%). ES-MS (positive mode, *m/z*) calcd for ^{py}P₃^BFeMe: 1478.7, found 1478.5. ¹H NMR (400 MHz, C₆D₆) δ 72.08, 33.15, 12.30, 9.95, 8.11, 7.89, 7.79, 7.62, 6.81, 5.10, 3.83, 3.71, 3.38, 3.11, 2.96, 2.58, 1.79, 1.67, 1.47, 1.31, 1.03, 0.27, -2.35, -2.86, -7.43, -16.22. μ_{eff} (C₆D₆, Evans method, 20 °C): 3.8 μ_{B} . Anal. calcd for C₉₇H₁₀₅O₃P₃BFe: C 78.80, H 7.16, N 0.0; found: C 78.42, H 7.24 N 0.3. UV-vis (THF, nm {cm⁻¹M⁻¹}): 375 {4800}.

Synthesis of [^{py}P₃^BFeN₂][Na(THF)_n] (3.4)

6.0 mg ^{py}P₃^BFeBr (3.2) (3.9 μ mol) was dissolved in 1 mL THF and cooled to -78 °C. 7.8 μ L Na/naphthalene (1M in THF, 2.0 equiv) was added and the reaction was allowed to warm. 1 mL pentane was added and the reaction was filtered and solvent was removed in vacuo to give 3.4 as a red solid (4.8 mg, 60% assuming n = 6). ES-MS (negative mode, *m/z*) calcd for

$[\text{P}^{\text{y}}\text{P}_3^{\text{B}}\text{Fe}]^-$, $[\text{P}^{\text{y}}\text{P}_3^{\text{B}}\text{Fe}(\text{THF})]^-$: 1462.6, 1535.7; found 1462.6, 1535.2. The N_2 adduct was not observed under electrospray conditions. ^1H NMR (400 MHz, THF-d_8) δ 18.65, 13.26, 12.87, 12.74, 12.54, 12.45, 12.34, 12.18, 10.49, 9.05, 8.77, 7.21, 6.92, 6.73, 6.32, 5.55, 5.41, 3.91. μ_{eff} (THF-d_8 , Evans method, 20 °C): 1.7 μ_{B} . IR (thin film) $\nu_{\text{NN}} = 1930, 1880 \text{ cm}^{-1}$.

B.3 Chemical Ammonia Generation Experiments

Ammonia generation experiments were conducted based on a previously reported protocol. In a nitrogen-filled glovebox, the precatalyst (2.0 μmol) was weighed into a vial. The precatalyst was then transferred quantitatively into a 250 mL Schlenk tube with a Teflon valve using THF. The THF was then evaporated to provide a thin film of precatalyst at the bottom of tube. The tube is then charged with a stir bar, the acid (108 equiv), and Cp^*Co (54 equiv) as solids. The tube is then chilled to 77 K and allowed to equilibrate for 10 minutes. To the chilled tube is added 1 mL of Et_2O . The temperature of the system is allowed to equilibrate for 5 minutes. This tube is sealed and is passed out of the box and transported to a fume hood. The tube is then transferred to a dry ice/acetone bath and is allowed to stir at $-78 \text{ }^\circ\text{C}$ for 3 h. The tube is then allowed to warm to RT with stirring and then stirred at RT for a further ten minutes. At this point the previously described procedure for quantifying ammonia was employed. To ensure reproducibility, all experiments were conducted in 250 mL tubes using 25 mm stir bars and stirring was conducted at $\sim 650 \text{ rpm}$.

B.4 Electrochemistry

All electrochemical measurements were conducted in a nitrogen-filled glovebox with a CH Instruments 600B electrochemical analyzer. For all measurements at low temperature,

the temperature was controlled by immersing the glovebox cold well in a well-stirred isopropanol bath cooled by an SP Scientific FTS Systems FC100 immersion cooler. For all measurements, a Ag/AgPF₆ reference electrode filled with 0.1 M NaBar^F₄ and isolated from the cell by a Coralpor frit was used. All potentials are reported relative to externally-referenced Fc⁺⁰.

HOPG Electrode Preparation. Highly-ordered pyrolytic graphite (HOPG) was obtained from graphitestore.com and cut into rectangular plates of 15 mm x 10 mm x 1 mm. These plates were then sonicated in deionized water for 30 minutes followed by acetonitrile for a further 30 minutes. The plates were dried in a dessicator overnight, followed by oven drying for 2 h. The plates were then brought into the glovebox and soaked in a 1 mM THF solution of analyte for 16 h, followed by washing with THF to remove any loosely-bound species. The electrodes were then dried in vacuo for 30 minutes to remove any remaining THF.

Cyclic voltammetry of solution-phase species. CV experiments were conducted in a 20 mL cell using a 3 mm glassy carbon disc as the working electrode and a 5 mm glassy carbon rod as the auxiliary electrode.

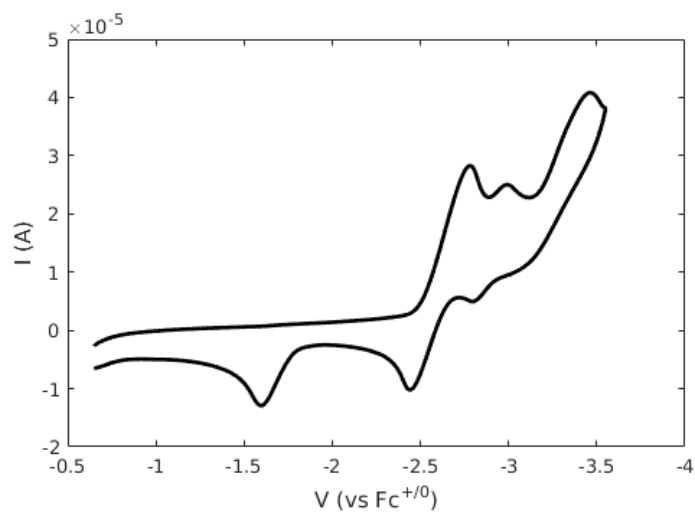


Figure B.1: Cyclic voltammogram of pyP_3^{B} (**3.1**) in 0.1 M $\text{NaBAr}_4^{\text{F}_4}/\text{Et}_2\text{O}$ solution. Scan rate = 100 mv/s.

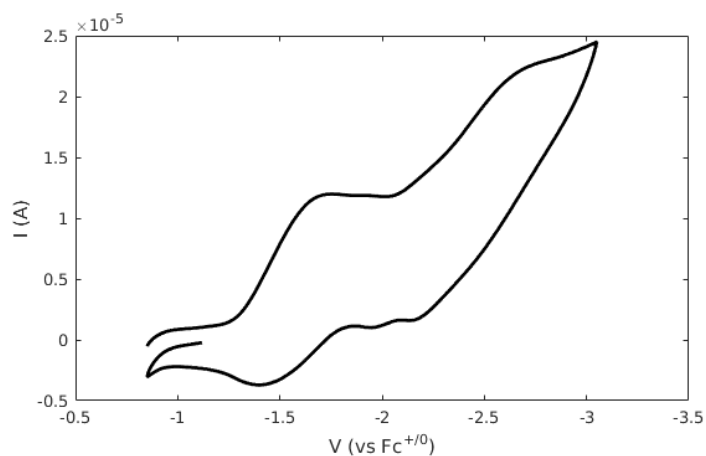


Figure B.2: Cyclic voltammogram of $\text{pyP}_3^{\text{B}}\text{FeMe}$ (**3.3**) in 0.1 M $\text{NaBAr}_4^{\text{F}_4}/\text{Et}_2\text{O}$ solution. Scan rate = 100 mv/s.

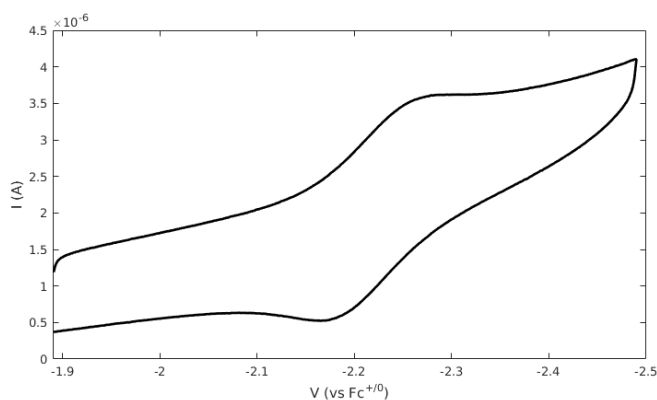


Figure B.3: Cyclic voltammogram of $[\text{P}^{\text{py}}\text{P}_3^{\text{B}}\text{FeN}_2][\text{Na}(\text{THF})_n]$ (**3.4**) in 0.1 M $\text{NaBAr}^{\text{F}}_4/\text{Et}_2\text{O}$ solution. Scan rate = 100 mv/s.

CV of prepared electrodes. In a 20 mL cell, a 0.1 M solution of $\text{NaBAr}^{\text{F}}_4$ in Et_2O was prepared and cooled to $-35\text{ }^\circ\text{C}$. An HOPG working electrode presoaked in analyte, a clean HOPG auxiliary electrode, and a reference electrode were then placed into the pre-cooled solution. The cell was allowed to thermally equilibrate for 5 minutes before measurement. A freshly prepared electrode was used for every scan so electrochemical decomposition did not affect any subsequent measurements.

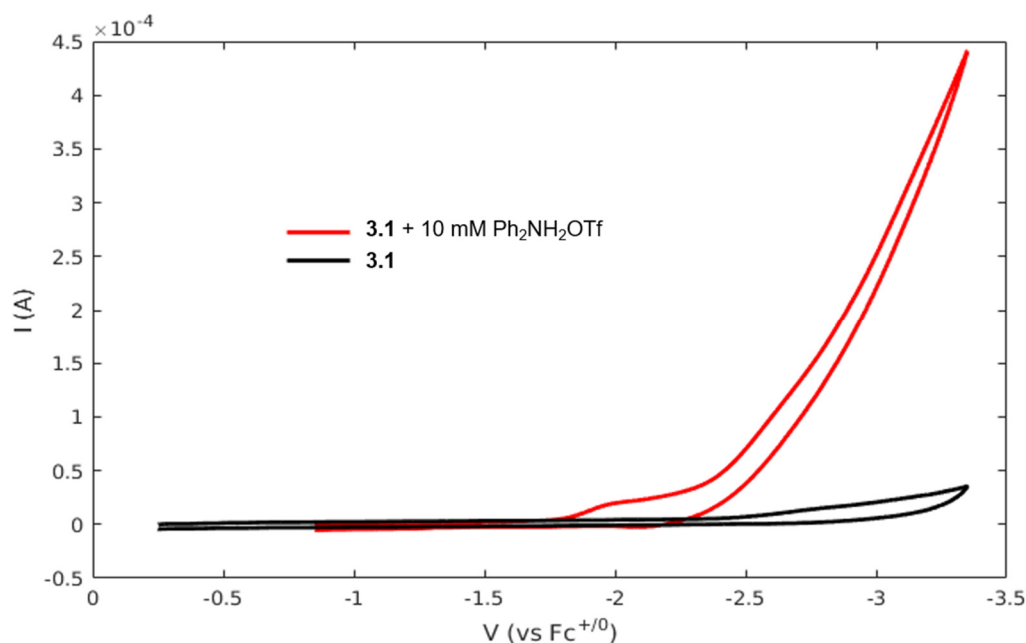


Figure B.4: Cyclic voltammograms of surface-attached pyP_3^{B} (**3.1**) in the presence (red trace) and absence (black trace) of 10 mM $[\text{Ph}_2\text{NH}_2][\text{OTf}]$ on an HOPG electrode in 0.1 M $\text{NaBAR}_4^{\text{F}}/\text{Et}_2\text{O}$ solution. Scan rate = 50 mv/s, temperature = -35 °C.

B.5 Electrochemical Ammonia Generation Experiments.

For CPE experiments, a sealable single-compartment cell was filled with 6 mL of 0.1 M $\text{NaBAR}_4^{\text{F}}$ in Et_2O electrolyte, and 100 μmol of acid was added. The chamber is fitted with a Na metal auxiliary electrode inside a 7 mm diameter glass tube separated from the working electrode by a medium porosity sintered glass frit, an HOPG working electrode submerged to a solution depth of 10 mm, and a Ag/AgPF_6 in 0.1 M $\text{NaBAR}_4^{\text{F}}/\text{Et}_2\text{O}$ reference electrode isolated by a CoralPor frit and referenced externally to $\text{Fc}^{+/0}$. The temperature is maintained at -35 °C by a SP Scientific FTS Systems FC100 immersion cooler. All experiments were stirred with a stirring rate of ~ 300 rpm. The cell is held at a working potential of -2.4 V vs

$\text{Fc}^{+/0}$ for 6 h, after which an additional 100 μmol of acid in 2 mL 0.1 M $\text{NaBAR}^{\text{F}}_4/\text{Et}_2\text{O}$ is injected through a rubber septum to sequester NH_3 as $[\text{NH}_4][\text{OTf}]$. The cell was then stirred a further 10 minutes, and the contents were transferred to a Schlenk tube and washed with additional Et_2O . The resulting solution was analyzed for NH_3 as described above.

B.6 Electrode Desorption Experiment

An electrode containing adsorbed $^{\text{py}}\text{P}_3^{\text{B}}\text{FeMe}$ (**3.3**) was prepared as above. The electrode was then soaked in 2 mL THF for 1 h. The THF was then transferred to another vial, and the soaking procedure was repeated a further two times. The THF extracts were combined and the solvent was removed in vacuo. The resulting residue was then dissolved in 300 μL THF, and this solution was analyzed by UV-visible spectroscopy in a 1 cm path length low-volume cuvette.

B.7 Supplementary XPS data

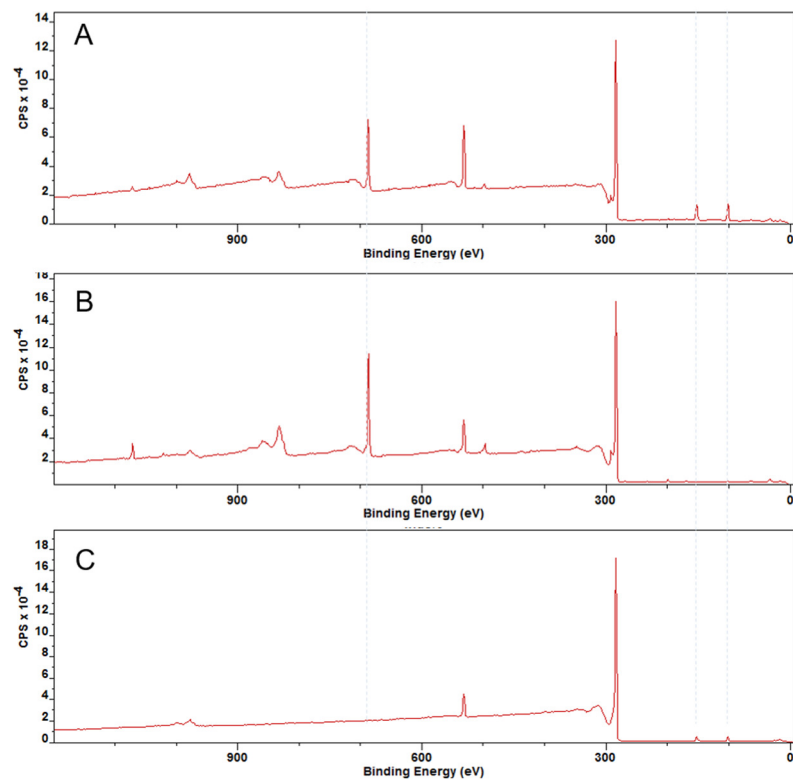


Figure B.5: Overview XPS spectra of (A) functionalized electrode pre-electrolysis, (B) functionalized electrode post-electrolysis, and (C) unfunctionalized electrode.

B.8 NMR Spectra

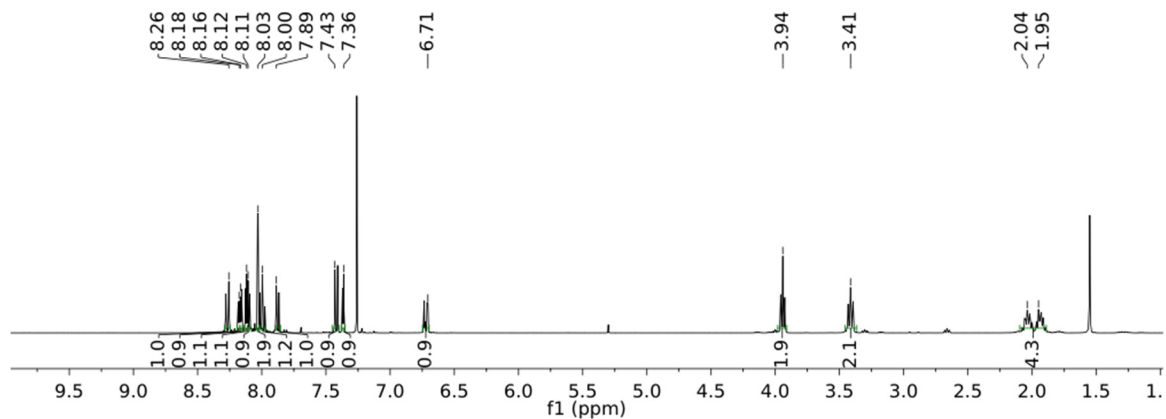


Figure B.6: ^1H NMR of 3-Iodo-4-Bromo-*O*-(1-pyrenyl-butyl)phenol in CDCl_3 .

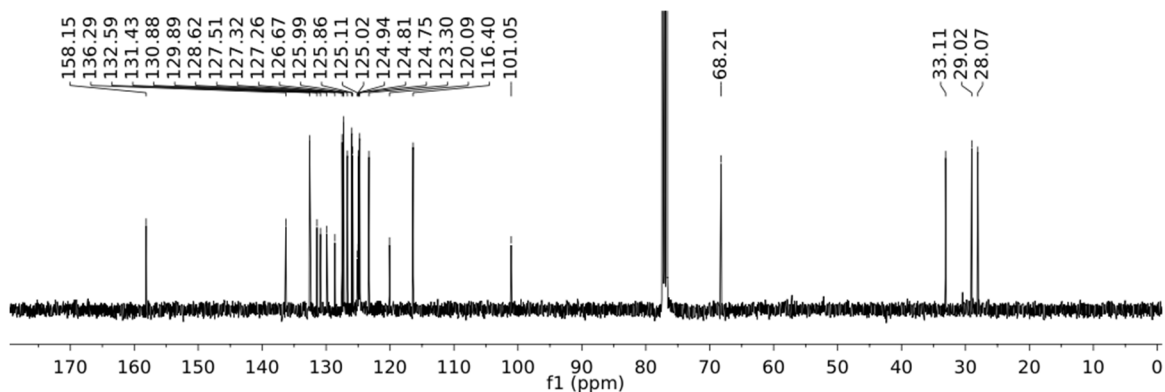


Figure B.7: $^{13}\text{C}\{^1\text{H}\}$ NMR of 3-Iodo-4-Bromo-*O*-(1-pyrenyl-butyl)phenol in CDCl_3 .

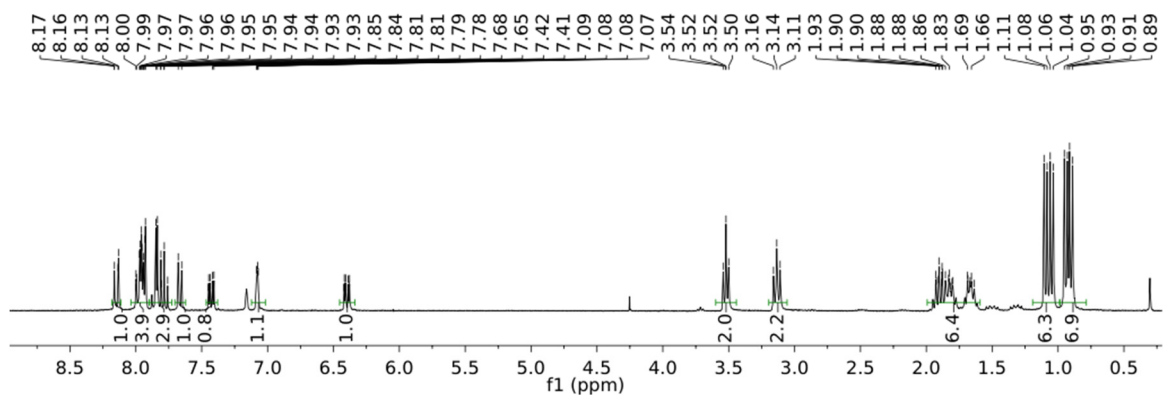


Figure B.8: ^1H NMR of 3-diisopropylphosphino-4-Bromo-*O*-(1-pyrenyl-butyl)phenol in C_6D_6 .

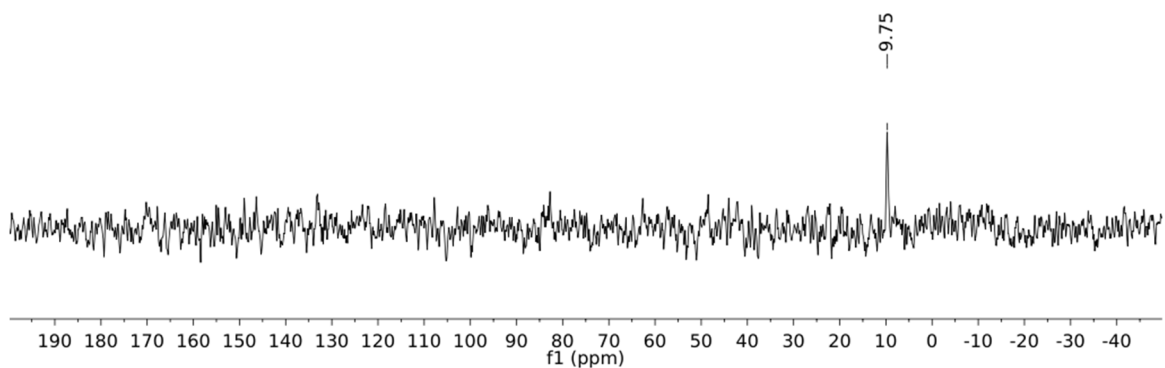


Figure B.9: $^{31}\text{P}\{^1\text{H}\}$ NMR of 3-diisopropylphosphino-4-Bromo-*O*-(1-pyrenyl-butyl)phenol in C_6D_6 .

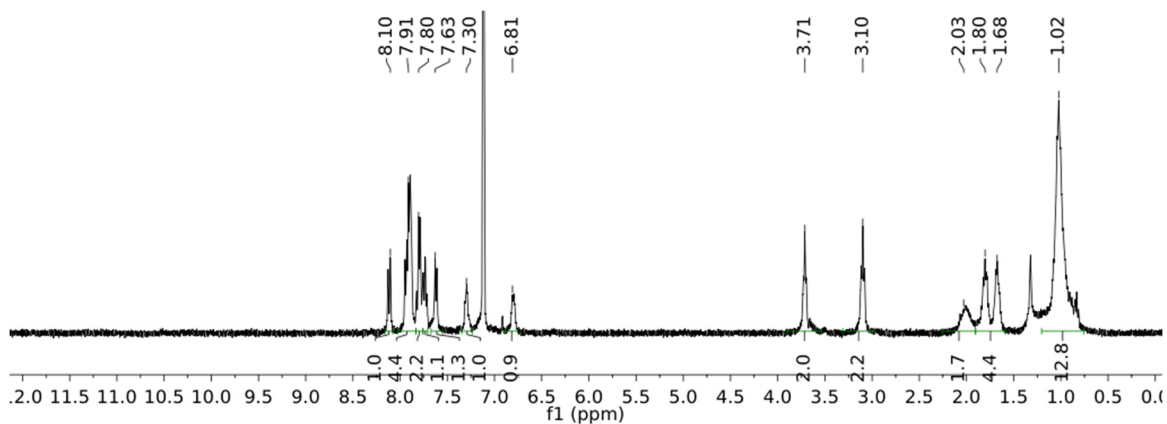


Figure B.10: ^1H NMR of pyP_3^{B} (**3.1**) in C_6D_6 .

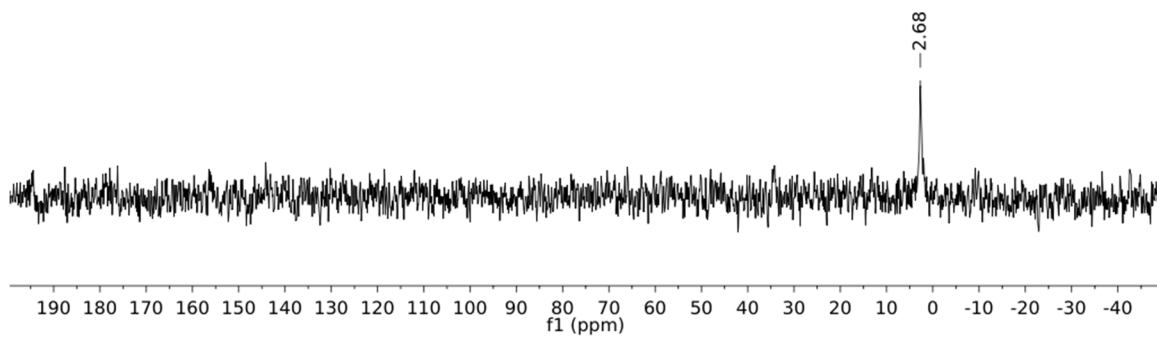


Figure B.11: $^{31}\text{P}\{^1\text{H}\}$ NMR of pyP_3^{B} (**3.1**) in C_6D_6 .

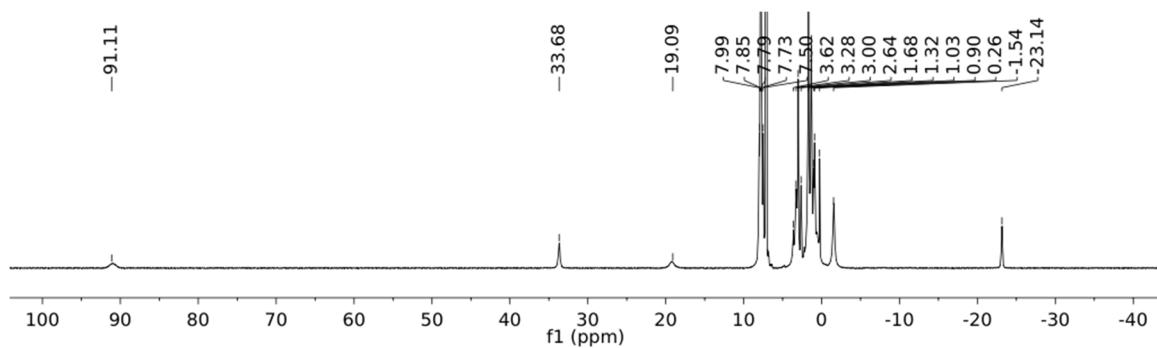


Figure B.12: ^1H NMR of $\text{pyP}_3^{\text{B}}\text{FeBr}$ (**3.2**) in C_6D_6 .

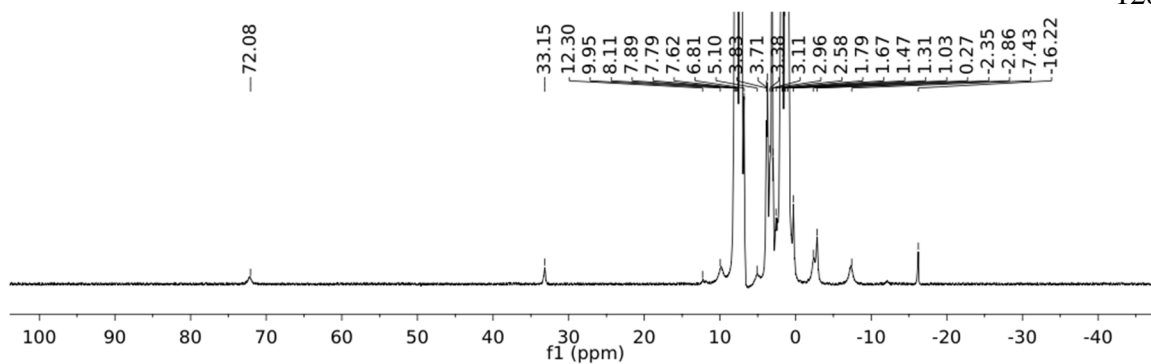


Figure B.13: ^1H NMR of $\text{pyP}_3^{\text{B}}\text{FeMe}$ (**3.3**) in C_6D_6 .

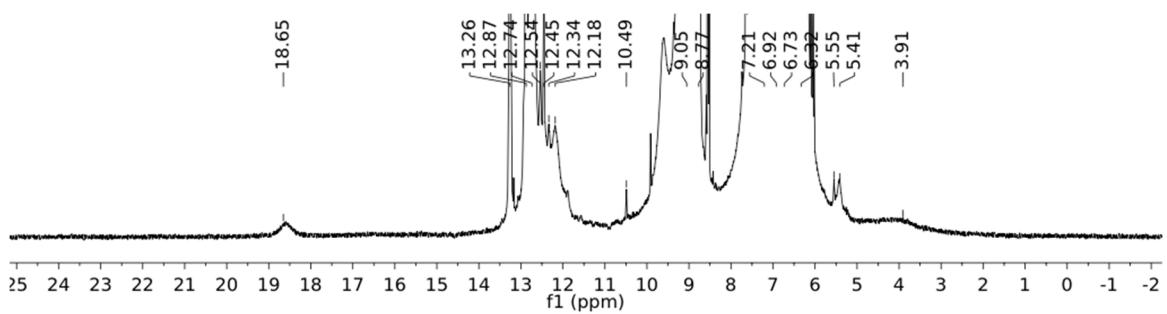


Figure B.14: ^1H NMR of $[\text{pyP}_3^{\text{B}}\text{FeN}_2][\text{Na}(\text{THF})_n]$ (**3.4**) in THF-d_8 .

B.9 References

- (1) Robbins, J. L.; Edelstein, N.; Spencer, B.; Smart, J. C. Syntheses and Electronic Structures of Decamethylmetallocenes. *J. Am. Chem. Soc.* **1982**, *104* (7), 1882–1893.
- (2) Del Castillo, T. J.; Thompson, N. B.; Peters, J. C. A Synthetic Single-Site Fe Nitrogenase: High Turnover, Freeze-Quench ^{57}Fe Mössbauer Data, and a Hydride Resting State. *J. Am. Chem. Soc.* **2016**, *138* (16), 5341–5350.
- (3) Vicente, J.; Chicote, M.-T.; Guerrero, R.; Jones, P. G. Synthesis of Complexes $[\text{Au}(\text{PPh}_3)\text{L}]^+$ (L = Primary, Secondary or Tertiary Amine). Crystal Structure of $[\text{Au}(\text{PPh}_3)(\text{NMe}_3)][\text{ClO}_4] \cdot \text{CH}_2\text{Cl}_2$. *J. Chem. Soc. Dalton Trans.* **1995**, *0* (8), 1251–1254.
- (4) Taher, A.; Lee, K. C.; Han, H. J.; Kim, D. W. Pyrene-Tagged Ionic Liquids: Separable Organic Catalysts for $\text{S}_{\text{N}}2$ Fluorination. *Org. Lett.* **2017**, *19* (13), 3342–3345.
- (5) Yavari, K.; Retailleau, P.; Voituriez, A.; Marinetti, A. Heterohelicenes with Embedded P-Chiral 1H-Phosphindole or Dibenzophosphole Units: Diastereoselective Photochemical Synthesis and Structural Characterization. *Chem. – Eur. J.* **2013**, *19* (30), 9939–9947.
- (6) Zhu, K.; Achord, P. D.; Zhang, X.; Krogh-Jespersen, K.; Goldman, A. S. Highly Effective Pincer-Ligated Iridium Catalysts for Alkane Dehydrogenation. DFT Calculations of Relevant Thermodynamic, Kinetic, and Spectroscopic Properties. *J. Am. Chem. Soc.* **2004**, *126* (40), 13044–13053.

- (7) Sur, S. K. Measurement of Magnetic Susceptibility and Magnetic Moment of Paramagnetic Molecules in Solution by High-Field Fourier Transform NMR Spectroscopy. *J. Magn. Reson.* (1969) **1989**, 82 (1), 169–173.
- (8) Weatherburn, M. W. Phenol-Hypochlorite Reaction for Determination of Ammonia. *Anal. Chem.* **1967**, 39 (8), 971–974.